JAIST Repository
https://dspace.jaist.ac.jp/

Title	新規デバイス応用のための2次元半導体・金属界面の理論的モデリング
Author(s)	ABDUL, GHAFFAR
Citation	
Issue Date	2024-03
Type	Thesis or Dissertation
Text version	ETD
URL	http://hdl.handle.net/10119/19062
Rights	
Description	Supervisor: 本郷 研太, 先端科学技術研究科, 博士

JAPAN
ADVANCED INSTITUTE OF
SCIENCE AND TECHNOLOGY

Japan Advanced Institute of Science and Technology

Doctoral Dissertation

Theoretical modeling of 2D-semiconductor/metal interfaces for novel prototype device application

Abdul Ghaffar

Supervisor: Kenta Hongo

Graduate School of Advanced Science and Technology
Japan Advanced Institute of Science and Technology
Information Science
March, 2024

Abstract

High-performance electronic and optoelectronic devices rely heavily on efficient charge transport at material interfaces. This study investigates critical factors influencing contact resistance in 2D-semiconductor/metal contacts through computational modeling. We focus on two promising 2D semiconductors: phosphorene and transition metal dichalcogenide (WS_2). A comprehensive analysis of 18 different metal electrodes (Ag, Al, Au, Co, Cr, Cu, Mo, Nb, Ni, Pd, Pt, Ru, Sc, Ta, Ti, W, V, and Zn) for phosphorene reveals the interplay between mechanical and electrical properties at the interface. This broad exploration allows for identifying optimal electrode materials that minimize contact resistance. For WS_2, we strategically downselected six metals (Ag, Au, Cu, Pd, Pt, and Sc) with varying electronegativity and work function. This targeted approach ensures a thorough understanding of the mechanical and electrical behavior of WS_2/metal interfaces while maintaining applicability to diverse contact scenarios. Building upon established knowledge, we further explored the potential of substitutional dopants (C, Cl, P, N, O, and F) in WS_2 to enhance contact properties. Our investigation evaluates several interface properties for their effectiveness in reducing contact resistance and ultimately achieving superior performance in 2D semiconductor devices. Notably, our study reveals that metal selection can be a feasible approach for phosphorene-based contacts, while for WS_2, C, P, and N-doping can lead to reduction in Fermi level pinning (FLP), a highly desirable outcome, without compromising the mechanical stability of the interface. At the same time, Cl and F-dopants can provide a path to lower the n-type Schottky barrier height (SBH). Our method provides an alternative approach to reduce the FLP that doesn't increase the tunneling barriers, which is not observed with other interface engineering methods. This work can guide further experimental work in designing and accelerating the discovery of optimal and low-energy consuming 2D-semiconductor/metal interfaces.

Keywords: *Schottky barrier*, *ab initio*, *Phosphorene*, *WS_2*, *semiconductor-metal interface*, *Tunnel barrier*, *metal-induced gap states*, *Fermi level pinning*, *Contact resistance*, *Interface dipole formation*

Acknowledgements

The completion of this research project owes its success to the unwavering guidance and support of numerous individuals. Foremost, I extend my heartfelt gratitude to my research supervisor, Prof. Kenta Hongo, whose constant support and guidance were instrumental throughout my research journey. His invaluable assistance extended to thesis documentation, manuscript preparation, and presentation readiness. I would also like to express my appreciation to Assoc. Prof. Nihar R. Mohapatra from IIT Gandhinagar (India), whose collaboration greatly enriched this research endeavor. I extend my acknowledgment to my second supervisor, Assoc. Prof. Ryo Maezono, as well as to Assoc. Prof. Shogo Okada, my minor research supervisor, and Dr. Ichiba Tomohiro, for their invaluable guidance. My sincere thanks go to the members of the thesis committee, including Prof. Oshima, Prof. Okada, Assoc. Prof. Hongo, and Prof. Maezono, for dedicating their time to review my dissertation and presentations, and providing invaluable feedback. The computational aspects of this research were made possible by the use of supercomputers at JAIST. I extend my gratitude to RCACI at JAIST for granting access and providing assistance during challenging times. I am deeply grateful to our lab staff, Kitagawa-san, Fujita-san, and Myojin-san, whose support was indispensable in meeting project deadlines. To my lab mates, including Dr. Song, Dr. Genki, Dr. Abhishek, Mr. Okumura, and Mr. Rohit, I offer my heartfelt thanks for their constant support, assistance, and encouragement. Last but certainly not least, I owe a debt of gratitude to my parents and family members, whose unwavering support and encouragement were a source of strength during challenging times.

Thank you all for your invaluable contributions and support.

Contents

Abstract **i**
List of Figures . . . viii
List of Tables . . . ix

1 Introduction **1**
1.1 Background . . . 1
1.2 Motivation . . . 2
1.3 Problem Statements . . . 5
1.4 Outline . . . 5

2 Methodology **7**
2.1 Theoretical uderpinning of *ab initio* methods . . . 7
2.2 Many-Body Schrödinger Equation . . . 7
2.3 Mean-field Theory . . . 8
2.3.1 Challenges and Solution of Mean-field Theories . . . 9
2.4 Density Functional Theory . . . 9
2.4.1 Kohn-Sham Equation and Exchange-correlation Functionals . . . 10
2.5 Self-Consistent Calculations . . . 12
2.5.1 Basis-set expansion . . . 12
2.5.2 Brillouin-Zone Integration . . . 14
2.5.3 Smearing . . . 14
2.5.4 Pseudopotential . . . 15
2.5.5 van der Waals correction . . . 15
2.6 Crystal Interface Construction . . . 17
2.6.1 The Number of Metal Layers . . . 17
2.6.2 Metallic Surface Orientation . . . 17
2.6.3 Lattice Strain . . . 18
2.6.4 Interface Distance and Vacuum Buffer . . . 18
2.7 Mechanical Property . . . 20
2.7.1 Interface Stability . . . 20
2.7.2 Interface Separation and Tunnel Barrier . . . 20
2.8 Electrical Properties . . . 23
2.8.1 Schottky Barrier Height . . . 25
2.8.2 Fermi Level Pinning . . . 26
2.8.3 Metal-induced Gap States (MIGS) . . . 28

3 Phosphorene-Metal Contact **29**
3.1 Background . . . 29
3.2 Computational Methodology . . . 30
3.3 Results and Discussion . . . 30
3.3.1 Mechanical Properties of the Interface . . . 32
3.4 Electrical Properties . . . 34
3.4.1 Partial Density of States (PDOS) . . . 34
3.4.2 Schottky Barrier Analysis . . . 36
3.4.3 Tunneling Barrier Analysis . . . 38
3.4.4 Mid-Interface Charge Density (MICD) . . . 40

4 WS_2-Metal Contact **45**
4.1 Background . . . 45
4.2 Results and Discussions . . . 46
4.2.1 Binding Strength and Mechanical Stability . . . 47
4.2.2 Schottky Barrier Analysis . . . 48
4.2.3 Tunnel Barrier and Tunneling Probability . . . 51
4.2.4 Metal Induced Gap States (MIGS) . . . 56
4.2.5 Interface Charge Analysis . . . 58

5 Summary **62**
5.1 Conclusion . . . 62

List of Figures

2.1 Jacob's ladder representing the hierarchy of approximations used in electronic structure calculation. The computational cost and accuracy largely depend on the specific condition and requirement. 11
2.2 SCF cycle used to iteratively solve the Kohn-Sham equation in a DFT calculation. 13
2.3 The illustration of the construction of semiconductor/metal interface. The percentage mean absolute lattice strain is given for different sets of interface matching. In the present case, the red circle indicates the interface constructed consisting of 123 atoms in total, with mean absolute strain = 0.09%. Interface construction is done using the QuantumATK [66] GUI. 19
2.4 (a) A schematic diagram of a typical FET. Contact resistance depends on two interfaces: 1) Vertical interface (direct semiconductor/metal contact), 2) Lateral interface (coupling between contact part and semiconductor in the channel). In figure (b) both the interfaces have been depicted as the atomic contacts. 21
2.5 Illustration of tunneling barrier emerging as a consequence of finite interface separation at the interface. 22
2.6 Energy levels and band bending upon metal-semiconductor contact. Vacuum-level has been assumed to be at zero reference point. 24
2.7 Illustration of FLP for WS_2-metal contact. It represents the FLP occurring towards CBM. High work function metals expected to yield p-type SBH such as Pd and Pt, contrarily lead to pinning towards CBM. This clearly shows that p-type conductivity is difficult to achieve with WS_2. 27

3.1 (a) Crystal structure of monolayer phosphorene as viewed from three different directions: top view showing the unit cell with lattice parameters a = 3.30 Å and b = 4.63 Å, side view depicts the armchair and zigzag dirctions. (b) Side view of the metal-phosphorene system with the specified coordinates. A vacuum buffer is introduced along the $\pm z$ direction. The combined metal-semiconductor systems contain 5 layers of metal interfaced to monolayer phosphorene. (Reproduced from Ghaffar *et al.* [92] under CC BY-NC-ND license.) . 31
3.2 Optimized structures for all the eighteen metal-semiconductor contacts. These structures represent the distinct effect of metals on the phosphorene surface. The apparent distortion in some of the cases is linked with the higher interface reactivity. (Reproduced from Ghaffar *et al.* [92] under CC BY-NC-ND license.) 34

3.3 (a) The interface adhesion strength calculated in terms of W_{sep} are plotted against average interfacial equilibrium distance (d_z). A consistent decreasing nature of W_{sep} with d_z suggests a strong correlation between the two. (b) d_z vs W_{sep} plot for a subset of meta-phosphorene cases presented using two different functionals. Absolute values are different, however, the decreasing trend of W_{sep} with d_z remains intact. (Reproduced from Ghaffar *et al.* [92] under CC BY-NC-ND license.) 35

3.4 Four different representative partial density of states (PDOS) plots are given; (a) pristine phosphorene without metal contact, (b) Ti-phosphorene, (c) Au-phosphorene, and (d) Nb-phosphorene systems. In all the metal-phosphorene contact systems, a finite density of states (DOS) appear within the band gap, indicating the metallization of phosphorene at the vertical contact interface. Notably, type 1 metals exhibit lower DOS within the band gap of phosphorene than that of type 2 metals, which demonstrate a higher DOS within the band gap. The vertical axis is represented in arbitrary units because our analysis is rather qualitative in terms of DOS around the Fermi level of phosphorene. (Reproduced from Ghaffar *et al.* [92] under CC BY-NC-ND license.) 37

3.5 (a) A schematic illustration of the structure of a typical Field-Effect Transistor (FET) based on 2D materials (2DMs). The source and drain regions are contacted with metals forming metal-phosphorene contacts. An atomic structure depicting the simulated part represented by a 3D-box in addition to extended channel region is shown. Path $A - B - C - D$, denotes the interfaces charge carriers must pass encountering two interfaces: AB (vertical interface), located between the metal and the contacted phosphorene, and CD interface occurring between the contacted phosphorene and the pristine phosphorene extending into the channel part. (b) Application of modified Schottky-Mott method to calculate the Schottky barrier heights (SBHs) for the CD interface. In this diagram, E_F represents the Fermi energy of the combined metal-contacted phosphorene system. The difference between E_F and CBM/VBM yields the n-type/p-type SBH. (Reproduced from Ghaffar *et al.* [92] under CC BY-NC-ND license.) . . 38

3.6 Illustration of the work function (W_F) of the metal-phosphorene interfaces aligned into the band gap of the pristine phosphorene. The vertical bars alignment with the conduction band minima (E_C) and valence band maxima (E_V) allows us to calulcate the contact polarity in addition to the calculation of their lateral SBHs. The W_F of the bulk metal is represented in blue font, enabling the direct, side-to-side comparison with W_F of interfaced metals. (Reproduced from Ghaffar *et al.* [92] under CC BY-NC-ND license.) 39

3.7 This figures represents strong atomic overlap. Metals with lattice parameters matching those of phosphorene form interfaces with maximum atomic overlap or orbital overlap. In this study, Nb, Ta, Mo, and W reprsent such metals. (Reproduced from Ghaffar *et al.* [92] under CC BY-NC-ND license.) 41

3.8 Figures showing the planar averaged electrostatic potential prependicular to the interface: (a) Ti-phosphorene, (b) Au-phosphorene, and (c) Nb-phosphorene contact interfaces. The dotted horizontal line at 0 on the vertical axis, and the dashed red vertical line represent the Fermi level and the mid-interface point, respectively. The tunnel barrier heights can be determined from the potential difference between the peak of the potential at the mid-interface and the Fermi level. (Reproduced from Ghaffar *et al.* [92] under CC BY-NC-ND license.) . . 42

3.9 This figure depicts the interface charge density; (a) displays the mid-interface charge density (ρ) varying with work of separation (W_{sep}) for different interfaces, demonstrating a clear positive correlation of ρ with W_{sep}. (b) A visualization of ρ for Zn (type 1 metal) and Cr (type 2 metal) interfaced with phosphorene. It can be noted that the Zn-based phosphorene interface exhibits the lowest ρ, while the Cr interface presents an example for the high ρ. (Reproduced from Ghaffar *et al.* [92] under CC BY-NC-ND license.) 43
3.10 The planar averaged charge density, perpendicular to the interface is presented for 3 distinct representative phosphorene-metal cases. (a) Ti-phosphorene is given as an example of highly adhesive type 2 metals, (b) Au-phosphorene represents the lower adhesive metals (type 1), and (c) Nb-phosphorene is an example for the cases with broken intra layer armchair P-P bond upon metal contact. (Reproduced from Ghaffar *et al.* [92] under CC BY-NC-ND license.) 44
3.11 The resistivity of all the metals employed for the interface construction with phosphorene. Sc, Ti, and V are the metals with highest resistivity among all the metals used in this study. (Reproduced from Ghaffar *et al.* [92] under CC BY-NC-ND license.) 44

4.1 Schematic diagram of a typical Field Effect Transistor (FET). The dotted circular part has been simulated as illustrated on the RIGHT. Both the pristine-WS_2/Metal and doped-WS_2/Metal interface is modeled as depicted in the figure. 48
4.2 Binding energy for all the systems, both with and without S-substitution. To facilitate a direct comparison of relative variations among different cases in relation to the pristine case, these systems are categorized into three distinct groups: 1. p-type dopants(C, P, N), 2. n-type dopants (F, Cl), and 3. neutral dopants (O). 49
4.3 Bar graph showing the lateral Schottky barrier height (SBH) calculated using a modified Schottky-Mott model, with the vacuum level aligned between contacted WS_2 at the electrode region and WS_2 in the channel. 52
4.4 The top two plots describe the Schottky barrier height (SBH) utilizing the idealized Schottky-Mott model and the subsequent alteration due to Fermi level pinning (FLP) calculated using Fat band technique. Please note that the Fat band method could not be employed for Sc and Ti due to their highly reactive nature, which destroys the WS_2's band-edges. The bottom two plots, with the help of bar plots, compare the SBH modification across different substituted interfaces concerning the pristine WS_2/metal interface. 53
4.5 Electronic bandstructure and atom-projected DOS as applied for the fat band technique to predict the vertical SBH of Au. Black and blue-colored arrows denote the n-type and p-type SBH, which originates at the Fermi level and points to the CBM and VBM, respectively. (a) Pristine-WS_2-Au(111), (b) O-doped-WS_2-Au(111), (c) C-doped-WS_2-Au(111), (d) Cl-doped-WS_2-Au(111) 54
4.6 Tunneling Probability (T) analysis for all the interfaces with/without doping. T values larger than 1 imply no tunneling barrier at the interface. 55
4.7 Metal-induced gap states (MIGS) calculated over all the electronic states within the band gap. We can observe variations in MIGS depending on metal and dopant chemical reactivity. 57

4.8 Planar-averaged electrostatic potential along the interface in the z-direction. The red dotted line represents the Fermi level. The dashed circular portion, which has been zoomed in on the right, is approximated as a rectangular shape to facilitate the application of quantum mechanical tunneling theory. 59
4.9 Planar average charge density (PACD) due to doping compared to the pristine contact. The dQ-values indicate the amount of charge transferred towards the WS_2 side upon substitution. The solid black line represents the interface mid-point, while the red/blue dotted lines indicate the locations of metal/WS_2 atomic planes along the z-direction. 61
4.10 Change in the interface dipole moment (ΔP) due to doping. The trend in dipole change consistently correlates with the Fat band Schottky barrier heights. . . . 61

List of Tables

3.1 A list of lattice characteristics utilized to construct phosphorene supercell (SC) and the metal SC to realize the commensurate metal-semiconductor contact interfaces, are presented. In addition to relevant parameters regarding interface modeling, a comprehensive summary of calculated properties are also compiled in this table. (Reproduced from Ghaffar *et al.* [92] under CC BY-NC-ND license.) 33
3.2 The following table represents the comparison of SBHs ($\Phi_{B,n}$ and $\Phi_{B,p}$) with earlier reported values available in published literature. 39

4.1 Vertical SBH for all the interfaces has been calculated employing fat band technique, as given here along with other relevant parameters. The E_g, Φ_n^V, and Φ_p^V denote the band gap, n-type SBH, and p-type SBH, respectively in the unit of eV. Metal-induced gap states (MIGS) are given in the units of states/eV/Å^3. . . 50

Chapter 1

Introduction

1.1 Background

The emergence of advanced computational capabilities, accompanied by the development of computational methodologies, has led to remarkable progress in the field of computational materials modeling. This progress has greatly facilitated the exploration of diverse material compositions and configurations, encompassing solids, liquids, and molecules, across various domains of physics and chemistry. As a result, we have witnessed a transformative shift in the pursuit of groundbreaking materials discovery and the modeling of interfaces within heterogeneous structures. These advancements have far-reaching implications, particularly in the field of electronics, optoelectronics, and biomedical applications. In the context of materials science, these advancements have enabled researchers to peer into the complex electronic and atomic structures of materials with unprecedented precision. By accurately simulating the behavior of atoms and electrons, scientists can predict materials properties, discover new materials, and optimize the existing ones utilizing computational codes developed for this purpose. This has profound implications for industries ranging from electronic to aerospace, as it expedites the development of high-performance materials for different applications. More importantly, computational modeling has the potential to reduce the cost of experiments by helping researchers focus their efforts on the most promising and relevant materials combinations. By simulating the properties and behavior of materials, for example in the electronics industry, we can quickly identify which combinations of semiconductor and metal interfaces as electrode materials are likely to exhibit desirable characteristics or meet specific criteria, allowing researchers to fine-tune interface materials for specific applications without the need for extensive trial-and-error experimentation.

Ab initio density functional theory (DFT) calculations have significantly advanced the field of electronics by providing detailed insights into the properties of various materials, including semiconductors and metals. DFT calculations enable researchers to predict and understand the electronic structure of materials from first principles. There has been a surge of DFT-based studies [1, 2, 3, 4] devoted to electronic structures and properties of material surfaces and interfaces. This knowledge is vital for understanding charge transport at interfaces giving insights into a specific device application, underscoring the capabilities of the first principles-based computational framework.

Due to their exceptional mechanical, optical, and electronic properties, two-dimensional materials (2DMs) have attracted significant attention in the scientific community over the last fifteen years [5, 6]. Among these materials, graphene and transition metal dichalcogenides

(TMDs) are being investigated as possible candidates for sub-2nm CMOS technology nodes [7, 8, 9]. Nevertheless, the zero band gap of graphene limits its usefulness in low-power logic circuit applications; on the other hand, phosphorene and TMDs are promising 2D semiconductors that could replace 3D semiconductors in the next generation of electronic industry. However, high contact resistance at the 2D-semiconductor-based metal-semiconductor (MS) interface is a major barrier to the realization of 2DM-based FETs, even though metal contacts are important for allowing carrier movement between the circuit back-end and FETs. This challenge must be addressed because low contact resistance can seriously impair the overall performance of FETs. Moreover, in the atomic thin limit of 2DMs, contact resistance is primarily controlled by the characteristics of the metal-semiconductor interface. For this reason, a thorough investigation of MS interface is necessary to determine the factors influencing contact resistance and gain insights to further the technological understanding of 2DM-based FETs.

To better understand appropriate contact properties, we have computationally modeled several metal-semiconductor contacts with phosphorene and transitional Metal dichalcogenide WS_2 semiconductors for next-generation electronic and optoelectronic devices. In the last few years, various metal-phosphorene interfaces have been studied: both theoretically and experimentally. It is quite difficult to work with such sensitive materials as 2D semiconductors when fabricating devices experimentally; the potential for imperfect interfaces casts a shadow over the interface properties, as impurities like resist residues or other fabrication anomalies can significantly affect the contact resistance. As a result, it is increasingly challenging to derive a clear relationship between the contact resistance and interface properties from experiments. On the other hand, addressing the challenge of contact resistance at the metal/semiconductor interface, in TMDs, continues to be difficult due to the inevitable Fermi level pinning (FLP) effect near the conduction band minima. Although various interface engineering techniques have been explored to mitigate FLP by reducing the chemical interaction between the metal and semiconductor, they often result in lower adhesion and higher tunneling resistance, leading to poor interface quality. Moreover, a promising solution to overcome these limitations lies in the use of substitutionally doped semiconductor/metal interfaces. Through first-principles calculations, we have conducted a comprehensive study on S-substituted WS_2-metal interfaces involving commonly used metals such as Ag, Au, Cu, Pd, Pt, Sc, and Ti. Additionally, we have explored the incorporation of non-metallic dopants, namely C, Cl, N, F, O, and P into the WS_2 surface. Our analysis focused on several critical parameters including adhesion strength, Schottky-barrier height (SBH), tunnel barrier, and charge transfer across the interface enable us to discern their relative trends. Notably, our results reveal an enhancement trend in FLP with the dopants ranked as F < O < Cl, elucidating their varying effects, while the strength of FLDP displays a distinct pattern determined solely by the n/p-dopant characteristics, varies as N < P < C. This observation rules out the possibility of FLDP being influenced by MIGS (metal-induced gap states), which is a departure from other FLDP techniques. Furthermore, contrary to existing methods, our study demonstrates that substitutionally doped interfaces undergo FLDP while maintaining enhanced adhesion strength and lower tunneling barrier at the interface.

1.2 Motivation

The "International Roadmap for Devices and Systems" (IRDS) [10] is a comprehensive series of reports and forecasts by the IEEE that predict upcoming technology trends in various domains, including semiconductor manufacturing, design, packaging, and other aspects related to semiconductor development. It is a collaborative effort involving key players in the semiconductor

industry, such as manufacturers, equipment suppliers, and research organizations. In its 2022 report, titled "Scope of Beyond-CMOS Focus Team," IRDS focuses on two vital points: 1) Integration of heterogeneous structures in new technology, 2) Encouraging the development of innovative information processing systems beyond CMOS (complementary metal-oxide-semiconductor). The report anticipates that integrating 2D materials into field-effect transistors (FETs) holds significant promise for future very large-scale integration (VLSI) technology, which aligns with the goal of advancing semiconductor technology. The drive for miniaturizing FETs in next-generation devices is a key area of research, primarily because of its role in extending Moore's law [11]. Moore's law posits that the number of transistors on an integrated chip (IC) will double approximately every two years, while the cost of computers will be halved. 2D semiconductors are particularly promising in this regard. Their unique structure, which does not require a three-dimensional crystal, allows for ultra-thin body thicknesses of under 1nm in their monolayer form, with no dangling bonds. Moreover, 2D semiconductors exhibit exceptional electronic properties, surpassing what is achievable in three-dimensional (3D) crystals when scaled down to such thicknesses. These characteristics position 2D channel materials as strong contenders to continue the trajectory of Moore's Law. Nonetheless, the IRDS report also recognizes the pressing need for improved contact engineering schemes. This is essential to effectively address the challenges associated with source/drain contacts in FETs, with a key focus on reducing contact resistance and unlocking the intrinsic performance potential of these transistors.

There are hundreds of 2D semiconductors that have been explored. Among them, two of the most extensively studied materials are phosphorene (which is a single layer of black phosphorus) and transition metal dichalcogenides (TMDs) like MoS_2, WS_2, and WSe_2, etc. This is because they all possess great electronic properties. While it is rather important to note, that most 2D semiconductors share common features such as a tunable band gap, anisotropy, high carrier mobility, strong light-matter interaction, good thermal conductivity, thin structure, and the ability to form heterostructures, they also have unique properties. Due to these differences, more research has been directed toward exploring certain 2D materials over others for their specific potential applications. In line with this, graphene is one such 2D material. However, its lack of a band gap makes it challenging to use in modern logic circuits without some engineered solutions to create a band gap. On the other hand, phosphorene is gaining attention as a 2D material because its band gap can be adjusted (0.3 eV for the bulk form and 2.0 eV for a single layer), making it suitable for high-speed transistors [12]. Additionally, TMDs exhibit moderate to high band gaps (1.8 eV in bulk and 2.5 eV in monolayer), which makes them excellent candidates for ultra-small and low-power transistors [13]. However, the successful integration of 2D materials in large-scale industry applications is contingent on realizing the Ohmic or low energy barrier metal interconnects, as they are crucial factors determining the final performance of devices [14, 15, 16].

Research on various metal-phosphorene contacts has gained significant attention, both in experimental and theoretical domains, over the past few years. However, in experimental studies, the elucidation of interface properties is often complicated by potential imperfections. Factors, like resist residues or fabrication anomalies on the interface, can substantially influence contact resistance. Consequently, establishing a clear relationship between contact resistance and interface properties from experimental studies can be challenging. On the theoretical front, several first-principles-based studies have explored metal-phosphorene contacts. Nevertheless, these studies frequently focus on a limited set of metals, making it challenging to cross-reference and understand the connection between interface properties and different metals. For instance, previous studies by Pan *et al.* [17] and Maity *et al.* [18] indicate that Ti-phosphorene forms a

pure Schottky contact, while Chanana *et al.* [19] suggest an intermediate contact. Additionally, Gong *et al.* have demonstrated that Cu forms an excellent Ohmic contact, while Pan *et al.* have observed both finite Schottky and tunnel barriers at the metal-phosphorene interface. These divergent results could also stem from variations in simulation conditions, including the choice of functionals, pseudo-potential, and interfaced metal surfaces.

To achieve a comprehensive and unbiased comparison among different contact metals, it is imperative to simulate them using consistent methods and input parameters. Furthermore, it's crucial for these metals to form mechanically stable contacts while maintaining favorable electrical properties. The interplay between mechanical strength and electrical performance is a key factor in identifying the optimal metal for contact with a specific 2D material, a facet that has been somewhat lacking in prior research. This study addresses these challenges by conducting an extensive *ab initio* investigation of metal and monolayer phosphorene interfaces. It offers a systematic analysis of both mechanical and electrical properties, exploring the interfaces between 18 potentially suitable metals Ag, Al, Au, Co, Cr, Cu, Mo, Nb, Ni, Pd, Pt, Ru, Sc, Ta, Ti, W, V, and Zn and monolayer phosphorene. The study systematically analyzes various metal-phosphorene interfaces to characterize the factors influencing their mechanical and electrical properties. To achieve this, the work of separation (W_{sep}) is calculated to gauge the adhesion strength of the metal contacts. Concurrently, the density of states, Schottky barrier height, tunnel barrier height, and mid-interface charge density calculations are performed to assess electrical performance. This comprehensive approach establishes a strong link between the mechanical and electrical performance of the metal contacts and their interface chemistry. This not only enables a fair comparison between different metals but also sheds light on the intricate relationship between mechanical and electrical properties.

For WS_2-metal interfaces, several experiments on metal/TMD contacts, similar to phosphorene, have reported discrepancies between idealized contact and observed behavior, owing to the presence of unintentional chalcogen vacancies [20, 21, 22, 23]; additionally, external dopants found in the experimental samples have been observed to significantly influence the post-characterization of device properties. Chalcogen vacancies, specifically, can result in the creation of deep acceptor trap states. This occurrence leads to both short and long-range Coulomb charge scattering, which subsequently contributes to the degradation of hole-mobility. The constrained movement of holes, due to the defects states, within the valence band is the primary factor behind this degradation, as referenced in [24, 25, 26]. To circumvent this issue, various approaches have been investigated including, vacancy healing [27], surface coating [28], doping [29], Thiol chemistry [30], and charge transfer [31]. However, it remains a challenge to deal with and understand the interplay of various defects. On the other hand, it is fascinating to note that the defects are also crucial to modulating the properties of TMDs for various applications [32, 33, 34]. In particular, the fabrication of functional devices through substitutional doping in 2D materials has been the subject of extensive research [35, 36, 37, 38, 39, 40, 41, 42, 43, 44, 45], with promising results for tuning and selectively modulating their optical and electronic properties. This poses a tradeoff between the defect-assisted modulation and target properties, making it highly important to characterize the properties of different dopants across a diverse set of metallic electrodes for transistor application. For instance, interface-engineered contacts with reduced FLP exhibit lower p-type SBH at the cost of low-quality interface and higher tunnel barriers.

In general, TMDs exhibit higher stability when combined with metal-rich compositions rather than chalcogen-rich ones, as discussed by Li *et al.* [46]. This insight clarifies why chalcogen substitution is more energetically favorable than substituting the transition metal (TM) in

these materials. Moreover, it is worth noting that S-vacancies introduce shallow trap states, while TM vacancies lead to deep-trap states. In line with this, Kim *et al.* [47] conducted experiment highlighting that S-vacancies in WS_2 result in a higher concentration of impurities and disorders compared to W-vacancies. This occurrence leads to a tenfold increase in doping concentration and a fourfold higher Coulomb scattering coefficient, owing to the formation of shallow doping levels [48] within the band gap, which makes S-vacancy chemically more active than W-vacancy. Furthermore, Wang *et al.* [49] suggest that various defects, including B, C, N, O, F, and P doping, as well as S-vacancies, can activate the inert basal planes of 2H-phase MoS_2, introducing impurity states at lower energy levels. These insights partly explain why so many recent studies have focused on improving device performance by employing non-metallic dopants like P [37, 44, 45], C [37, 44, 45], N [26, 39, 45], F [38, 43, 50], O [42, 45, 51], and Cl [41, 45, 52, 53, 54]. Nevertheless, quantifying the relative performance of different chalcogen-substituted WS_2/metal Interface across various metals with differing chemical properties has remained a longstanding challenge. In this context, our study encompasses an array of ubiquitous dopants, including P, C, N, O, and F, alongside metals such as Ag, Au, Cu, Pd, Pt, Sc, and Ti. Our aim is to offer a more comprehensive understanding of the tunability in their contact properties within both substituted and unsubstituted systems.

Considering the need for consistent simulation criteria when characterizing relative contact properties of various complex characteristics pertaining to 2D-semiconductor/metal interfaces, our investigation carries added significance. We believe that our exploration of the factors affecting phosphorene-metal interfaces and S-substituted WS_2/metal contacts can significantly contribute to fundamental research and offer valuable insights for experimental device fabrication in next-generation applications.

1.3 Problem Statements

The following research objectives have been addressed in this work:

- Computational modeling of metal/2D-semiconductor interface and understanding the factors leading to contact resistance?
- How do 2D-semiconductors namely, phosphorene, and WS_2 lead to varying interface properties upon contact with different metal electrodes?
- Tunability of the WS_2/metal interface properties under doping with different dopants
- Demonstration of reduced hole Schottky barrier height with substitutional doping in transition metal dichalcogenide (TMD), WS_2/metal contacts

1.4 Outline

This work is divided into 5 chapters.

- Chapter 1: The first chapter offers an introduction to this research, encompassing its foundational context. Within, it delves into the driving factors, significance, and the research's boundaries. Additionally, it outlines the principal goals and explores the current body of literature.

- Chapter 2: Within the methodology section, we have incorporated several key elements that guide our work. This chapter describes the fundamental principles underpinning our modeling of the 2D semiconductor/metal interface. These involve modeling criteria, computational tools, simulation parameters, as well as validation and verification against existing literature pertaining to our chosen methodology.

- Chapter 3: This chapter provides an in-depth examination of the interface between metal and phosphorene.

- Chapter 4: Chapter 4 explores the intricate aspects of WS_2/metal contact interfaces in the context of substitutional doping.

- Chapter 5: In the last chapter, we conclude our work by discussing the following crucial aspects: brief summary of the research objective, key findings, hypothesis involved, address limitation, implication, and future direction, followed by concluding remarks.

Chapter 2

Methodology

2.1 Theoretical uderpinning of *ab initio* methods

Ab initio calculations, also known as first-principles calculations are a computation framework firmly grounded in the fundamental principles of quantum mechanics to predict the electronic structure of atoms, molecules, and solids. Modern computational materials science and quantum chemistry heavily rely on the *ab initio* calculations that have become an indispensable tool for materials research. However, the *ab initio* calculations are computationally intensive, especially for large and complex systems. High-performance computing or supercomputing facilities are often required to perform accurate calculations in a reasonable timeframe. The inherent complexity in the calculation arises because many-body Schrödinger's equation requires to be solved. A modestly average atomic structure is generally composed of hundreds of correlated particles, making the calculations computationally quite demanding. Several, models and approximations have been devised to deal with the complexity of *ab initio* calculations. In the following sections, we will be laying out the foundation of first-principles calculations.

2.2 Many-Body Schrödinger Equation

The many-body Schrödinger equation is a fundamental equation describing the behavior of a system of interacting particles, such as electrons in an atom or molecules in a chemical reaction. It is an extension of the standard Schrödinger equation to systems with multiple particles and takes into account their mutual interactions. The many-body Schrödinger equation for a system of N particles is typically expressed as,

$$\hat{H}\Psi(\mathbf{r}_1, \mathbf{r}_2, \ldots, \mathbf{r}_N) = E\Psi(\mathbf{r}_1, \mathbf{r}_2, \ldots, \mathbf{r}_N), \tag{2.2.1}$$

where H is the Hamiltonian operator, which represents the total energy of the system.

$$\hat{H} = -\frac{\hbar^2}{2m_e}\sum_i \nabla_i^2 - \frac{1}{4\pi\epsilon_0}\sum_{i,I}\frac{Z_I e^2}{|r_i - R_I|} + \frac{1}{2}\frac{1}{4\pi\epsilon_0}\sum_{i\neq j}\frac{e^2}{|r_i - r_j|} \tag{2.2.2}$$

where electrons are represented by lowercase subscripts and coordinates r_i and nuclei are denoted by uppercase subscripts, coordinates R_I, atomic number Z_I, electronic charge e , and mass of the nuclei M_I. It includes kinetic energy, potential energy, and any additional terms

associated with the interactions between particles. $\Psi(\mathbf{r}_1, \mathbf{r}_2, \ldots, \mathbf{r}_N)$ is the wave function of the system, which depends on the positions of all N particles. The wave function encodes the quantum state of the system and contains information about the probability distribution of finding the particles at specific positions. E is the total energy of the system, which is an eigenvalue of the Hamiltonian operator. It represents the energy associated with the quantum state described by the wave function ($\Psi(vecR)$). Solving the many-body Schrödinger equation is a challenging task, especially for systems with a large number of particles, such as complex molecules or solids. Approximation methods, such as Hartree-Fock theory, density functional theory (DFT), and various forms of quantum Monte Carlo methods, are often employed to find approximate solutions to this equation for real-world systems. Solving Eq. (2.2) involves the evaluation of different parts contributing to the Hamiltonian. However, the nuclear kinetic energy, which is inversely proportional to the mass of the nuclei ($1/M_I$) can be neglected. For the most part, often we focus our attention on the electronic aspect of the problem while assuming the nuclei remain fixed. This approximation is known as the Born-Oppenheimer (adiabatic) approximation [55]. Consequently, the final term, which represents the interaction between nuclei themselves, becomes a constant and, as a result, can be incorporated into the reference energy level. Eventually, the Hamiltonian that forms the foundation of the theory for electronic structure calculation is reduced in a form composed of the first three terms: 1) the kinetic energy of the electrons, 2) the electron-nucleus interaction, and 3) the electron-electron interaction. This can be given as follows:

$$\hat{H} = \hat{T}_e + \hat{V}_{en} + \hat{V}_{ee}, \tag{2.2.3}$$

This equation represents the fundamental challenge in understanding the electronic structure of various systems. The first and last terms in the equation are common to all problems, while the unique characteristics of each system are found in the middle term — a potential that affects all electrons equally. Dealing with this Hamiltonian is a complex task due to the challenging nature of the two-body electron–electron interaction term ($\hat{V}_{ee}$), therefore, a theoretical framework to approach such a task is required.

2.3 Mean-field Theory

Mean-field theory in the context of electronic structure calculations is a fundamental approach used to simplify the many-body quantum mechanical problem of interacting electrons in a solid-state system. It forms the basis for several widely used methods in condensed matter physics and quantum chemistry. Mean-field theory simplifies electronic structure calculations by approximating electron-electron interactions into a system of non-interacting electrons, making them computationally tractable for a wide range of materials and systems. Mean-field solutions, when wisely selected, can offer valuable and understandable results. They serve as a foundation for studying the impact of correlation effects. In many-body theories, the 'particles' involved can either be the actual particles with their original properties or, more commonly, they can be solutions obtained from a set of mean-field equations designed to simplify the many-body problem. Some important mean-field methods for handling electronic interactions are the Hartree–Fock approximation (HFA), the Weiss mean-field, and density functional theory (DFT). In the next section, we will describe the theoretical formulation of the mean-field theories.

2.3.1 Challenges and Solution of Mean-field Theories

Despite the ubiquitous application of the Mean-field approaches for electronic structure calculation, their application for some of the most important materials such as strongly correlated materials, quantum magnetic materials, materials involving defects, electronic excitation, etc., remains challenging. The Mean-field framework fails to adequately capture electron-electron correlation effects, particularly in strongly correlated materials. Post-HF methods such as Moller-Plesset perturbation theory (MP2) and coupled cluster theory (CCSD) can be used to account for electron correlation beyond the mean field level. In DFT, one can adopt the hybrid functionals or advanced exchange-correlation functions to improve the treatment of correlation effects. Also, a significant amount of correlation energies can be recovered by including van der Waals dispersion correction, which accounts for longe range interaction. Another challenge comes from the choice of basis-set. An incomplete basis set can give rise to erroneous results. Using an appropriate basis for the specific material under investigation with a sufficiently larger cutoff for basis set expansion can effectively improve the overall accuracy. Furthermore, for solid crystals with periodic lattice symmetry, there is an issue, generally known as a finite-size effect. It originates from the use of small simulation cells that can introduce inaccuracies resulting from an interaction between atoms/electrons near the edges of the cell, which are different from those in the bulk region. This introduces artificial boundary effects responsible for this type of error, which can be dealt with by using a sufficiently large supercell size. A larger supercell ensures the representation of periodicity and reduces the interactions across periodic images significantly. Additionally, an adequate sampling of k-points inside the reciprocal lattice (Brillouin zone) can provide one with more accurate ground state properties.

2.4 Density Functional Theory

Density Functional Theory (DFT) is a quantum mechanical modeling approach widely used in computational materials science. It calculates the electronic structure properties of materials, predicting their behavior without solving the many-body Schrödinger equation directly. DFT approximates the electronic density rather than wavefunctions, making it computationally efficient. It's employed to study diverse material properties, such as electronic band structures, energetics, and structural optimizations, providing valuable insights for designing and understanding materials at the atomic and molecular levels [56, 57, 58].

The Hohenberg-Kohn theorem is a fundamental concept in density functional theory that establishes the relationship between the electron density and the external potential $\hat{V}_{ext}$ of a quantum system. The theorem is usually summarized in two parts:

Theorem 1: There exists a one-to-one correspondence between the external potential of a quantum system, denoted as $V(\mathbf{r})$, and its ground-state electron density, denoted as $n(\mathbf{r})$. In other words, for a given electron density, there is only one corresponding external potential, and vice versa.

Theorem 2: The ground-state energy (E_0) of the system is a unique functional of the electron density ($n(\mathbf{r})$). This functional is denoted as $E_0[n(\mathbf{r})]$, and it can be expressed as,

$$E_0 = E_0[n(r)] = \min_{\Psi \to n(r)} \langle \Psi | \hat{H} | \Psi \rangle, \tag{2.4.1}$$

where E_0 represents the ground-state energy, corresponding to the electron density ($n(\mathbf{r})$), $\Psi(\vec{R})$ is the many-electron wave function that yields $n(\mathbf{r})$. The notation $\min_{\Psi \to n(\mathbf{r})}$ indicates that the

minimum ground state energy is obtained by finding the wave function (Ψ) that corresponds to the given electron density $n(\mathbf{r})$. The key insight of the HK theorem 2 is that, for a given electron density, the ground-state energy is determined solely by that density, and the specific form of the wave function is not needed to compute the energy.

The Hohenberg-Kohn theorem paved the way for the development of density functional theory (DFT), which seeks to approximate the energy functional ($E_0[n(\mathbf{r})]$) and make practical calculations of electronic structure properties based on the electron density. In DFT, the exchange-correlation functional is introduced to approximate the correlation effects, enabling the computation of ground-state energies and other electronic properties for a wide range of systems.

2.4.1 Kohn-Sham Equation and Exchange-correlation Functionals

The central idea in the Kohn-Sham equation is to replace the complex many-body wavefunction (Ψ) with a set of non-interacting single-particle wavefunctions (ψ_i) that are subject to an effective potential such that the electron density of the non-interacting system matches the real electron density of the interacting system as,

$$\hat{H}_{\mathrm{KS}}\psi_i(\mathbf{r}) = \epsilon_i\psi_i(\mathbf{r}), \tag{2.4.2}$$

where,

$$\hat{H}_{\mathrm{KS}} = \left(-\frac{1}{2}\nabla^2 + v_{\mathrm{eff}}(\mathbf{r})\right), \tag{2.4.3}$$

and ψ_i and ϵ_i represent the single-particle wavefunction and single-particle energy, respectively. The many-body wavefunction (Ψ) as a product of single-particle wavefunctions (ψ_i) for non-interacting electrons and an antisymmetrization term (Slater determinant) to account for the Pauli exclusion principle is given as,

$$\Psi(\mathbf{r}_1, \mathbf{r}_2, \ldots, \mathbf{r}_N) = \frac{1}{\sqrt{N!}} \begin{vmatrix} \psi_1(\mathbf{r}_1) & \psi_2(\mathbf{r}_1) & \ldots & \psi_N(\mathbf{r}_1) \\ \psi_1(\mathbf{r}_2) & \psi_2(\mathbf{r}_2) & \ldots & \psi_N(\mathbf{r}_2) \\ \vdots & \vdots & \ddots & \vdots \\ \psi_1(\mathbf{r}_N) & \psi_2(\mathbf{r}_N) & \ldots & \psi_N(\mathbf{r}_N) \end{vmatrix} \tag{2.4.4}$$

The Kohn-Sham Hamiltonian ($\hat{H}_{\mathrm{KS}}$) in Eq. (2.4.2) includes an effective potential $v_{\mathrm{eff}}(\mathbf{r})$, which is represented as,

$$v_{\mathrm{eff}}(\mathbf{r}) = v_{\mathrm{ext}}(\mathbf{r}) + v_{\mathrm{H}}(\mathbf{r}) + v_{\mathrm{XC}}(\mathbf{r}), \tag{2.4.5}$$

where $v_{\mathrm{H}}(\mathbf{r})$ is the Hartree potential resulting from the electron-electron interactions, $v_{ext}(\mathbf{r})$ is the external potential due to nuclei in the system, and $v_{XC}(\mathbf{r})$ denotes the exchange-correlation potential. The exchange-correlation potential encapsulates both exchange effects between elections with the same spins and correlation effects between electrons. It is defined in terms of the exchange-correlation energy function $E_{\mathrm{XC}}[n]$. The analytical expression of the exchange-correlation potential is not known, therefore, one has to rely on the approximation as,

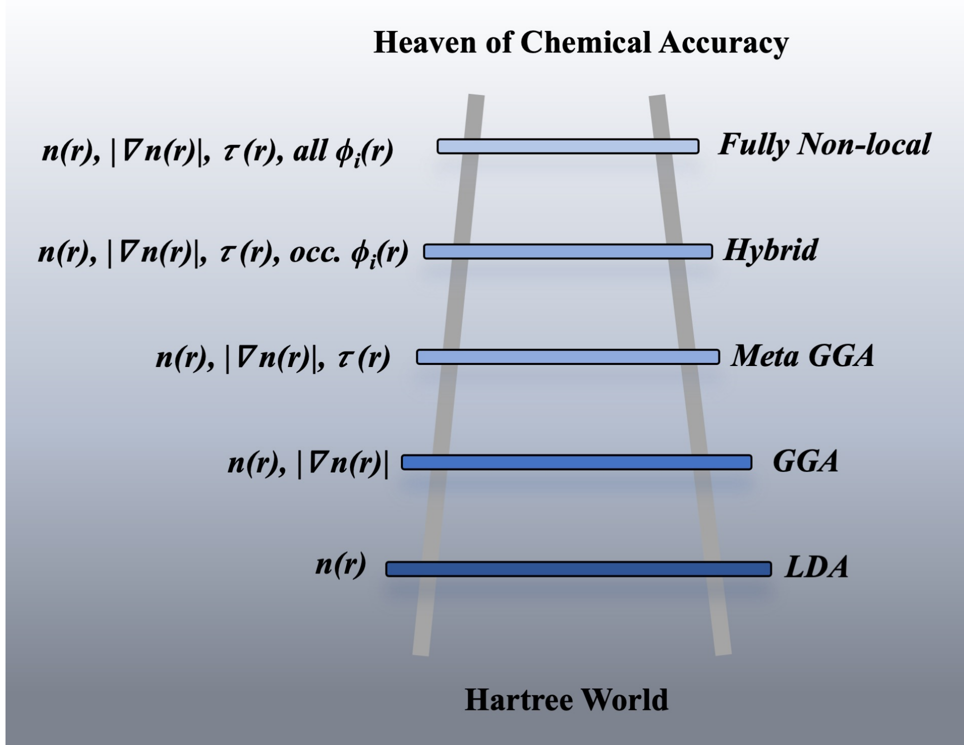

Figure 2.1: Jacob's ladder representing the hierarchy of approximations used in electronic structure calculation. The computational cost and accuracy largely depend on the specific condition and requirement.

$$v_{\mathrm{XC}} = \frac{\delta E_{\mathrm{XC}}[n]}{\delta n} \tag{2.4.6}$$

The specific form of $E_{XC}[n]$ depends on the approximation for exchange-correlation effects, such as the local density approximation (LDA), generalized gradient approximation (GGA), or more sophisticated functionals like hybrid functionals. There is a hierarchy of approximations used in electronic structure calculations for different level of exchange-correlation functionals depending upon a trade-off between computational cost and accuracy, which is called as Jacob's ladder [59]. The following Fig. 2.1 depicts how Jacob's ladder typically looks for different types of exchange-correlation functionals.

At the bottom rung of the ladder is Hartree's theory, which is based on the mean-field approximation. This method is computationally efficient, but its accuracy is highly limited as it does not include the electron correlation effects. LDA partially considers both exchange-correlation effects, though it borrows from the theory of electron gas. One step up from the LDA, GGA incorporates gradients of electron density for the exchange-correlation formulation, providing better accuracy for molecular and solid-state properties. Subsequent rungs are further improvements to recover correlation energy by employing different schemes for more and more accurate calculations involving a lesser number of approximations. It is important to mention that meta-GGA, and beyond the level of theory, though yields higher accuracy. However, they are highly computationally inefficient. Moreover, the GGA funtional that is used in the present study is computationally efficient and accurate enough for a wide range of materials science and its applications, including ground-state properties, structural optimization, and

many other electron structure properties.

2.5 Self-Consistent Calculations

In DFT, a self-consistent calculation is an iterative process used to find the electronic density that minimizes the total energy of the system by solving the single-particle Kohn-Sham (KS) equation. One starts with an initial guess for the electron density (n_0), and the corresponding KS equation for the given electron density to find the single-particle wavefunction ψ_i and eigenvalues ϵ_i. This newly obtained wavefunction is used to calculate a new electron density:

$$n(\mathbf{r}) = \sum_{i}^{N_{\text{electrons}}} |\psi_i(\mathbf{r})|^2. \tag{2.5.1}$$

In the next step, the new electron density is checked if it meets the convergence criteria. This iterative process is repeated until the electron density no longer changes significantly between iterations, indicating that a self-consistent solution has been reached as illustrated in Fig. 2.2. Self-consistency ensures that the electronic structure of the system is accurately described within DFT. As is explained in the next subsection, the KS equation is numerically solved by introducing the basis set to expand the KS wavefunctions and involves finding the set of expansion coefficients (c_{ij}) that minimizes the total energy.

2.5.1 Basis-set expansion

By expanding the KS wavefunctions in terms of basis set functions, the differential KS equation can be reduced into a matrix form, which is numerically solved in a computationally efficient way. There are various types of basis sets available, such as plane waves, Gaussian basis sets, and Slater-type (atomic) orbitals, wavelets, linearized augmented plane waves, numerical basis sets on a real-space grid, etc. The choice of the basis set depends on the nature of the problem and the level of accuracy required for a particular crystal. Localized basis sets, which are composed of atomic orbitals, are advantageous for large-scale applications: in fact, linear scaling methods have been devised with localized basis sets [60]. Note that standard DFT calculations are based on cubic scaling because of the orthonormality constraint of the KS equation in Eq. (2.4.2). While localized basis sets can be efficiently applied to molecular systems, their application to solid crystals does not yield as accurate results as plane-wave approaches due to the lattice periodicity of such crystals.

The basis set consists of a set of basis functions (typically denoted as $\phi_i(\mathbf{r})$). These basis functions are used to expand the wavefunctions of the electrons in the system as follows:

$$\psi_i(\mathbf{r}) = \sum_{j} c_{ij}\phi_j(\mathbf{r}), \tag{2.5.2}$$

where $\{c_{ij}\}$ are expansion coefficients. Our study involves the solution of periodic potential for a heterostructure constructed with a semiconductor/metal interface. For such periodic systems, plane-wave basis sets are the most appropriate basis, which is often expressed as,

$$\psi(\mathbf{r}) = \sum_{\vec{k}} c_{\vec{k}} e^{i\mathbf{k}\cdot\mathbf{r}}, \tag{2.5.3}$$

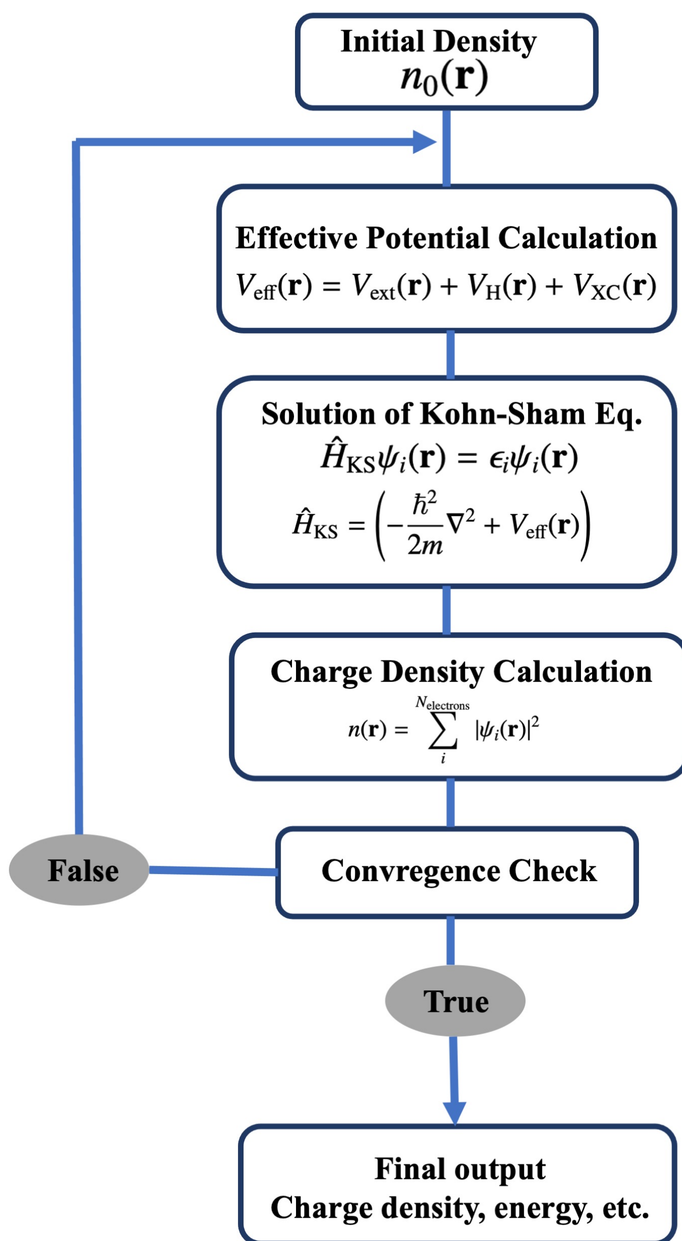

Figure 2.2: SCF cycle used to iteratively solve the Kohn-Sham equation in a DFT calculation.

The electronic Hamiltonian ($\hat{H}$) is expressed in terms of the basis functions, and the density matrix ($\hat{\rho}$) is constructed based on the electron occupations in the second quantization formulation,

$$\hat{H} = \sum_{ij} H_{ij} c_i^\dagger c_j, \tag{2.5.4}$$

$$\hat{\rho} = \sum_{ij} P_{ij} c_i^\dagger c_j \tag{2.5.5}$$

with H_{ij} representing the matrix elements of the Hamiltonian, and P_{ij} denotes the matrix elements of the density matrix. These equations are formulated in terms of the basis functions and involve finding the set of expansion coefficients ($\{c_{ij}\}$) that minimize the total energy.

2.5.2 Brillouin-Zone Integration

Our work involves crystals with periodic boundary conditions. To get essential physical insights into the electronic properties of such systems, the electronic wave functions are subject to periodic boundary conditions. Brillouin zone integration is a natural way to handle these periodic conditions mathematically. The integration is performed over the first Brillouin zone only, which holds all the information needed to describe the electronic properties of the entire crystal. By integrating over a single unit cell in reciprocal space (k-space) rather than the entire crystal, calculations become more manageable when dealing with a large and complex crystal structure.

2.5.3 Smearing

In a crystal system, electrons follow the Aufbau principle, filling the lowest Kohn–Sham eigenstates up to a certain energy level, resembling to the step-like Fermi–Dirac distribution at absolute zero temperature. However, metallic systems do not have steplike occupancy (0 or 1). For such systems achieving convergence can be challenging because tiny perturbations can alter electron occupancy. Smearing helps stabilize DFT calculations, particularly when dealing with degenerate or nearly degenerate electronic states near the Fermi level, ensuring convergence and providing a continuous representation of electron occupation. To mitigate these fluctuations, one approach involves electron smearing, allowing for fractional occupancies f_{nk}.

Two of the most commonly used smearing methods in DFT are Fermi-Dirac and Gaussian smearing methods.

Fermi-Dirac Smearing: In the Fermi-Dirac smearing method, the electron density smearing uses the Fermi-Dirac distribution function as given by,

$$f(E) = \frac{1}{1 + e^{(E - E_f)/k_b T}}, \tag{2.5.6}$$

where $f(E)$ denotes the occupation probability of an electron in a state with energy E, E_f denotes the Fermi energy that represents the highest occupied energy level. k_b and T are the Boltzmann constant and temperature, respectively. If we use a step-like electron distribution at absolute zero, we usually encounter an issue of convergence for the systems with degenerate

electron states near E_f. To resolve this, the Fermi-Dirac method smears out the electrons allowing fractional occupations by assigning the finite temperature T in the above equation. This takes care of degenerate eigenstates (e.g, metals) in the vicinity of E_f, resulting in a smooth electron density distribution. It is worth mentioning that the finite temperature used here does not correspond to the physical temperature applied to the system rather it is an ingenious approach to deal with the partial occupancies in electronic structure modeling in DFT.

Gaussian Smearing: In this method, smearing exploits the Gaussian distribution function,

$$f(E) = e^{\frac{-(E-E_f)^2}{2\sigma^2}}, \tag{2.5.7}$$

Here, σ represents the smearing parameter, which controls the width of the Gaussian distribution. A careful selection of this parameter is required, as while larger σ values provide more numerical efficiency they suffer from inaccuracies. On the other hand, smaller σ values offer higher accuracy but may require longer computational costs. In the present work, we have made use of Gaussian smearing in combination of a small sigma value of 0.01.

2.5.4 Pseudopotential

In electronic structure calculation using the DFT framework, a pseudopotential is an approximation used to simplify the description of the electron-ion interaction in a solid-state system. Accurately representing the electron-ion interaction caused by the Coulomb potential due to the atomic nuclei requires a large number of plane-waves for the basis-set expansion. This makes the calculation highly challenging. Pseudopotentials are introduced to replace the core electron behavior and its screening effect accurately in a much simpler and computationally efficient representation by introducing a pseudo-effective potential designed to mimic the electron-ion interaction for valence electrons. Furthermore, different types of pseudopotentials are designed to capture various aspects of the electron-electron interaction and exchange-correlation effects. Here are some common types includes: LDA (Local Density Approximation), GGA (Generalized Gradient Approximation), Hybrid, Meta-GGA, etc. We employed GGA pseudopotentials with projector projector-augmented wave (PAW) framework. The PAW pseudopotentials are constructed to capture the interaction between valence electrons and atomic cores by matching the valence electron states of the pseudopotential system with the all-electron system.

2.5.5 van der Waals correction

Today, the most widely used theoretical approach to understanding the electronic structure of a crystal system is DFT. However, it's important to note that the employed exchange-correlation functionals especially the gradient correct ones such as GGA functionals, struggle to accurately describe dispersive interactions. Despite extensive research into this problem, the incorporation of dispersion effects into the standard KS-DFT remains a challenge. These long-range electron correlations become significant when there is minimum overlap between the electron densities of different parts of a system. To mitigate the overall issue of dispersion, usually, adding an empirical potential of the form C_6R^{-6} to the KS-total energy, where R represents the interatomic distances and $\{C_6\}$ are the dispersive coefficients, suffices for some of the dispersive systems. Our study involves the systems with heterostructures formed by interfacing the metal and 2D semiconductors. The fact that 2D semiconductors have inert basal planes indicate that the resulting interfaces are most often formed due to non-covalent interactions. Such interfaces need

to be calculated accounting for the long-range dispersion forces, which is often neglected in standard DFT calculations. To get more reliable results for van der Waals (vdW) systems, a dispersion correction term E_{disp} is added to the standard KS Energy (E^{KS}),

$$E^{KS-corr} = E^{KS} + E_{disp}, \tag{2.5.8}$$

where term $E^{KS-corr}$ denotes the vdW corrected energy of the system. In principle, electrostatic and exchange-repulsion interaction can be accurately accounted for, at mean-field theory level with HF and DFT level. The vdW correction (dispersion correction) improves the accuracy of the simulations by including the dispersion forces. Several methods have been devised for the vdW corrections including non-local density functionals (Grimme D2, D3, and D4 etc.) [61, 62, 63, 64], semi-empirical dispersion corrections, screened hybrid functionals among others.

The empirical dispersion correction is given by

$$E_{\text{disp}} = \sum_{i=1}^{N_{\text{at}}} \sum_{j=i+1}^{N_{\text{nat}}} \frac{C_{6,ij}}{R_{ij}^6} f_{damp}(R_{ij}) \tag{2.5.9}$$

where N_{at} is the number of atoms in the system, C_6^{ij} is the dispersion coefficient for atomic pair given by indices (i and j), s_6 represents a global scaling factor, and R_{ij} denotes the interatomic distance. The term f_{damp} is known as the damping function, which is incorporated to avoid singularities for R_{ij} approaching to zero. This is expressed in mathematical form as,

$$f_{damp}(R) = \frac{1}{1 + \exp\left(-\alpha(R/R_0 - 1)\right)}, \tag{2.5.10}$$

where R_0 denotes the sum of atomic vdW radii. This form of damping function has been proposed by Grimme in their DFT-D approach [61], as it decays at small R fast enough to zero so that dispersion correction vanishes below a typical van der Waals distance. However, later it was realized that for heavier atoms, the combination rule that was employed to get the C_6^{ij} coefficients as,

$$C_6^{ij} = 2\frac{C_6^i C_6^j}{C_6^i + C_6^j}, \tag{2.5.11}$$

gives too much weight to the smaller coefficients for lighter atoms. To remedy this DFT-D2 approach, Grimme [62] uses a geometric mean of the form

$$C_6^{ij} = \sqrt{C_6^i C_6^j}, \tag{2.5.12}$$

which provides a much better accuracy. This improvement owes itself to replace the nonlocal, long-, and medium-range electron correlation part in a correlation effects in the gradient corrected functionals by C_6 damping for R^{-6}-dependent terms. Although this new method yields better results when compared with standard GGA functionals, it comes at a cost of re-evaluation of the scale factor s_6 for common functionals as well as the self-interaction error has not been considered in the above framework.

To further improve upon the DFT-D2 model for non-covalent interaction, Grimme *et al.*

introduced DFT-D3 method [63], which yields higher accuracy, a broader range of applicability, and lesser empiricism. Moreover, the DFT-D3 method with "zero-damping" requires pair-specific cut-off radii and the presence of an artificial repulsive interatomic force at short distances leads to further inaccuracies. To mitigate these issues, they slightly updated the DFT-D3 approach accompanying Becke and Johnson (BJ) [65] proposed damping for $n \geq 6$ as given below in general form,

$$E_{\text{disp}} = -\frac{1}{2} \sum_{A \neq B} \frac{C_n^{AB}}{R_{AB}^n + const.}, \tag{2.5.13}$$

where R_{AB}^0 denotes the cut-off radius for atomic pair AB, and n denotes the nth-order dispersion coefficient. Using $n = 6, 8$, Grimme [64] has modified the DFT-D3 method to achieve the following expression,

$$E_{\text{disp}}^{D3(BJ)} = -\frac{1}{2} \sum_{A \neq B} s_6 \frac{C_6^{AB}}{R_{AB}^6 + [f(R_{AB}^0)]^6} + s_8 \frac{C_8^{AB}}{R_{AB}^8 + [f(R_{AB}^0)]^8}, \tag{2.5.14}$$

where $f(R_{AB}^0) = a_1 R_{AB}^0 + a_2$; the sum over all atomic pairs in the system ; a_1, a_2 are free fit parameters introduced by BJ. The pair-wise cut-off radius R_{AB}^0 is expressed as,

$$R_{AB}^0 = \sqrt{\frac{C_8^{AB}}{C_6^{AB}}}, \tag{2.5.15}$$

In the present work, the choice of vdW correction schemes was based on the earlier reports which includes the DFT-D3 method of Becke-Johnson damping function along with a benchmark study carried out invloving other functionals.

2.6 Crystal Interface Construction

Modeling the interfaces between a semiconductor and a metal in DFT calculations comprises several essential stages. Modeling the heterostructure interface is pivotal for gaining insights into the electronic and chemical characteristics of these connections. When constructing the interface, there are various crucial factors to consider, including the number of metal layers, crystal facet orientation, minimum lattice mismatch, initial distance at the interface, and more.

2.6.1 The Number of Metal Layers

To accurately represent realistic semiconductor/metal contacts, it is essential to interface the 2D semiconductor with bulk metal. However, we must confine ourselves to a practical number of metal layers, typically ranging from three to six layers, to effectively replicate the bulk metal properties. We conducted a benchmark study using five layers of metal and observed that it closely matches the experimental work function.

2.6.2 Metallic Surface Orientation

Choosing the appropriate metallic surfaces can be a complex task, with several critical considerations. In general, the selection aims to ensure that the surfaces are free from defects in

experiments and possess a stable interface with the metal contact. Typically, crystal planes with higher coordination numbers and greater atomic density are more stable than other low-index planes.

In this study, the metallic electrodes encompass FCC crystal structures (Ag, Au, Cu, Pd, and Pt), where the (111) plane is the most densely packed; BCC crystal structures (Mo, Cr, V, and W), where the (110) plane is the most stable; and HCP crystals (Co, Sc, Ti, and Zn), featuring the (0001) plane with the highest coordination numbers and stability. Consequently, we have given priority to selecting these planes for our investigation. However, it is worth noting that constructing an interface structure with these atomic planes may necessitate an exceedingly large supercell, which can be impractical even for DFT calculations. In such cases, we may opt to use less densely packed atomic planes.

2.6.3 Lattice Strain

While modeling the commensurate semiconductor/metal interface, considering lattice mismatch is crucial as it can significantly influence the interface's properties and behavior of the system. Lattice mismatch refers to the disparity in atomic spacing or arrangement between the crystal lattices of the metal and semiconductor. Moreover, the presence of lattice mismatch between the metal and semiconductor can induce strain within the interface region. This strain can give rise to the formation of dislocations, defects, or misfit dislocations, where the crystal structure distorts to accommodate the mismatch. Therefore, to replicate realistic semiconductor/metal conditions, we took great care to realize the realistic condition as much as possible by ensuring the lattice strain below 5% average error along either periodic direction. This is accomplished by expanding the metal and semiconductor crystals along the periodic direction (x, y) into a commensurate supercell. To quantify the lattice strain, usually mean absolute strain (MAS) has been calculated as,

$$\text{MAS} = \frac{1}{N}\sum_{i=x,y}|\epsilon_i| \tag{2.6.1}$$

where $N = 2$ represents the number of lattice directions, where the combined supercell has been matched. ϵ_x, and ϵ_y denote the lattice strain along x, and y-lattice directions, respectively, expressed as $\epsilon_x = \frac{\Delta L_x}{L_{y0}}$, and $\epsilon_y = \frac{\Delta L_y}{L_{x0}}$, where L_{x0} and L_{y0} are the original lattice parameters in the x and y-directions, respectively. A representative example is presented in Fig. 2.3.

2.6.4 Interface Distance and Vacuum Buffer

The interface distance between the metal and semiconductor within the combined crystal lattice was initially determined based on the atomic radii of the atoms facing each other at the interface in our initial modeling. This adjustment was made to enhance the efficiency of the self-consistent field (SCF) cycle and achieve the ground state configuration more rapidly. It is important to note that, during subsequent crystalline relaxation, the interface separation was ultimately modified to reach an equilibrium separation. Additionally, our modeling approach incorporates a vacuum buffer along the interface direction. This buffer serves to mitigate the spurious interactions resulting from periodic boundary conditions in DFT calculations. Furthermore, to maintain the crystal's structural integrity and prevent surface reconstruction, the bottom two layers of metals are fixed..

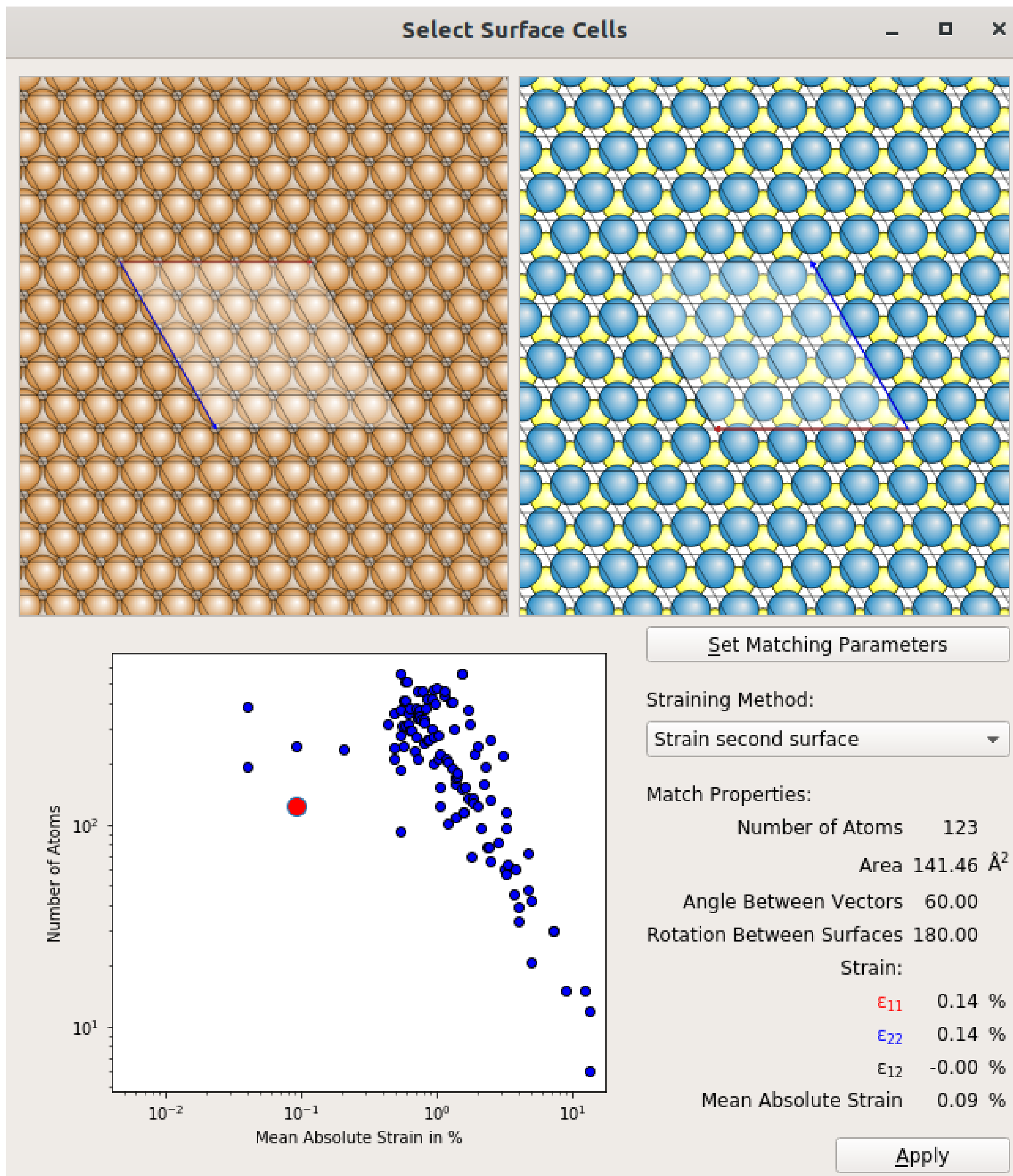

Figure 2.3: The illustration of the construction of semiconductor/metal interface. The percentage mean absolute lattice strain is given for different sets of interface matching. In the present case, the red circle indicates the interface constructed consisting of 123 atoms in total, with mean absolute strain = 0.09%. Interface construction is done using the QuantumATK [66] GUI.

2.7 Mechanical Property

The mechanical properties of a semiconductor/metal interface are important for understanding the stability and reliability of electronic devices that utilize this interface. These properties can impact the mechanical integrity and performance of such devices. These mechanical properties are influenced by various factors, including the choice of materials, the crystallographic orientation of the materials, surface treatments, and device operating conditions. Fig. 2.4 demonstrates contact resistance arising in the device schematic. In our work, two highly crucial factors have been discussed including 1) adhesion strength and 2) Interface stress. The former has been described in the following section, whereas the latter has already been discussed in the earlier section 2.6.3.

2.7.1 Interface Stability

Interface stability is a fundamental consideration in the design, fabrication, and operation of electronic and opto-electronic devices based on 2D semiconductor-metal interfaces. Ensuring stability enhances device performance, reliability, and longevity while enabling the development of advanced technologies. Stable interfaces are less prone to degradation over time ensuring properties essential for device reliability. An unstable interface may promote undesired defect formation and trap charge carriers leading to high contact resistance, hindering efficient charge carrier injection. Stable interfaces, however, ensure efficient charge transport and minimize energy consumption, which leads to better device efficiency. In 2D semiconductors, due to passive basal planes, the contact interfaces do not have as high affinity as 3D semiconductors to adhere to the metal surface due to the unavailability of unsaturated dangling bonds in 2D semiconductors. To quantify the relative interface stability of different contact systems, we carried out the binding strength of the interface using the following expression,

$$E_b = \frac{1}{A}\left(E_m + E_s - E_{sys}\right), \tag{2.7.1}$$

where E_m, E_s, and E_{sys} represent the metal energy, semiconductor energy, and the total the energy of the combined system, respectively. The parameter A denotes the area of the interface, which is employed to normalize the E_b values to enable the relative binding strength comparison among different contact interfaces.

2.7.2 Interface Separation and Tunnel Barrier

The binding strength of the contact interface manifests itself in the form of interface separation as presented in Fig. 2.5 by a vertical dashed line separating metal and semiconductor portions. To characterize the overall contact resistance of the contact systems, there are interfaces to be considered: 1) Vertical interface that denotes the direct semiconductor/metal contact, 2) Lateral contact denoting the metal-contacted-channel interface as shown in the schematic diagram in Fig. 2.4. An improved device performance generally takes shape with appropriate engineering of these two interfaces. The vertical interface plays a major role in the device's performance. The separation between the semiconductor and metal at this interface determines the properties of the interface including stability and the emerging tunneling barrier. The tunneling barrier refers to an energy barrier that charge carriers (e.g., electrons, holes) must overcome to move from one side of the interface to the other through quantum tunneling. The tunneling bar-

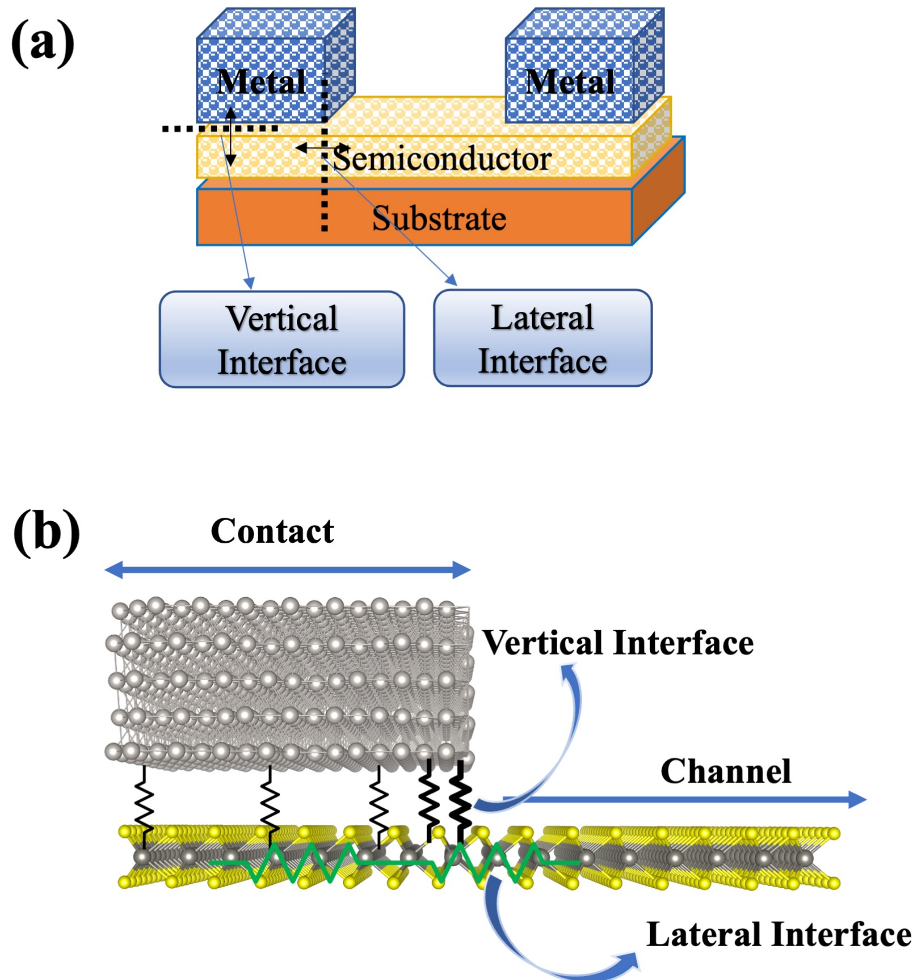

Figure 2.4: (a) A schematic diagram of a typical FET. Contact resistance depends on two interfaces: 1) Vertical interface (direct semiconductor/metal contact), 2) Lateral interface (coupling between contact part and semiconductor in the channel). In figure (b) both the interfaces have been depicted as the atomic contacts.

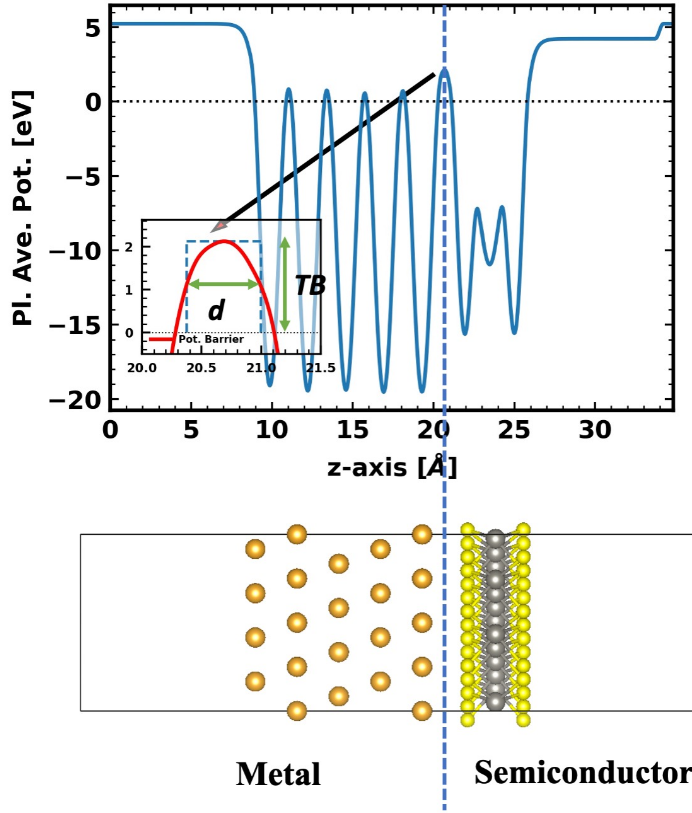

Figure 2.5: Illustration of tunneling barrier emerging as a consequence of finite interface separation at the interface.

rier height can be tailored by adjusting the interface separation. A larger separation increases the tunneling barrier height, while a smaller separation reduces it. In general, the separation between pristine 2D-semiconductor/metal interfaces lies between 1.5 to 3.5 Å, where the quantum mechanical tunneling effect becomes significant. We have modeled the quantum mechanical tunneling by studying the electrostatic potential of the system and approximating the barrier into a rectangular barrier as shown in Fig. 2.5. The full-width half maxima (FWHM) has been taken as the width of the barrier (d) while the height of the barrier is used as the tunneling energy barrier (T_b). T_b represents the barrier height with respect to the Fermi level. We employed the following expression to calculate the tunneling probability of all the barriers.

$$T \sim \exp\left(-2\sqrt{\frac{2mT_b}{\hbar^2}}d\right), \tag{2.7.2}$$

It is worth noting that some of the metals show very intimate contact with the semiconductors with zero tunneling barriers. In such cases, we have $T = 1$, employing a transparent interface for the carriers to flow.

2.8 Electrical Properties

The electrical properties of a semiconductor/metal interface play a crucial role in various electronic devices and circuits. These properties are determined by the behavior of charge carriers (usually electrons and holes) as they interact with the interface between the metal and semiconductor materials. Parasitic contact resistance is the primary issue with the 2D-semiconductor/metal interface. The contact resistance appears to result from both the tunnel barrier and the Schottky barriers which charge carriers must overcome to move between the metal and semiconductor. Lower contact resistance is desirable for efficient charge carrier injection or extraction in electronic devices. A large number of researchers modified and engineered the material interface to achieve specific device characteristics and performance goals. Most of these prospects depend on being able to successfully achieve lower contact resistance, which is essential for the efficient operation of electronic and optoelectronic devices. Several challenges can impede the realization of low-contact resistance, albeit depending on the specific materials, device structure, and operating conditions. Some of the common challenges associated with achieving Ohmic contact or contact with lower resistance in metal-semiconductor (MS) interface:

Fermi Level Pinning: Fermi level pinning occurs when the energy levels at the MS interface becomes pinned, generally assumed but not limited due to surface states or defects. This pinning can lead to a misalignment of energy bands, creating energy barriers that increase contact resistance. Metallic work function-based models such as Schottky-Mott [67, 68] (SM) model drastically fails to account for the barrier heights.

Metal Work function Matching: According to the SM model a good choice of metal can help achieve low contact resistance by selecting a good match between the work function of the metal and electron affinity (χ_S) of the semiconductor.

Schottky Barrier Height: The Schottky barrier height (SBH) represents the energy barrier that charge carriers must surmount when moving across the MS junction. Achieving a low SBH is crucial for reducing contact resistance. However, the choice of metal and semiconductor can limit the ability to lower this barrier.

Surface and Interface Defects: Surface states, and states arising from the defects at the MS interface can act as charge trap states. These trap states often lead to scattering of conducting charge carriers thereby contributing hugely to increased contact resistance. Generally, passivating or reducing these defects is essential for achieving low contact resistance.

Contact Annealing and Post-Processing: In the experimental fabrication of the MS interface, thermal annealing, and subsequent post-processing steps can influence the quality of the interface. Optimizing the annealing conditions based on the specific requirements of selected metals and semiconductors can reduce contact resistance.

Interface Engineering: Advanced interface engineering techniques are often employed to reduce the overall contact resistance. Moreover, these engineered interfaces often come at a cost of a very expensive and highly optimized experimental setup, which is not understood yet enough to be used for large-scale synthesis for any type of MS interface.

The MS interface is often accompanied by electric contact having non-Ohmic behavior. As shown in Fig. 2.6, at the metal side we have a sea of electrons responsible for electrical conduction; on the other hand, at the semiconductor side, there is a misalignment of Fermi level until they are kept in contact with each other. Upon interface formation electrons in the semiconductor's conduction band minima (CBM), flow towards the metallic side until the Fermi level on both sides aligns leading to band bending. This band bending creates the Schottky contact by introducing the Schottky barrier height (SBH) across the interface, which is the most crucial

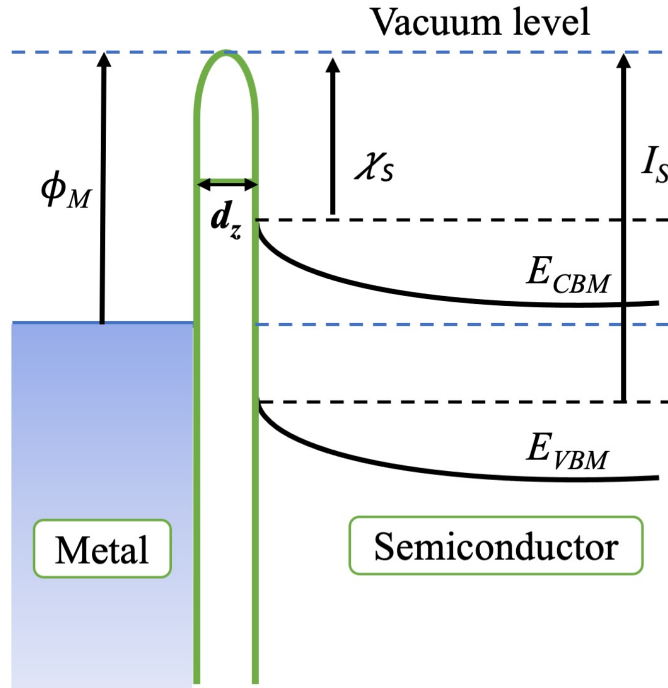

Figure 2.6: Energy levels and band bending upon metal-semiconductor contact. Vacuum-level has been assumed to be at zero reference point.

aspect of an interface formed by MS contact that regulates its electrical properties. Depending on the energy alignments of the semiconductor and metal at the interface, it could be either n-type or p-type contacts. For n-type semiconductors, the primary contributors to electrical conduction are the electrons located near the CBM. Conversely, in p-type semiconductors, the predominant carriers of current are the holes found near the valence band maximum (VBM). In other words, the lowest available energy state (representing CBM) in the n-type semiconductors interacting with electrons in the metal, are located above the Fermi level of the combined MS interface. And the energy difference between the CBM and the Fermi level representing n-type SBH, results in an energy barrier for the electron transport across the MS interface. On the other hand, the highest occupied energy level accessible to holes (representing VBM) lying below the Fermi level yields p-type SBH from the energy difference between VBM and the Fermi level. Consequently, these SBHs create a barrier that, depending on where the Fermi level is located inside the semiconductor's fundamental band gap, causes n-/p-type rectifying behavior at the interface between the metal and the semiconductor. The contact polarity of an MS interface plays a crucial role in determining the contact resistance for electron or hole conduction; for example, the polarity of an n-type and p-type contact makes electron injection and hole injection easier, respectively.

2.8.1 Schottky Barrier Height

As discussed above, contact resistance can be quantified with the help of SBH evaluation of the MS interface. The Schottky-Mott model is generally employed technique to calculate the SBH (see a recent review [69] for more detail). The Schottky-Mott model is a fundamental concept that attempts to calculate the SBH by addressing the alignment of energy bands in both isolated crystals and their intimate MS interface. It emphasizes the role of electrostatics in understanding energy-level alignment. In an isolated system, energy bands are first referenced to the vacuum level outsite, whereby the work function (ϕ_M) of an isolated metal is determined from the energy difference between its vacuum level and Fermi level. Similarly the position of CBM and VMB with respect to the vacuum level of an isolated semiconductor gives it's electron affinity (χ_{SC}) and ionization potential (I_{SC}), respectively (see Fig. 2.6). The Schottky-Mott model states that the energy band alignment observed in isolated systems should also apply to the MS interface providing expressions for calculating the SBH for electrons (n-type) and the SBH for holes (p-type). Usually, the n-type and the p-type SBHs are denoted by $\Phi_{B,n}$ and $\Phi_{B,p}$, respectively, which are expressed as,

$$\Phi_{B,n} = \phi_M - \chi_{\mathrm{SC}} \tag{2.8.1}$$

and,

$$\Phi_{B,p} = I_{\mathrm{SC}} - \phi_M, \tag{2.8.2}$$

where χ_{SC} and I_{SC} represent the electron affinity and ionization energy of the semiconductor.

From the above discussion, if the CBM of the semiconductor remains positioned with respect to the Fermi level as it was before contact, then the rule is properly followed. The fundamental concept behind the SM model, similar to the associated Anderson model [70] for determining heterojunction band offsets, is rooted in the principle of electrostatic potential superposition. In practical terms, these theories can be thought of as the straightforward process of aligning the vacuum energy levels at the exteriors of two surfaces. However, it is important to note that the strict application of the SM model to real MS interfaces is limited, as it does not account for the charge rearrangement during the interface formation resulting from the interaction at the interface. Rather, it serves as an indicator of the system's electrostatics before interface chemistry becomes dominant.

In the present work, the electrostatic potential has been utilized to determine the position of the vacuum level. It is important to note that the term "vacuum level" referred here corresponds to an electron's energy positioned immediately outside the surface of a crystal. This equivalence with the vacuum level at infinity is only valid in situations where the long-range electric field completely disappears in the vacuum [71]. Although 2D semiconductors have passive surfaces free of dangling bonds, a realistic 2D-MS interface is accompanied by finite charge transfer at their interfaces, which is beyond the SM model and is an idealistic, non-interacting picture of the MS interface. Therefore, we cannot simply apply the SM model to the realistic 2D-MS interface. The electronic states associated with the surfaces of both crystals may not persist in the same form after the MS interface is formed; they are likely to undergo significant modifications. Newly formed "interface states" localized within the interface region and influenced by the atomic structure of the interface can emerge due to interactions between metal and semiconductor atoms. The actual distribution of charge at an MS contact will deviate substantially from

a straightforward sum of the charges on the surfaces of metal and semiconductor when kept in isolation. This leads to an overall change in potential energy caused by charge redistribution at the interface. This change can be attributed to the creation of an additional, recasting the original SM models as follows,

$$\Phi_{B,n} = \phi_M - \chi_{\mathrm{SC}} + \Delta V, \tag{2.8.3}$$

$$\Phi_{B,p} = I_{\mathrm{SC}} - \phi_M - \Delta V, \tag{2.8.4}$$

where the term ΔV denotes the energy associated with the interface dipole energy which can be captured by calculating the electrostatic potential of the MS interface. The interface dipole is essentially the outcome of charge transfer between the metal and the semiconductor.

2.8.2 Fermi Level Pinning

The selection of metal to create a good quality (with zero or vanishing SBH) contact interface with a semiconductor often depends on the work function of the metal as the work function gives the position of its Fermi level with respect to the vacuum level. For instance, to achieve zero n-type SBH for a semiconductor having an ionization potential of 5.0 eV, a metal with the same work function is supposed to provide zero n-type SBH within the idealistic SM framework. However, in practice, due to a finite charge re-arrangement taking place at the MS interface, the semiconductor's Fermi level is pinned or fixed at a specific position within the band gap, regardless of the metal used for the contact. Instead of the idealized alignment predicted by the SM model, the Fermi level of the semiconductor remains pinned to its original position, leading to deviations in the SBH and the actual SBH observed in experiments.

In experimental setups, to quantify the pinning effect, Fermi-level pinning parameter denoted as S is used,

$$S = \frac{\partial \Phi^0_{B,n}}{\partial \phi_M}, \tag{2.8.5}$$

which is nothing but the slope of the linearly fitted value of SBH with respect to the work function of the metals. This parameter is associated with every semiconductor, giving the information about the severity of its pinning effect. A value of S = 1 corresponds to the idealistic Schottky-Mott model, which is rarely observed in experiments due to several reasons unavoidable factors including unintentional modification at the interface during the fabrication processes. Furthermore, a value of S=0 indicates a strongly-pinned case with no dependence on metal's work function. This situation is also referred to Bardeen limit. John Bardeen [72] realized that the existence of states at the interface, with energies within the semiconductor's band gap could facilitate the absorption of a significant amount of charge transferred from the metal. The absorption effectively shields the semiconductor from the specific characteristic of metal, resulting in the alignment of the semiconductor's energy bands naturally aligning themselves in relation to the surface states, which are, in turn, pinned to the Fermi level due to their comparatively higher density of states. To provide a perspective on the fact that how severe is the FLP, in practice, based on the experimental data, the observed S-parameter for Si is ~ 0.2 [69]. For 2D-semiconductor-metal contact, an example for WS_2-metal is presented in Fig. 2.7, showing the FLP towards CBM.

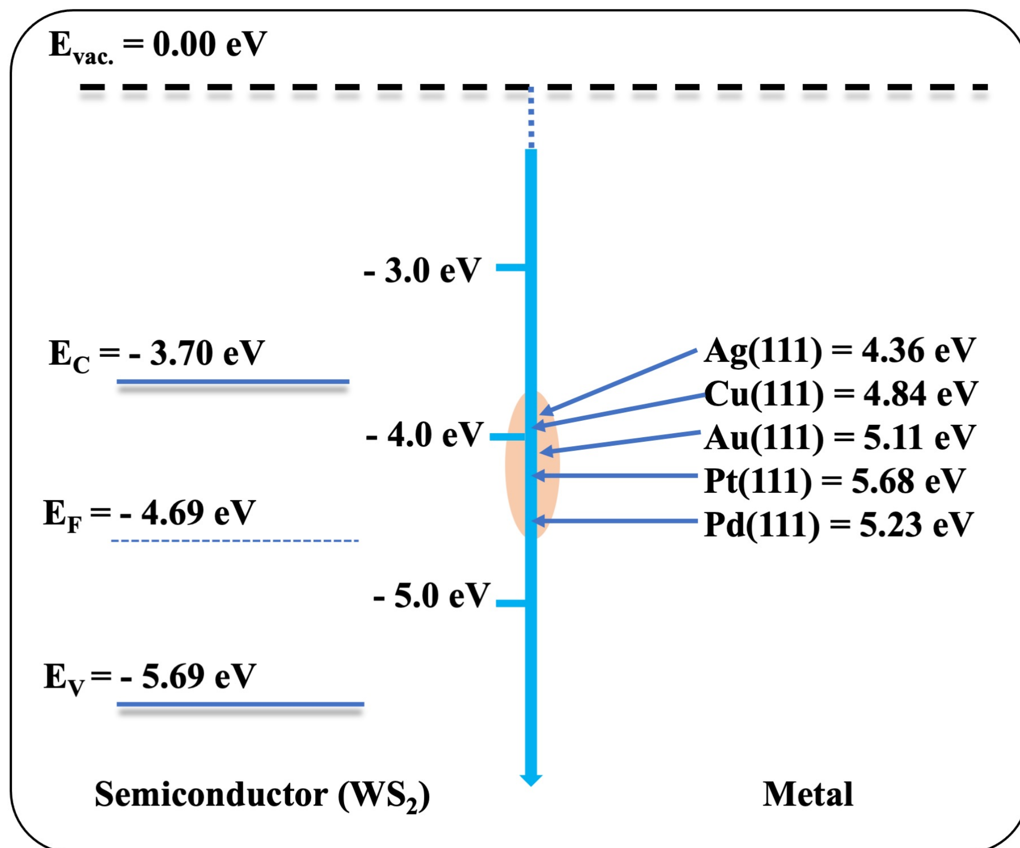

Figure 2.7: Illustration of FLP for WS_2-metal contact. It represents the FLP occurring towards CBM. High work function metals expected to yield p-type SBH such as Pd and Pt, contrarily lead to pinning towards CBM. This clearly shows that p-type conductivity is difficult to achieve with WS_2.

2.8.3 Metal-induced Gap States (MIGS)

One of the major reasons why the idealistic Schottky-Mott model fails to accurately describe the SBH arising at the realistic MS interfaces is the emergence of metal-induced gap states (MIGS) in the band gap of the semiconductor. These states play a crucial role in characterizing the Fermi-level pinning effects. Upon interface formation, due to electronic interaction between the metal and semiconductor, the metal's electronic states (Bloch states due to breaking of lattice symmetry at the interface along a non-periodic direction) can penetrate into the band gap of the semiconductor, creating new electronic states within the band gap also known as MIGS. The MIGS are typically located within the semiconductor's band gap near the CBM or VBM, depending on the specific interface or material. In this scenario, conduction electrons, instead of living into the semiconductor's CBM find it energetically favorable to reside in the MIGS. As a result, the alignment of the metal's Fermi level takes place with these MIGS instead of the true Fermi level of the semiconductor, rendering the use of the SM model without appropriate modification for SBH prediction disputable. Moreover, in electronic structure calculation using DFT we can gain insights into the MIGS by calculating the band structure projection resulting from the modification in the semiconductor's band edges in the total band structure. This process, which is often referred to as fat band technique, also yields the accurate SBH, for the vertical interface as shown int Fig. 2.4 without employing the SM model. It is worth mentioning that several semiconductors including phosphorene have been found to be metalized on the metallic surfaces, providing Ohmic contact, which can not be assessed for its SBH based on either model (SM model, fat band technique). However, the SBH emerging at the lateral interface can be computed with the help of the modified equations presented in Eqs. (2.8.3) and (2.8.4).

Chapter 3

Phosphorene-Metal Contact

3.1 Background

Phosphorene, a noteworthy two-dimensional material (2DM), first gained prominence in the early part of 2014 [73, 74, 75]. This unique material exhibits a layer-dependent band gap ranging from 0.3 eV to 2.0 eV [76, 77, 78, 79]. This feature places phosphorene in an ideal position for a wide array of field-effect transistor (FET) applications. Moreover, phosphorene's anisotropic transport properties and its impressive carrier mobility, approximately 1000 cm^2/Vs, make it as a highly promising contender for the next-generation field-effect transistors (FETs) [73, 80, 81, 82, 83].

Numerous first-principles-based theoretical investigations have explored metal-phosphorene interfaces, albeit with a limited selection of metals. Additionally, understanding the intricate relationship between interface properties and various metals can be challenging due to the complexities of different metal-semiconductor interfaces. For instance, recent studies by Pan *et al.* [17] and Maity et al. [18] observed that Ti-phosphorene forms a pure Schottky contact, while Chanana *et al.* [19] suggested an intermediate contact. Meanwhile, Gong *et al.* [84] reported that Cu forms an excellent ohmic contact, demonstrating as the preferred choice for metal electrodes with phosphorene. On the other hand, Cu creates both a tunnel barrier and a finite Schottky barrier at the metal-phosphorene contact, according to researchby Pan *et al.* These discrepancies could result from variations in simulation conditions, such as the choice of exchange-correlation functionals, pseudo-potentials, and metallic surfaces being utilized. To establish a comprehensive and reasonable basis for comparing different metal-phosphorene contacts, it is imperative to employ a uniform methodology and a consistent set of input parameters. This approach ensures a reasonable selection of metals forming mechanically stable contacts along with favorable electrical properties. Notably, previous studies lacked a holistic understanding of the interplay between the mechanical strength of contacts and their influence on the electrical characteristics.

This work presents a detailed *ab initio* investigation of metal and mono-layer phosphorene interfaces, offering a systematic analysis of their mechanical and electrical properties. Eighteen metals were investigated for their properties upon their contacts to mono-layer phosphorene: aluminum (Al), silver (Ag), gold (Au), cobalt (Co), copper (Cu), chromium (Cu), molybdenum (Mo), nickel (Ni), niobium (Nb), platinum (Pt), palladium (Pd), ruthenium (Ru), scandium (Sc), tantalum (Ta), titanium (Ti), tungsten (W), zinc (Zn), and vanadium (V). The investigation goes into various metal-phosphorene interfaces, scrutinizing the factors that influence their mechanical and electrical properties. Adhesion strength, represented by the work of separation (W_{sep}), is

calculated to assess the mechanical stability of the metal contacts when interfaced with monolayer phosphorene. In order to assess electrical performance, the study also takes into account a number of other important properties, such as the density of states, the height of the tunnel and Schottky barriers, and the charge density estimates at the mid-interface. By examining the interface chemistry, this study establishes a crucial link between the mechanical and electrical properties of metal-phosphorene contacts, enabling a fair comparison among different metal contacts.

3.2 Computational Methodology

The Vienna Ab Initio Simulation Package (VASP) [85, 86] served as the primary tool for conducting our DFT calculations. We employed the Perdew-Burke-Ernzerhof (PBE) method of the generalized gradient approximation (GGA) exchange-correlation functional [87] in these calculations. To ensure a smooth core-valence electron density connectivity, we utilized the projector-augmented wave (PAW) corrected pseudopotential [88] using a plane wave basis set with a cutoff energy of 400 eV for both crystal structure optimization and subsequent electronic structure computations. For metals exhibiting magnetic properties, such as Co and Ni, we performed spin-polarized calculations in ferromagnetic configurations. We set per atom force and energy thresholds at less than 0.01 eV/Å and 1×10^{-5} eV, respectively, during structural optimization. To obtain a more accurate total energy, we used the Methfessel-Paxton [89] smearing scheme with a sigma value of 0.01 to account for the partial occupancy in metallic systems, for energy calculations; however, we used tetrahedron smearing with Blochl-correction [90] for electronic structure calculations, which included the Fermi energy, density of states (DOS), and vacuum level. This approach provides an accurate representation of the electronic density of states. Furthermore, we incorporated the optB86b-vdW [91] dispersion correction, which is instrumental in computing both geometric and electrical properties, especially for non-covalent interactions. To further validate our observed trend, we, in addition, employed DFT-D3 [63] dispersion correction. To prevent interactions of repeated cell slabs, in a periodic boundary condition (PBC)-based DFT framework, we included a vacuum space region of no less than 12 Å along the z-axis, perpendicular to the metal-phsphorene interface. It's essential to note that for specific metals, a vacuum level exceeding 12 Å was necessary to ensure the convergence of the vacuum potential. The lattice, along the periodic direction (along the x and y-axes) has been kept unchanged, as depicted in Fig. 3.1. Given the diverse and rather large set of metal species with varying lattice parameters employed in this study, we took great care to ensure that the phosphorene supercell aligned with a commensurate supercell of the metal, by minimizing the lattice strain in the metals.

3.3 Results and Discussion

Standard DFT simulations are not directly suitable for the calculation of contact resistance in metal-phosphorene interfaces. Nevertheless, critical factors contributing to contact resistance can, in principle, be deduced from electronic structure calculations utilizing the standard DFT method. Some of the pivotal factors leading to contact resistance include, but are not confined to, chemical interactions, band bending leading to the formation of Schottky barriers, variations in the work function between the metal and semiconductor, the presence of surface states, interface strain, and charge rearrangement. A comprehensive exploration of metal-semiconductor

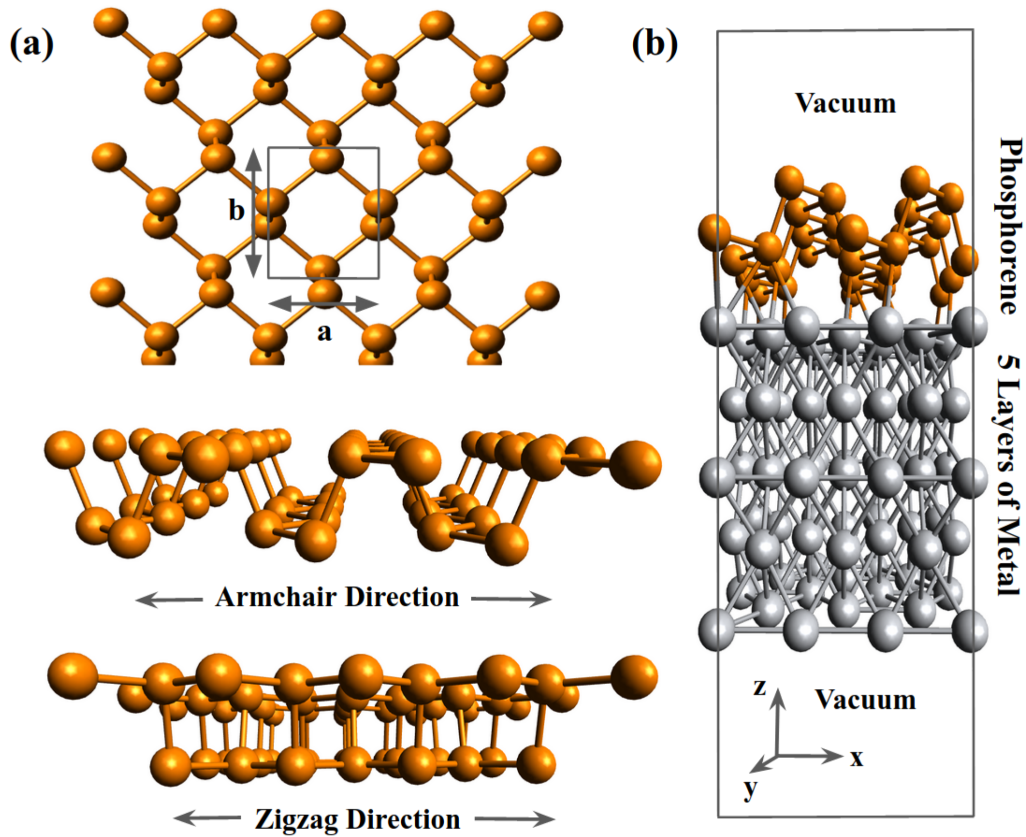

Figure 3.1: (a) Crystal structure of monolayer phosphorene as viewed from three different directions: top view showing the unit cell with lattice parameters a = 3.30 Å and b = 4.63 Å, side view depicts the armchair and zigzag dirctions. (b) Side view of the metal-phosphorene system with the specified coordinates. A vacuum buffer is introduced along the $\pm z$ direction. The combined metal-semiconductor systems contain 5 layers of metal interfaced to monolayer phosphorene. (Reproduced from Ghaffar *et al.* [92] under CC BY-NC-ND license.)

(MS) interfaces, involving the quantitative assessment of these properties, facilitates a meaningful comparison of contact resistance across various MS interfaces. A few of these qualities are covered in the sections that follow.

3.3.1 Mechanical Properties of the Interface

The mechanical strength or binding strength of the metal-phosphorene interface is evaluated through the determination of the work of separation (W_{sep}), which is also expressed in terms of binding energy (E_b). This parameter characterizes the anti-peeling energy or adhesion strength of the interface and is calculated using the formula presented in Eq. (2.7.1). The resulting W_{sep} values for all the metals are provided in Table 3.1, with higher values signifying stronger adhesive strength. Notably, among the metals, V exhibits the highest adhesive strength, while Zn displays the lowest, aligning with the findings from [84]. Furthermore, to categorize the metals into two different categories, a threshold value of 1.5 J/m^2 for W_{sep} is selected. Metals with W_{sep} < 1.5 J/m^2 are classified as type 1, indicating low adhesion, while those with W_{sep} > 1.5 J/m^2 are categorized as type 2, indicating high adhesion. An intriguing observation is made with this threshold; it doesn't merely divide the range of calculated W_{sep} values arbitrarily. It reveals that all type 1 metals possess filled d-orbitals, whereas type 2 metals, except for Pd, have vacant d-orbitals. This suggests that vacant d-orbitals in metals facilitate the hybridization of s- and p-orbitals of phosphorene atoms, contributing to stronger adhesion. The presence of vacant d-orbitals in metals enables stronger bonding with phosphorene, establishing it as a pivotal criterion in the selection of metals for enhanced mechanical strength. Pd, although lacking vacant d-orbital states, demonstrates high adhesive strength due to the almost equal energies of its 4d- and 5s-orbitals, enabling electrons to transition from the 4d to the 5s-orbitals, thus creating vacant orbitals for hybridization and bonding at the interface.

For a more in-depth analysis, we've calculated the average interfacial equilibrium distance (d_z) between the layers of metal and the phosphorene exposed at the interface, as detailed in Table 3.1. It's noteworthy that type 2 metals exhibit notably lower d_z values when compared to type 1 metal. This observation points to stronger chemical interactions and potential for hybridization with the phosphorene surface layers in the case of type 2 metals. Conversely, type 1 metals display significantly higher d_z values, indicative of weaker or even non-covalent interaction. The relationship between W_{sep} and d_z is visually represented in Fig. 3.3a. This illustration underscores the connection between adhesion and bond strength, highlighting that a decrease in d_z corresponds to an increase in W_{sep}. This correlation emphasizes the pivotal role of bond strength in determining adhesion. Furthermore, we conducted W_{sep} calculations using the DFT+D3 [63] functional. Fig. 3.3b provides a comparison of the results obtained with the optB86b-vdW and PBE+D3 functionals. Clearly, both methods independently suggest that Ta forms a superior adhesive contact when compared to Nb (W_{sep} of Ta > W_{sep} of Nb). However, an interesting discrepancy arises when we perform W_{sep} calculations with DFT+D3 for Nb and optB86b-vdW for Ta, leading to the opposite conclusion. This disparity again highlights the critical importance of conducting analyses employing a standardized set of simulation criteria, which includes energy thresholds, smearing methods, lattice matching, and barrier calculation techniques, as already laid out in this study.

Table 3.1: A list of lattice characteristics utilized to construct phosphorene supercell (SC) and the metal SC to realize the commensurate metal-semiconductor contact interfaces, are presented. In addition to relevant parameters regarding interface modeling, a comprehensive summary of calculated properties are also compiled in this table. (Reproduced from Ghaffar *et al.* [92] under CC BY-NC-ND license.)

Type	S.No.	Metal	Metal SC	BP SC	$\Delta x\%$	$\Delta y\%$	W_{sep} (J/m2)	d_z (Å)	$\Phi_{B,n}$ (eV)	$\Phi_{B,p}$ (eV)	TBH (eV)	ρ (e)
Type 1 Metals	1.	Zn(0001)	5 × 1	4 × 1	0.75	0.50	0.60	2.75	0.09	0.83	1.74	0.098
	2.	Ag(111)	5 × 2	3 × 3	4.10	1.21	0.88	2.54	0.50	0.42	1.59	0.126
	3.	Al(110)	4 × 3	5 × 2	1.82	7.23	0.92	2.45	0.29	0.63	0.97	0.105
	4.	Au(110)	4 × 3	5 × 2	1.09	6.53	0.93	2.41	1.02	0.00	1.88	0.154
	5.	Cu(111)	4 × 1	3 × 1	3.13	4.54	1.27	2.34	0.73	0.19	0.83	0.168
Type 2 Metals	6.	Mo(110)	1 × 1	1 × 1	4.54	1.79	1.82	2.25	0.75	0.17	0.00	0.285
	7.	Pd(111)	5 × 1	4 × 1	4.17	2.81	1.86	2.13	1.16	0.00	0.00	0.266
	8.	W(110)	1 × 1	1 × 1	4.24	3.46	1.91	2.11	1.02	0.00	0.00	0.292
	9.	Co(0001)	4 × 1	3 × 1	1.41	6.05	2.29	1.97	0.87	0.05	0.00	0.276
	10.	Ni(111)	4 × 1	3 × 1	0.56	6.89	2.32	1.97	0.92	0.00	0.00	0.296
	11.	Pt(111)	5 × 1	4 × 1	5.00	3.67	2.45	2.12	1.36	0.00	0.00	0.283
	12.	Nb(110)	1 × 1	1 × 1	0.00	0.80	2.55	1.99	0.87	0.05	0.00	0.304
	13.	Sc(0001)	1 × 3	1 × 4	0.30	7.13	2.61	2.22	0.33	0.59	0.00	0.144
	14.	Ru(0001)	5 × 1	4 × 1	2.27	1.00	2.63	2.15	1.00	0.00	0.00	0.273
	15.	Ta(110)	1 × 1	1 × 1	0.30	1.08	2.68	1.94	1.14	0.00	0.00	0.288
	16.	Ti(0001)	3 × 2	2 × 3	4.43	3.23	2.97	2.00	0.39	0.53	0.00	0.223
	17.	Cr(110)	3 × 4	2 × 5	1.27	6.69	3.16	1.90	0.70	0.22	0.00	0.316
	18.	V(110)	3 × 3	2 × 4	2.16	2.95	3.25	1.93	0.72	0.20	0.00	0.302

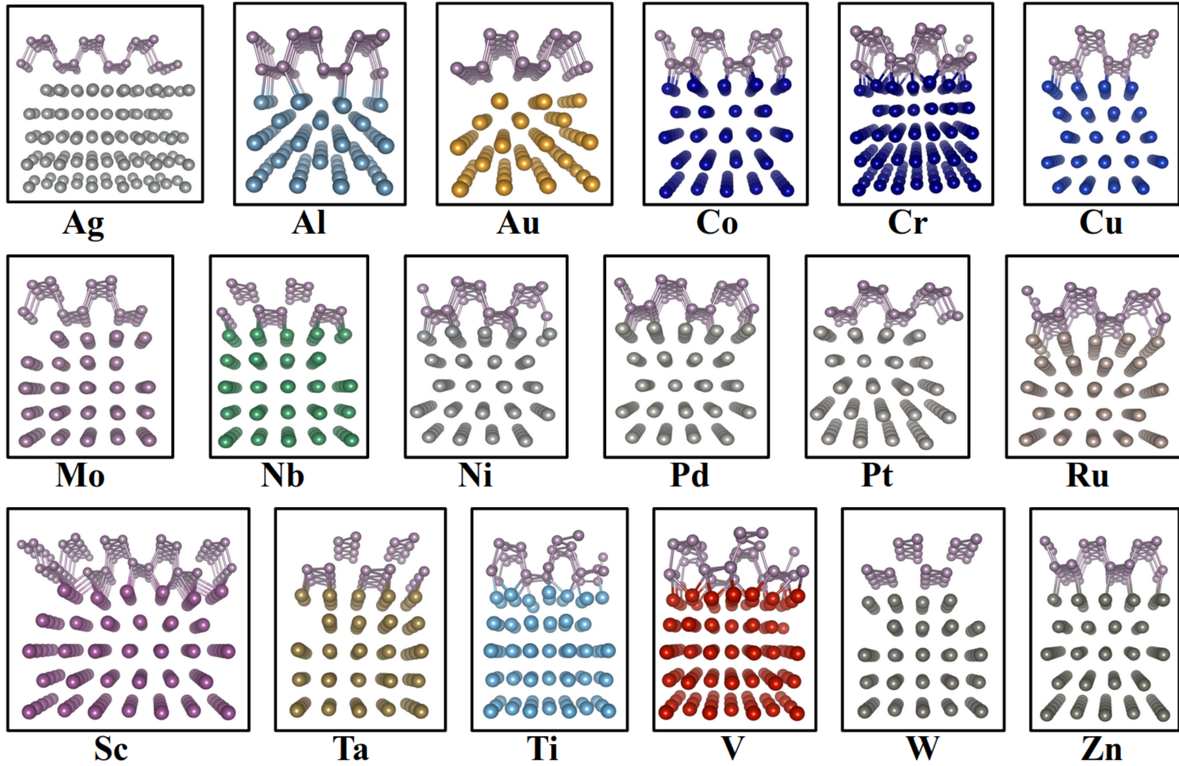

Figure 3.2: Optimized structures for all the eighteen metal-semiconductor contacts. These structures represent the distinct effect of metals on the phosphorene surface. The apparent distortion in some of the cases is linked with the higher interface reactivity. (Reproduced from Ghaffar *et al.* [92] under CC BY-NC-ND license.)

3.4 Electrical Properties

The most crucial aspect of an effective metal contact is the facilitation of charge flow between 2DM and the metal contact. Nevertheless, this capability is contingent on various factors. Here, we explore the various electrical characteristics of the metal-phosphorene interface in order to determine the critical factors controlling charge transport through the interface and, in turn, contact resistance.

3.4.1 Partial Density of States (PDOS)

We conduct Partial Density of States (PDOS) calculations to assess variations in the phosphorene DOS caused by the presence of metal contact. We observe that when in contact with metal, states emerge within the band gap of phosphorene due to considerable changes in its atomic structure, a phenomenon influenced by various factors. All metal-phosphorene contacts show an increased amount of DOS inside the band gap, in the vicinity of the Fermi level, which is indicative of metallization of the contacted phosphorene. In Fig [**?**], significant changes in the DOS within the band gap are caused by the chemical interaction of highly adhesive type 2 metals, which can substantially distort the atomic arrangement of phosphorene (see Fig. [**?**]). Notably, some type 2 metals (Nb, W, M, and Ta) have lattice parameters similar to those of phosphorene lattice. This leads to a specific atomic arrangement at the interface as depicted in Fig. 3.7, that maximizes orbital overlap, resulting in a stronger chemical bond resulting in the creation of DOS within the band gap of phosphorene (see Fig. 3.4d). A considerably increased

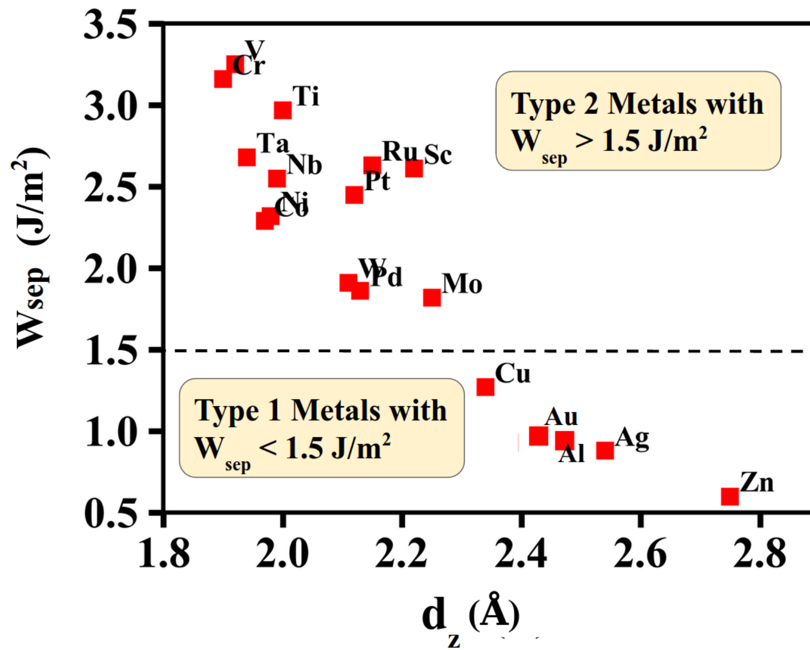

(a)

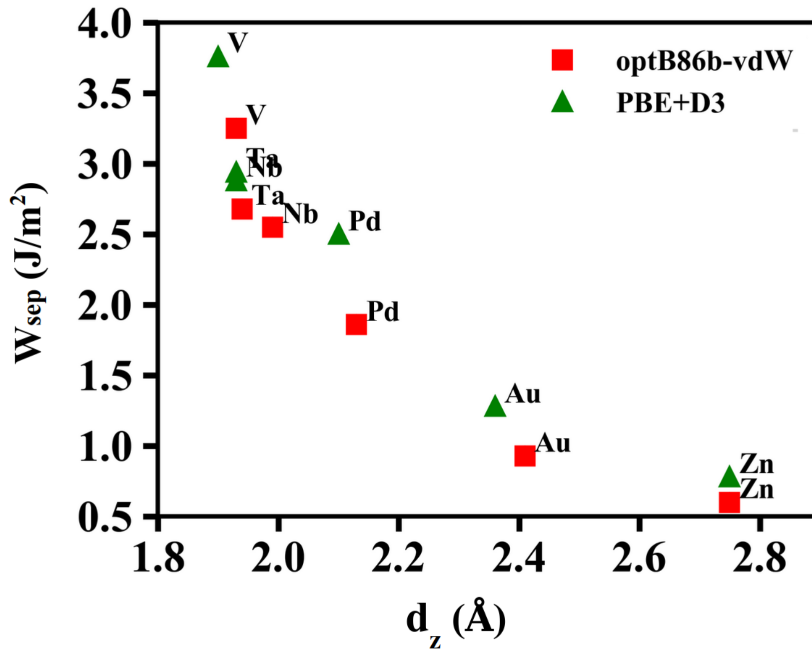

(b)

Figure 3.3: (a) The interface adhesion strength calculated in terms of W_{sep} are plotted against average interfacial equilibrium distance (d_z). A consistent decreasing nature of W_{sep} with d_z suggests a strong correlation between the two. (b) d_z vs W_{sep} plot for a subset of meta-phosphorene cases presented using two different functionals. Absolute values are different, however, the decreasing trend of W_{sep} with d_z remains intact. (Reproduced from Ghaffar *et al.* [92] under CC BY-NC-ND license.)

orbital overlap also facilitates efficient carrier injection across the direct contact interface, reducing contact resistivity by exhibiting an Ohmic nature. Conversely, for type 1 metals, the contacted portion of phosphorene demonstrates metalization (states within the band gap), but the change in DOS is not as prominent as in type 2 metals. This is expected because the interaction between type 1 metals and phosphorene involves weaker bonds. For instance, Fig. 3.4c illustrates that the DOS within the band gap of Au-contacted phosphorene (a type 1 metal) remains relatively similar to pristine phosphorene. Additionally, van der Waals forces and strain on the phosphorene layer may contribute to changes in DOS.

Despite the fact that all metals lead to phosphorene metalization, distinguishing metals solely based on their contact resistance via DOS analysis is challenging. However, we can establish a qualitative analysis based on the degree of DOS in the phosphorene band gap. Therefore, a quantitative differentiation among metals regarding their ability to form low-resistance contacts requires further analysis. Fig. 3.5a illustrates a schematic representation of a standard 2D-FET, showcasing the metal-phosphorene interface formed ath the source and drain contact regions. Two separate interfaces are present: (a) the interaction between the metal and phosphorene (along AB), and (b) the interaction between metallized and unaltered phosphorene in the FET channel region (along CD). Understanding the tunnel barrier across AB and the Schottky barrier across CD is crucial for getting a comprehensive insight into the electrical properties of metal-phosphorene contacts because, even though interface AB is metalized, the existence of a tunnel barrier is dependent upon the strength of the bond between the metal and phosphorene. Additionally, the work function difference between pristine and metalized phosphorene across interface CD can create a lateral Schottky barrier, affecting carrier flow across CD and consequently influencing the overall contact resistance.

3.4.2 Schottky Barrier Analysis

Fig. 3.6 displays the calculated work function ϕ_{M} for all metal-phosphorene systems considered in this study, alongside E_{C}, E_{V}, and the Fermi-level (E_{F}) of pristine phosphorene. The calculated Schottky barriers for electrons and holes ($\Phi_{\mathrm{B,n}}$ and $\Phi_{\mathrm{B,p}}$) are presented in Table 3.1. The metals with higher ϕ_{M} (Cr, Co, Nb, Cu, and V) form p-type Schottky contacts at the CD interface, while the metals with lower ϕ_{M} (Sc, Sc, Ti, and Zn) form n-type Schottky contacts at the CD interface. It is important to note that all negative SBH values can be adjusted to zero, representing Ohmic contact for either electron or hole conductivity. Additionally, Ni, Pt, Pd, Ru, Ta, W, and Au exhibit Ohmic contact, and no ambipolar characteristics are observed. The SBH values obtained in this study are compared with previous theoretical investigations in Table 3.2. It's noteworthy that the results of this study align with some prior research but diverge from others. This variance can be attributed to the sensitivity of first-principles calculations to the computational methods employed for barrier calculation. For instance, Pan *et al.* [17] used the Schottky-Mott method to calculate the Schottky barrier for lateral conduction (interface CD, as depicted in Fig. 3.5a), whereas Chanana *et al.* [19] only took into account barrier formation for vertical conduction (interface AB, illustrated in Fig. 3.5a) during carrier injection. The results also depend on simulation parameters such as the exchange-correlation functionals, k-points mesh size, and threshold energy for structural optimization. Hence, conducting a comprehensive study encompassing a diverse range of metals with consistent simulation parameters, as executed in this work, has pivotal importance. Furthermore, establishing a universally applicable numerical value for specific parameters remains challenging. Rather than directly comparing absolute SBH values from different studies, it's more informative to analyze the trends in SBH values across different contacts, employing a uniform set of parameters. This approach aligns

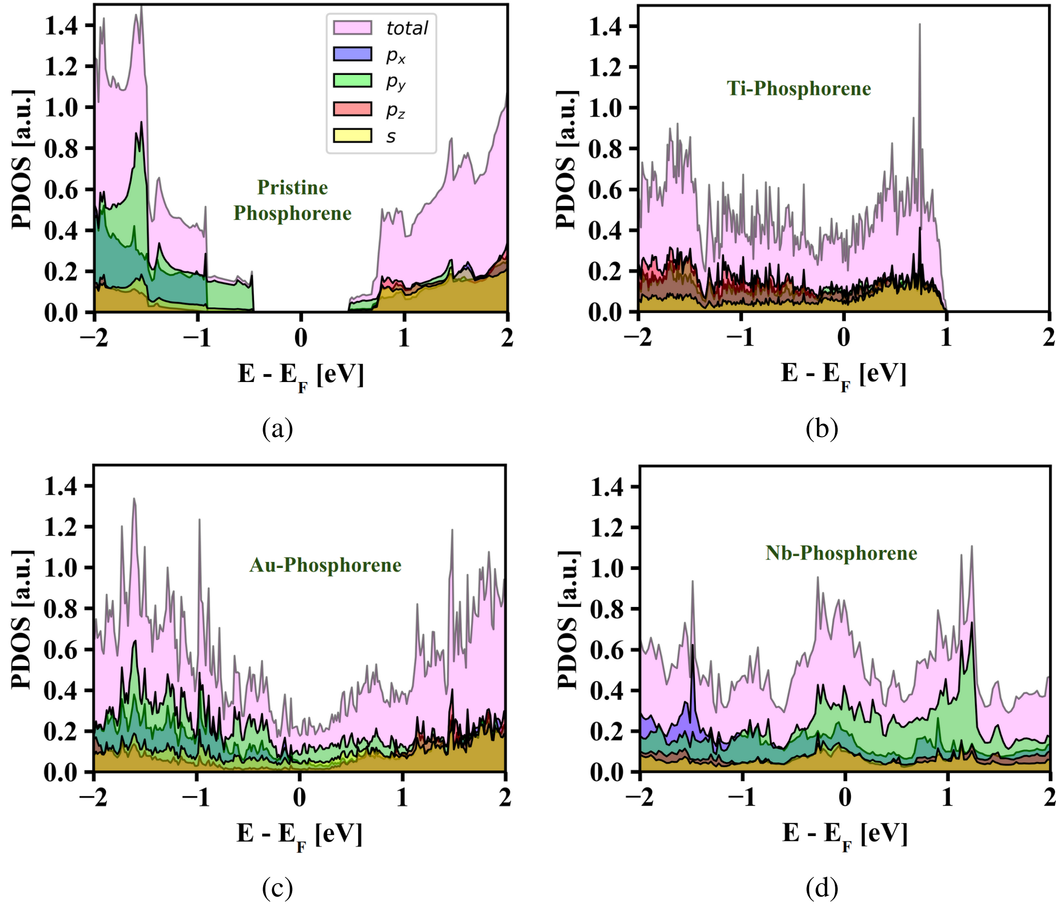

Figure 3.4: Four different representative partial density of states (PDOS) plots are given; (a) pristine phosphorene without metal contact, (b) Ti-phosphorene, (c) Au-phosphorene, and (d) Nb-phosphorene systems. In all the metal-phosphorene contact systems, a finite density of states (DOS) appear within the band gap, indicating the metallization of phosphorene at the vertical contact interface. Notably, type 1 metals exhibit lower DOS within the band gap of phosphorene than that of type 2 metals, which demonstrate a higher DOS within the band gap. The vertical axis is represented in arbitrary units because our analysis is rather qualitative in terms of DOS around the Fermi level of phosphorene. (Reproduced from Ghaffar *et al.* [92] under CC BY-NC-ND license.)

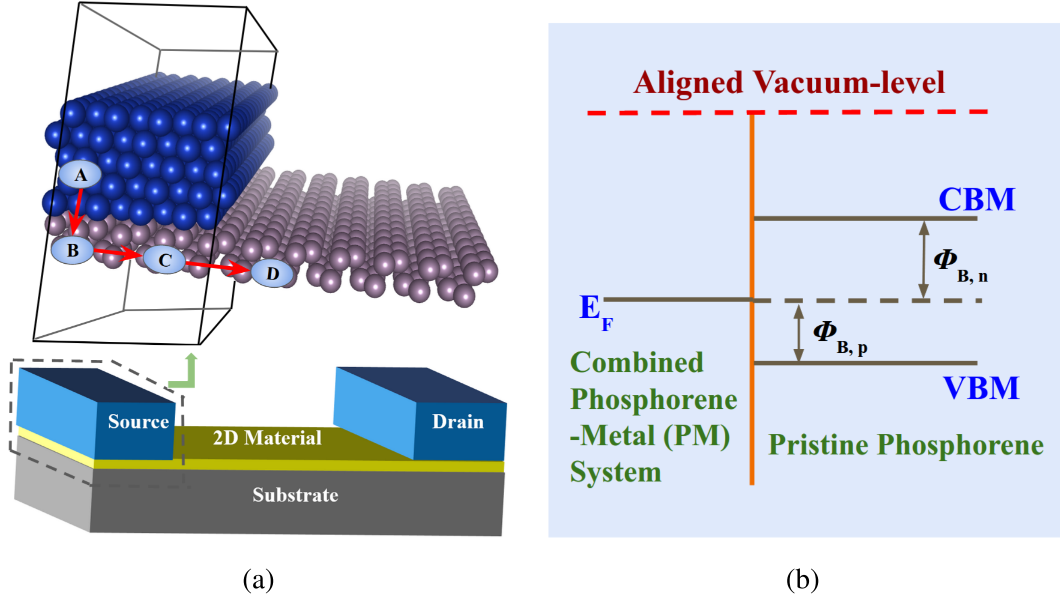

(a) (b)

Figure 3.5: (a) A schematic illustration of the structure of a typical Field-Effect Transistor (FET) based on 2D materials (2DMs). The source and drain regions are contacted with metals forming metal-phosphorene contacts. An atomic structure depicting the simulated part represented by a 3D-box in addition to extended channel region is shown. Path $A - B - C - D$, denotes the interfaces charge carriers must pass encountering two interfaces: AB (vertical interface), located between the metal and the contacted phosphorene, and CD interface occurring between the contacted phosphorene and the pristine phosphorene extending into the channel part. (b) Application of modified Schottky-Mott method to calculate the Schottky barrier heights (SBHs) for the CD interface. In this diagram, E_{F} represents the Fermi energy of the combined metal-contacted phosphorene system. The difference between E_{F} and CBM/VBM yields the n-type/p-type SBH. (Reproduced from Ghaffar *et al.* [92] under CC BY-NC-ND license.)

with the findings of experimental studies by Das *et al.* [93] and Du *et al.*[94], where the hole Schottky barrier exhibited the same trend for metals Pd, Ni, and Ti (Pd < Ni < Ti).

3.4.3 Tunneling Barrier Analysis

As was previously mentioned, charge transfer and, by extension, contact resistance can be greatly affected by the existence of a tunnel barrier at interface AB (vertical interface) between the metal and phosphorene. The likelihood of carrier tunneling across interface AB depends on the tunnel barrier's height (T_b) and width (d). In Fig. 3.8, the height and the width of the mid-gap region, which represents the region between the metal and phosphorene along vertical interface, in the planar-averaged electrostatic potential plot, is used to determine T_b. Based on the calculations carried out in this study, type 1 metals have a higher T_b, whereas type 2 metals show a T_b of negative or zero. The negative T_b appears as a consequence of the Fermi level lying above the tunneling barrier indicating electrons residing in the highest occupied states have higher energy than the barrier they encounter at the interface. This observation is explained by the bonding strength of the metal-phosphorene contact; however, it is important to remember that an overly strong bond at the interface is not always desirable. Metals with extensive orbital overlap with phosphorene, such as Mo, W, Nb, and Ta, form very strong bonds that may even be stronger than the intralayer phosphorene P-P/armchair bond. This can lead to the disruption of

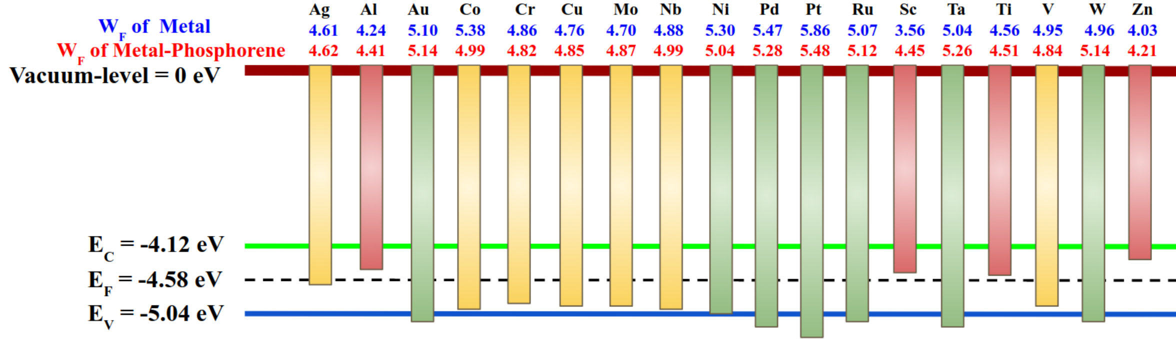

Figure 3.6: Illustration of the work function (W_F) of the metal-phosphorene interfaces aligned into the band gap of the pristine phosphorene. The vertical bars alignment with the conduction band minima (E_C) and valence band maxima (E_V) allows us to calulcate the contact polarity in addition to the calculation of their lateral SBHs. The W_F of the bulk metal is represented in blue font, enabling the direct, side-to-side comparison with W_F of interfaced metals. (Reproduced from Ghaffar *et al.* [92] under CC BY-NC-ND license.)

Table 3.2: The following table represents the comparison of SBHs ($\Phi_{B,n}$ and $\Phi_{B,p}$) with earlier reported values available in published literature.

Metal	SBH [17]	SBH [19]	SBH [18]	SBH (this work)
Al(110)	0.23/0.68	NA	NA	0.29/0.63
Au(110)	0.71/0.20	NA	0.89/0.01	1.02/0.00
Cr(110)	0.58/0.33	NA	NA	0.70/0.22
Cu(111)	0.76/0.15	NA	NA	0.73/0.19
Ni(111)	0.89/0.02	NA	0.18/0.72	0.91/0.00
Pd(111)	0.00/0.00	Ohmic	0.93/0.00	1.16/0.00
Ti(0001)	0.40/0.51	Intermediate	0.41/0.49	0.39/0.53

the intra-phosphorene armchair bond or a significantly distorted atomic structure (see Fig. 3.2). The broken bond induces an intra-phosphorene layer tunnel barrier. For instance, refer to Fig. 3.8 (c), where an electrostatic potential peak is observed within the phosphorene region, not in the mid-gap area. This peak suggests the presence of an intra-phosphorene tunnel barrier (TB), requiring electrons to tunnel through the barrier located within the phosphorene layer. This can exacerbate the carier injection efficiency due to extra tunneling barrier. As a result, even while these metals might not directly create a tunnel barrier at the metal-phosphorene interface, they might nevertheless have a high charge flow resistance, which would increase contact resistance overall.

To provide a quantitative perspective, we calculate the carrier tunneling probability (T) across interface AB. To accomplish that, the full-width half-maxima (FWHM) of the mid-gap, the peak above the Fermi level in the planar-averaged electrostatic potential plots, is used to estimate the form of the tunnel barrier, giving it an approximated square shape with a barrier height T_b and width d. The T is determined by the formula,

$$T = \exp\left(-2\sqrt{\frac{2mT_b}{\hbar^2}}d\right), \tag{3.4.1}$$

where, m and $\hbar$ represent the carrier's effective mass and the reduced Planck's constant, respectively. Type 1 metals Ag, Al, Au, Cu, and Zn have calculated T values of 50%, 66%, 51%, 74%, and 44%, respectively. On the other hand, T is 100% for all type 2 metals, at least for the vertical interface. Some of the type 2 metals, however, have intra-phosphorene tunnel barriers, as previously mentioned, estimated T values for Mo, Nb, Ta, and W are 79%, 35%, 20%, and 29%, respectively. Although Mo, Nb, Ta, and W exhibit higher adhesive strength and lower Schottky barrier height (SBH) at interface CD, the presence of an intra-phosphorene tunnel barrier could contribute to higher contact resistance. Consequently, a comprehensive analysis that considers both SBH and TB with consistent simulation criteria offers valuable insights into the electrical properties of MS contacts.

3.4.4 Mid-Interface Charge Density (MICD)

At the metal-semiconductor interface, there can be localized electronic states known as interface states. These states can trap charge carriers, leading to a variation in the charge density. The presence and distribution of these states can significantly impact the charge density. The interface states and in turn the charge density at the MS interface depends on various factors, including the properties of the metal and the semiconductor; Some of these properties include electronegativity, work function, and lattice mismatch. The mid-interface charge density (ρ) is calculated at the mid-point of the interface AB, which theoretically represents the electron localization due to molecular bond formation taking place between metal-phosphorene atoms at the interface. Although chemical bonding at the interface is the basis for adhesion, the bonding electrons are expected to be localized in the middle of the interface or slightly shifted towards the more electronegative atoms. Moreover, MICD provides an additional method to evaluate metal contacts with superior mechanical strength and electrical conductivity. It's important to note that bonding strength is closely connected to the degree of charge involvement in bonding. Consequently, ρ is anticipated to increase with W_{sep}. Fig. 3.9a illustrates ρ with respect to W_{sep}, and as anticipated, ρ rises in tandem with higher W_{sep}. Visualizations of ρ for two metals, (a) Cr (with the highest ρ value), and (b) Zn (with the lowest ρ value), are provided in Fig. 3.9b. This observation indicates that the lower-adhesive metals (Zn, Au, etc.) are physisorbed on the phos-

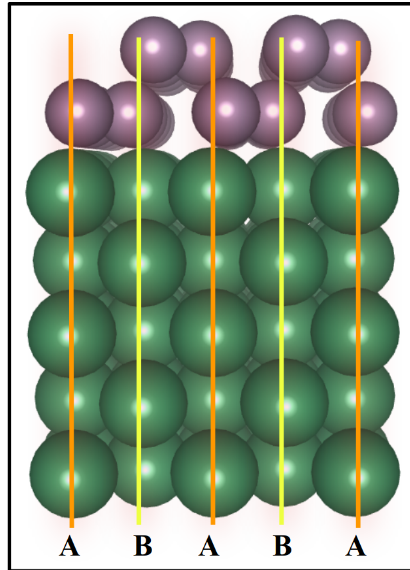

Figure 3.7: This figures represents strong atomic overlap. Metals with lattice parameters matching those of phosphorene form interfaces with maximum atomic overlap or orbital overlap. In this study, Nb, Ta, Mo, and W reprsent such metals. (Reproduced from Ghaffar *et al.* [92] under CC BY-NC-ND license.)

phorene surface facilitated through van der Waals interaction, whereas higher-adhesive metals (V, Ti, Sc, Cr, etc.) are chemisorbed on the phosphorene surface mediated from the covalent bond formation, along the interface bonding strength.

Planar-averaged charge density calculation along the z-direction (normal to the interface) was carried out in order to determine ρ, as Fig. 3.10 illustrates. Table 3.1 provides a summary of the ρ values for all eighteen metal MP-interfaces that were taken into consideration in this study. Notably, In Fig. 3.9, Sc and Ti exhibit deviations from the general ρ vs. W_{sep} trend. While the specific reasons for this deviation are not entirely clear, an interesting observation is presented in Figure 3.11. This figure depicts the intrinsic resistivity values of the metals [95], revealing that Sc and Ti, the metals deviating from the ρ-W_{sep} trend, also have the highest metallic resistivity. Though this is an exception, generally speaking, ρ can be used to indicate higher mechanical strength or chemical bonding. Metals with higher ρ values are also anticipated to show improved conductivity for interface AB. That being said, it is important to keep in mind that overall conductivity and, consequently, electrical behavior, rely on both interfaces. For this reason, both Schottky and tunneling barrier heights continue to be excellent indicators for evaluating ”good” quality metal contacts for phosphorene-based FET devices.

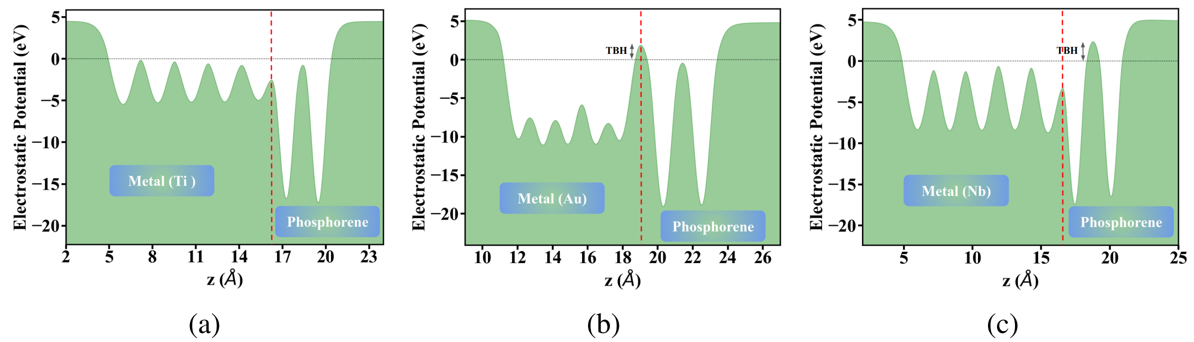

Figure 3.8: Figures showing the planar averaged electrostatic potential prependicular to the interface: (a) Ti-phosphorene, (b) Au-phosphorene, and (c) Nb-phosphorene contact interfaces. The dotted horizontal line at 0 on the vertical axis, and the dashed red vertical line represent the Fermi level and the mid-interface point, respectively. The tunnel barrier heights can be determined from the potential difference between the peak of the potential at the mid-interface and the Fermi level. (Reproduced from Ghaffar *et al.* [92] under CC BY-NC-ND license.)

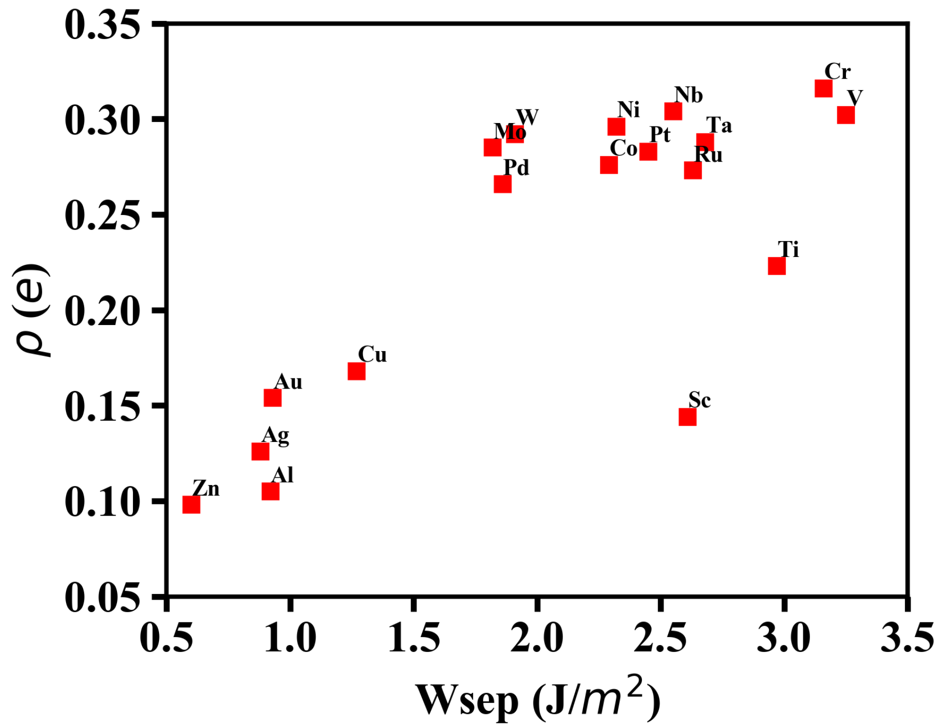

(a)

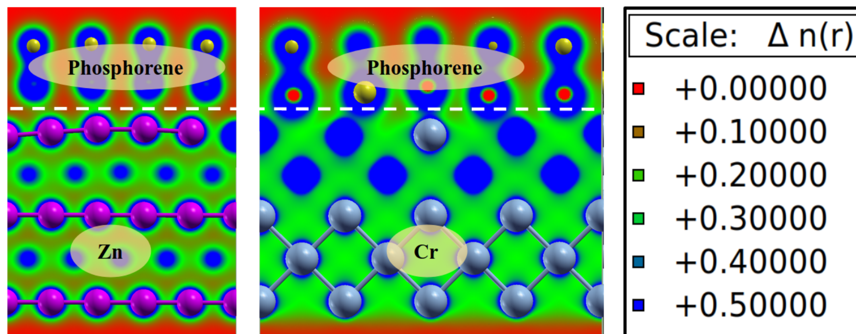

(b)

Figure 3.9: This figure depicts the interface charge density; (a) displays the mid-interface charge density (ρ) varying with work of separation (W_{sep}) for different interfaces, demonstrating a clear positive correlation of ρ with W_{sep}. (b) A visualization of ρ for Zn (type 1 metal) and Cr (type 2 metal) interfaced with phosphorene. It can be noted that the Zn-based phosphorene interface exhibits the lowest ρ, while the Cr interface presents an example for the high ρ. (Reproduced from Ghaffar *et al.* [92] under CC BY-NC-ND license.)

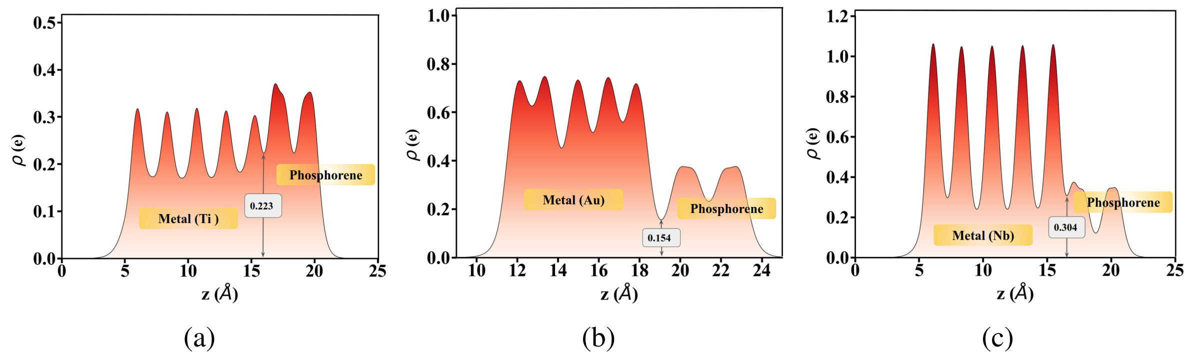

Figure 3.10: The planar averaged charge density, perpendicular to the interface is presented for 3 distinct representative phosphorene-metal cases. (a) Ti-phosphorene is given as an example of highly adhesive type 2 metals, (b) Au-phosphorene represents the lower adhesive metals (type 1), and (c) Nb-phosphorene is an example for the cases with broken intra layer armchair P-P bond upon metal contact. (Reproduced from Ghaffar *et al.* [92] under CC BY-NC-ND license.)

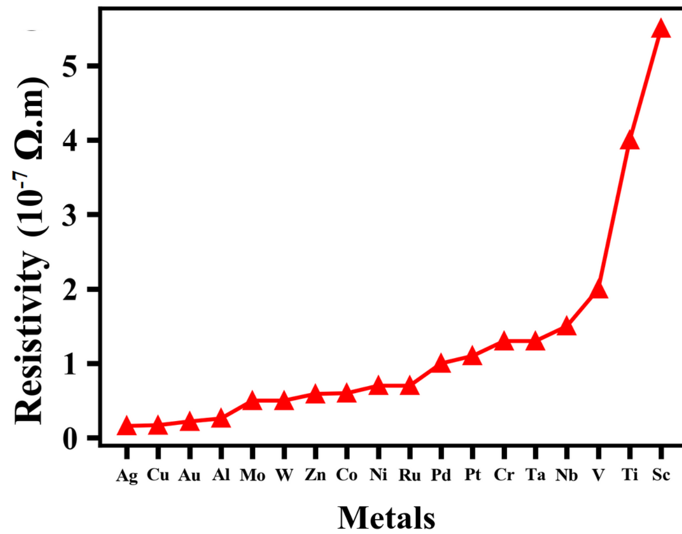

Figure 3.11: The resistivity of all the metals employed for the interface construction with phosphorene. Sc, Ti, and V are the metals with highest resistivity among all the metals used in this study. (Reproduced from Ghaffar *et al.* [92] under CC BY-NC-ND license.)

Chapter 4

WS_2-Metal Contact

4.1 Background

Two-dimensional (2D) semiconductors, widely known for their flexible mechanical and electronic properties, have significantly expedited research endeavors focused on their integration into cutting-edge flexible electronic and optoelectronic devices. Their remarkable versatility has unlocked a wide spectrum of applications, spanning across electronics [96, 97], optoelectronics [98, 99], sensors [100, 101], and biomedical devices [102, 103]. Among the diverse array of 2D semiconductors explored thus far, transition metal dichalcogenides (TMDs) have accumulated substantial attention. In this category, WS_2 has emerged as a formidable 2D semiconductor, primarily attributed to its recent accomplishments in prototype device applications [104, 105, 106]. However, the presence of parasitic contact resistance presents a formidable obstacle in the quest for high-performance devices. Efforts have been dedicated to tackling and mitigating this problem [107, 108, 109, 110]. Several techniques have been employed to curtail resistance, encompassing modifications at the interface and surface levels, including: 1) Surface Functionalization [111, 112], 2) Doping [113, 114], 3) Interface Engineering (leveraging suitable metals) [25, 115], and 4) Surface Passivation [51, 116, 117].

Multiple experiments [118, 119, 120, 121], have successfully demonstrated controllable doping techniques for TMDs , which offers a promising approach to enhance the contact properties of WS_2/metal interfaces. The dopants used in these experiments, such as P, C, and N, have a significant chemical influence on WS_2 [122, 123]. Consequently, diverse contact tunable properties can be envisaged. For example, these dopants shift the Fermi level toward the valence band minima by creating acceptor states, thereby promoting p-type conductivity, which is highly desirable in pristine TMD/metal contact systems as these interfaces typically lead to n-type contact behavior due to Fermi level pinning (FLP) close to the conduction band edge (E_c). At the same time, Cl and F can be classified as a n-type dopants due to their ability to derive donor states within the band gap close to the conduction band, whereas O-dopants being isoelectronic to Sulfur generally expected to show very insignificant effect on WS_2's electronic properties. Nevertheless, due to the metal-induced gap states (MIGS) formation, the above mentioned characteristics of different dopants are expected to undergo very complex interactions thereby making it essential to carry out an analysis to classify the ability of different dopant systems to alter and provide an efficient route for improved engineered contact interfaces. The emergence of acceptor states caused by p-type dopants suggest a potential for Fermi level depinning (FLDP). However, the comparative ability to produce p-type contact properties with different dopants, and their correlation with other contact properties, is still not addressed. This highlights the need for a comprehensive investigation of chalcogen-substituted WS_2 to quantify

the reduction in metal-induced gap states (MIGS) and its correlation with FLDP. By studying these aspects, we can gain valuable insights into substitutionally doped systems as a contact resistance mitigation technique.

In general, TMDs show higher stability with metal-rich systems than chalcogen rich [46], which explains the fact that chalcogen substitution is energetically more favorable than transition metal (TM) substitution. In addition, S-vacancy exhibit shallows trap states while TM vacancies are associated with deep-trap states. In this vain, Kim *et al.* [47] demonstrated experimentally that S-vacancy causes more impurities and disorders in WS_2 compared to W-vacancy resulting in 10 times higher doping concentration in tandem with 4 times higher Coulomb scattering coefficient, due to the formation of shallow doping level [48], which makes it chemically more active. Moreover, Wang *et al.* [49] suggest that various defects such as B, C, N, O, F, and P doping and S-vacancy can be used to activate the inert basal planes of 2H-phase MoS_2 causing impurity states to be introduced in the lower energy levels. Furthermore, in the light of above discussion, recent developments in chalcogen substitution-based studies has been carried out to achieve improved device performances employing non-metallic dopants: P [37, 44, 45], C [37, 44, 45], N [26, 39, 45], F [38, 43, 50], O [42, 45, 51], Cl [41, 45, 52, 53, 54]. However, it remains a long-standing challenge to quantify the relative performance of different chalcogen-substituted WS_2/metal interfaces over a set of metals having varying chemical properties. In this light, our study involves a selection of several highly ubiquitous dopants such as P, C, N, O, and F, and metals including Ag, Au, Cu, Pd, Pt, Sc, and Ti , in the search for a more comprehensive understanding of the tunability in their contact properties with/without substitutionally doped systems. The above considerations along with the fact that the characterization of relative contact properties of different systems require a consistent set of simulation criteria, increases the importance of this study on S-substituted WS_2/Metal contact. We believe that this study can help fundamental research and provide insight towards defect-assisted metal/TMDs contact properties in the experimental fabrication for the next-generation device application.

4.2 Results and Discussions

Analyzing 2D semiconductors through experimental methods poses a significant challenge due to the increased strength of the effective Coulomb interaction in low dimensions along with the requirement of highly sophisticated handling techniques to prevent sample contamination. This enhanced interaction is a result of dimension-related effects that are typically overlooked in experimental studies. However, theoretical modeling based on first-principles theory has successfully characterized the properties of 2D materials, offering a relatively accurate analysis of their relative properties. Although the DFT calculations may not accurately predict the precise location of semiconductor band edges, they provide a useful framework to guide the experimental synthesis.

To successfully model the contact interface, we constructed several metal surfaces interfaced with a monolayer of WS_2. Previous research indicates that only the contact layer of TMDs can accurately capture the overall contact behavior [54, 115]. This justifies our modeling approach using a monolayer of WS_2, and we can justify that the insights gained in this study may have broader applicability to other TMDs. This is because the 2H-hexagonal phase of TMDs, which represents the semiconducting polytype of TMDs, generally exhibits similar chemical interactions.

4.2.1 Binding Strength and Mechanical Stability

Before conducting the interface analysis, we first assessed the relative stability of monolayer-WS_2 doped systems (system shown in Fig. 4.1), in terms of binding energy (E_b). Positive E_b values indicate the system's stability. Notably, we found that dopants C, N, and O exhibited higher E_b values compared to pristine-WS_2 when considering S as a dopant. Conversely, P, F, and Cl demonstrated lower E_b values. The variability in binding strength among different dopants likely arises from factors such as the dopant's electronegativity, atomic size, and their similarity to sulfur in accommodating broken bonds from S-vacancies.

Our study revealed a valuable insight into doped-WS_2 systems; they have the potential to enhance chemical interactions upon contact with metals. For instance, doped-WS_2 with higher E_b values may lead to reduced chemical reactivity, when metal/WS_2 interface is formed. This has the potential to enhance non-covalent interaction in the form of van der Waals contacts. This, in turn, could help suppress the formation of metal-induced gap states (MIGS) and increase the Fermi level depinning (FLDP) phenomenon. Furthermore, our band structure analysis confirms the roles of the dopants as acceptor dopants (C, P, and N), donor dopants (Cl, F), and neutral dopants (O). As depicted in Fig. 4.2, we observed a strong and consistent correlation between the average interface separation and Binding Energy (BE), which was also discussed in our study [92] with phosphorene-metal interfaces. Specifically, we calculated a notably high negative correlation coefficient, typically exceeding -0.95. The average interface separation (d_z) does not only highly correlate to the binding strength, but it also plays an important role when calculating the tunneling barrier at the interface. It's essential to note that the movement of interfacial atoms, influenced by chemical interactions at the interface, whether with or without dopant substitution, can introduce complexities in determining the precise interfacial distance. To address this challenge, we employed K-means clustering, an unsupervised machine learning algorithm, along the z-coordinates (the interface direction). In this approach, the number of clusters (K) was set equal to the total number of atomic planes, yielding K-centroids, each representing the average z-coordinate value for a specific atomic plane within the system. This method ensures robust results as the number of clusters (atomic planes) was already known. Surprisingly, contrary to our initial expectations, we observed that all p-type doped interfaces, on average, exhibit enhanced BE values compared to the pristine interface. This suggests that p-type dopants not only reduce the Schottky barrier height (SBH) but also contribute to the further stabilization of the contact interfaces. Furthermore, as discussed in Section 4.2.2, this behavior indicates the potential for lower Fermi level pinning (FLP), resulting in reduced p-type SBH values.

To delve further into our study, we also examined charge rearrangement for various doped and pristine cases. Surface passivation techniques aiming to reduce the hole SBH through the insertion of 2D layers and other functionalization techniques involve a tradeoff. This tradeoff stems from the need to balance the reduction in SBH due to FLP due to MIGS suppression against the increase in tunnel barrier height (TBH) resulting from an extended semiconductor-metal interfacial distance. Significantly, our observation that E_b increases with C, P, and N dopants as d_z reduces provides valuable insights into TBH. The strong negative correlation between E_b and d_z, as evident in Fig. 4.2, implies that an increase in E_b accompanies a reduction in the tunneling distance, facilitating the electron flow across the interface more effectively by overcoming the tunneling barrier height. In addition, contacts with higher/lower BE/d_z ratios can not only, indirectly impact TBH but also SBH, as they direct relation to the formation of MIGS, which arises from enhanced orbital overlap due to intimate contact at the metal-semiconductor (MS) interface. In the subsequent sections, we explore the interplay between E_b

and various parameters across different systems.

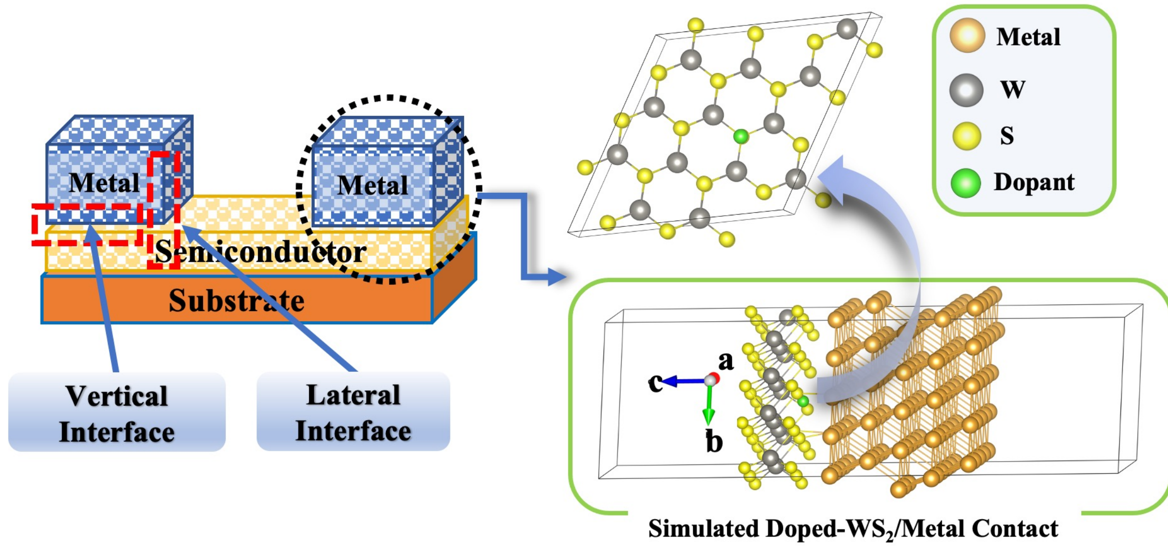

Figure 4.1: Schematic diagram of a typical Field Effect Transistor (FET). The dotted circular part has been simulated as illustrated on the RIGHT. Both the pristine-WS_2/Metal and doped-WS_2/Metal interface is modeled as depicted in the figure.

4.2.2 Schottky Barrier Analysis

Two of the crucial interfaces directly responsible for overall contact resistance are vertical interface (direct metal-semiconductor contact) and the lateral interface (contact between interfaced-semiconductor and the semiconductor in the channel) as depicted in Fig. 4.1. In Figure 4.4, we present the vertical SBH data using bar graphs; numerical values for all the doped and undoped (pristine) systems are listed in Tab. 4.1. These graphs not only illustrate SBH trends among various metals but also provide insights into their respective impacts on the SBH modification in the substituted systems. The top-left figure represents the Schottky-Mott SBH calculated using energy levels of isolated metals and WS_2 with the aligned vacuum level. Notably, P, C, and N-substituted cases result in a clear reduction in p-type SBH, as anticipated from the doped-WS_2 study in Section 4.2.1. Similarly, n-type dopants Cl and F generally reduce n-type SBH. In contrast, the O dopant, considered iso-electronic to the replaced S-atom and termed a neutral dopant, shows minimal deviation from the pristine case. From the numerical values of SBH presented in Tab. 4.1, it can be witnessed that despite significant Fermi level shifts towards the valence band in the case of C, N, and P-substituted WS_2, the corresponding contact systems do not produce SBH variation in the same proportion. The relative SBH trend follows N < P < C, while Cl, F, and O follow a general trend, though not strictly - O < F < Cl. The variation in SBH strength with different metal electrodes aligns with a recent theoretical study [53], which examined the effect of Cl-doping on Ag and Pd-metal electrodes. These variations can be reasonably explained by the dopants' potential to introduce acceptor/donor impurities into the WS_2 layer, as elaborated in Section 4.2.5. Ongoing experimental studies dedicated to doped TMDs-Metal contacts are in excellent agreement with our analysis [118, 119, 122, 124, 125]. Furthermore, we expect to explain the transition of SBH behavior towards p-type/n-type contacts in light of the strength of p-type/n-type dopants in suppressing/enhancing metal-induced

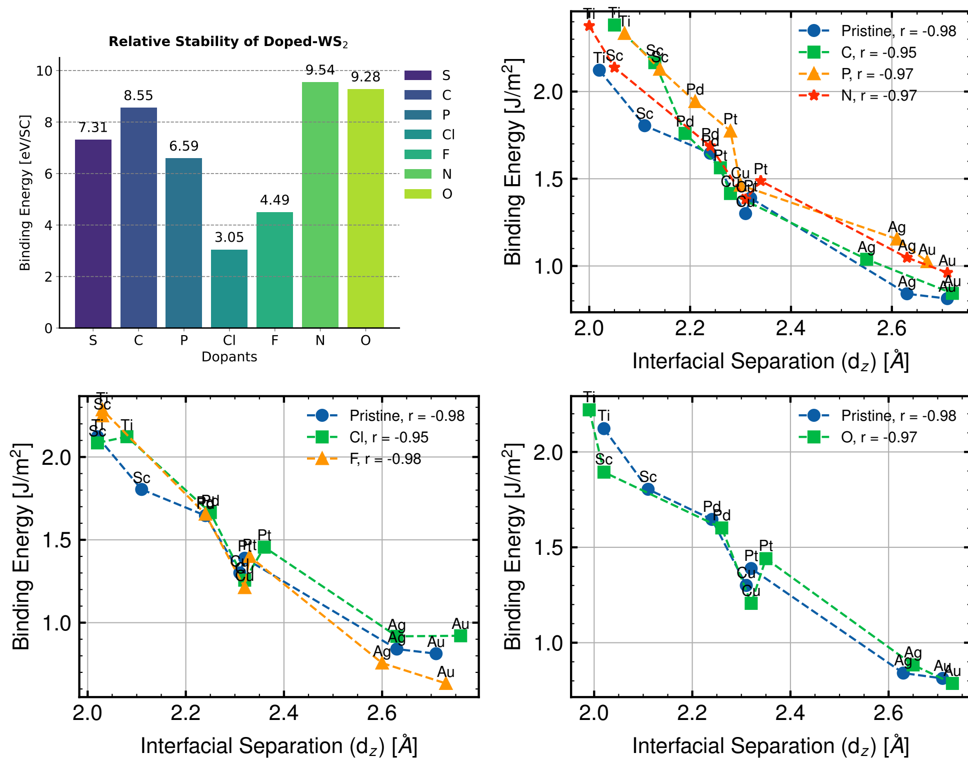

Figure 4.2: Binding energy for all the systems, both with and without S-substitution. To facilitate a direct comparison of relative variations among different cases in relation to the pristine case, these systems are categorized into three distinct groups: 1. p-type dopants(C, P, N), 2. n-type dopants (F, Cl), and 3. neutral dopants (O).

gap states (MIGS), as will be discussed in the following section. As predicted, the nature of dopants can be categorized into three distinct groups based on their ability to tune energy levels into n-,p-type polarity: 1. n-type inducing (F, Cl), 2. p-type inducing (P, C, N), 3. neutral (O). While these dopants do not transform the contact polarity into what is based on this distinction, significant changes are exhibiting clear induction of acceptor/donor characteristics in line with the above classification for the vertical interface. Additionally, calculated SBH for the lateral interface can be observed in Fig. 4.3. The polarity and absolute values of SBH largely align with the SBH based on the idealistic Schottky-Mott model [67, 68] , as illustrated in Fig. 4.3. This suggests that the carrier polarity of the lateral interface is largely independent of doping characteristics at the vertical interface. The can be reasoned by examining the main parameters that influence the lateral SBH, which are the work function and interface dipole correction of the combined WS_2-metal interface in the light of Eq. (2.8.3), and Eq. (2.8.4). Note that this calculation of the lateral SBH is based on the modified Schottky-Moot method, which also considers the variations in the work function of the metal resulting from interface formation. We notice that the work function of metals does not vary considerably across all the doped systems - at least not according to the doping characteristics. This provides sufficient explanation for why doping has small effect on the polarity or value of the lateral SBH in general.

Table 4.1: Vertical SBH for all the interfaces has been calculated employing fat band technique, as given here along with other relevant parameters. The E_g, Φ_n^V, and Φ_p^V denote the band gap, n-type SBH, and p-type SBH, respectively in the unit of eV. Metal-induced gap states (MIGS) are given in the units of states/eV/Å^3.

Dopant	Metal	Calculated Properties			
		Φ_n^V	Φ_p^V	E_g	MIGS
Pristine	Ag	-1.589	0.145	1.734	2.940
	Au	-1.360	0.350	1.710	3.857
	Cu	-1.563	0.212	1.775	5.471
	Pt	-1.100	0.580	1.680	8.423
	Pd	-1.128	0.754	1.882	8.037
P	Ag	-1.351	0.370	1.721	3.065
	Au	-1.010	0.673	1.683	3.289
	Cu	-1.433	0.314	1.747	5.236
	Pt	-0.969	0.705	1.674	7.947
	Pd	-0.998	0.918	1.916	9.868
C	Ag	-1.095	0.513	1.608	3.793
	Au	-0.805	0.815	1.620	3.594
	Cu	-1.244	0.400	1.644	5.839
	Pt	-0.937	0.698	1.635	8.572
	Pd	-0.971	0.904	1.875	7.583
N	Ag	-1.370	0.280	1.650	3.908
	Au	-1.022	0.618	1.640	3.728
	Cu	-1.475	0.290	1.765	6.905
	Pt	-1.010	0.618	1.628	7.260
	Pd	-1.030	0.830	1.860	6.878
Cl	Ag	-1.657	0.004	1.661	3.145

Continued on next page

Table 4.1 – continued from previous page

Dopant	Metal	Calculated Properties			
		Φ_n^V	Φ_p^V	E_g	MIGS
	Au	-1.562	0.162	1.724	5.543
	Cu	-1.631	0.066	1.697	6.097
	Pt	-1.152	0.498	1.650	8.855
	Pd	-1.217	0.633	1.850	8.904
F	Ag	-1.563	0.196	1.759	5.606
	Au	-1.240	0.460	1.700	5.023
	Cu	-1.586	0.220	1.806	8.399
	Pt	-1.200	0.390	1.590	9.105
	Pd	-1.220	0.556	1.776	9.240
O	Ag	-1.710	0.005	1.715	2.827
	Au	-1.400	0.300	1.700	3.422
	Cu	-1.595	0.202	1.797	6.060
	Pt	-1.132	0.510	1.642	8.016
	Pd	-1.161	0.681	1.842	7.114

4.2.3 Tunnel Barrier and Tunneling Probability

In principle, the interface tunneling width (denoted as d_z) and tunneling barrier (referred to as "T_b") both impact the overall tunneling resistance, making the calculation of tunneling probability (T) an essential means of quantifying both the interface properties into a single quantity as expressed through Equation 2.7.2. As shown in Figure 4.6, metals Sc and Ti exhibit a T equal to 1, implying zero barriers for carrier flow. This is due to the formation of an extremely close contact between the metal and WS_2. In contrast, other metals display a tunneling probability of less than 1, largely dependent on their degree of affinity for binding to the WS_2 surface. This affinity, in turn, is linked to the degree of overlap of atomic wave functions, leading to a greater possibility of chemical bonding at the interface region, a key factor responsible for the formation of metal-induced gap states (MIGS). Consequently, less reactive metals like Ag, Au, and Cu yield the lowest T values across all the substituted cases. Typically, the phenomenon of Fermi level depinning (FLDP) can be associated with lower tunneling probability. Interestingly, we observe that interfaces substituted with C, P, and N, which can induce FLDP, generally show a significant increase or remain more or less the same in terms of T-values across all metals except Au. Note that the governing parameter associated with T can be linked to the various interface properties: the number of valence electrons, electronegativity difference, ionic charge, steric effects, interface environment, oxidation states, reactivity, and more. In line with this, Au, being highly non-reactive and having the lowest electronegativity difference (2.58 (S) - 2.54 (Au) = 0.04), mainly forms van der Waals interfaces. This leads to a substantial reduction in adhesion upon doping because the dopants move away from the metal surface (Z_d) further reducing chemical interaction. Additionally, the decrease in van der Waals interaction energy as $\frac{1}{r^6}$ with interface distance (d_z) may explain the discrepancy observed with Au electrodes. Nevertheless, additional computations are necessary to validate this.

There appears to be a significant correlation between tunneling barriers and MIGS forma-

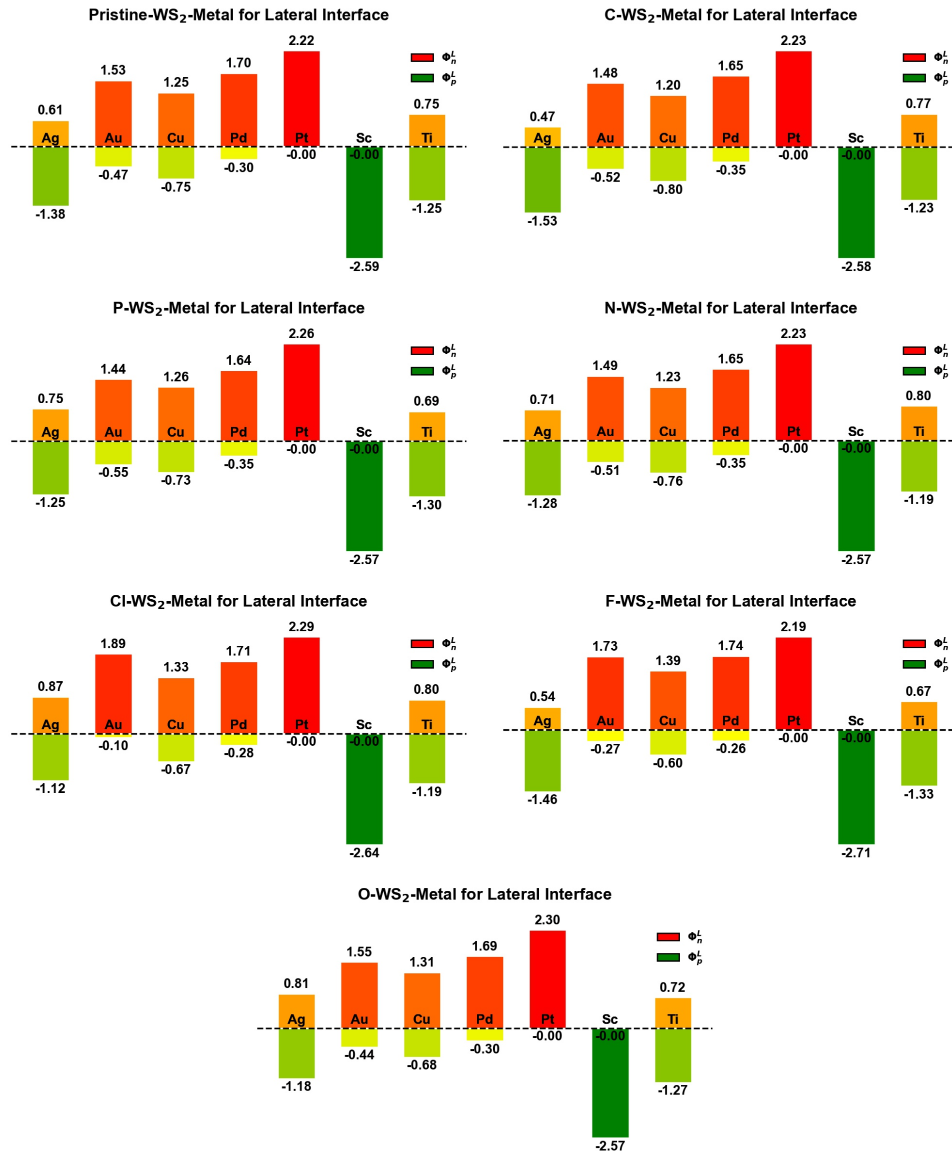

Figure 4.3: Bar graph showing the lateral Schottky barrier height (SBH) calculated using a modified Schottky-Mott model, with the vacuum level aligned between contacted WS_2 at the electrode region and WS_2 in the channel.

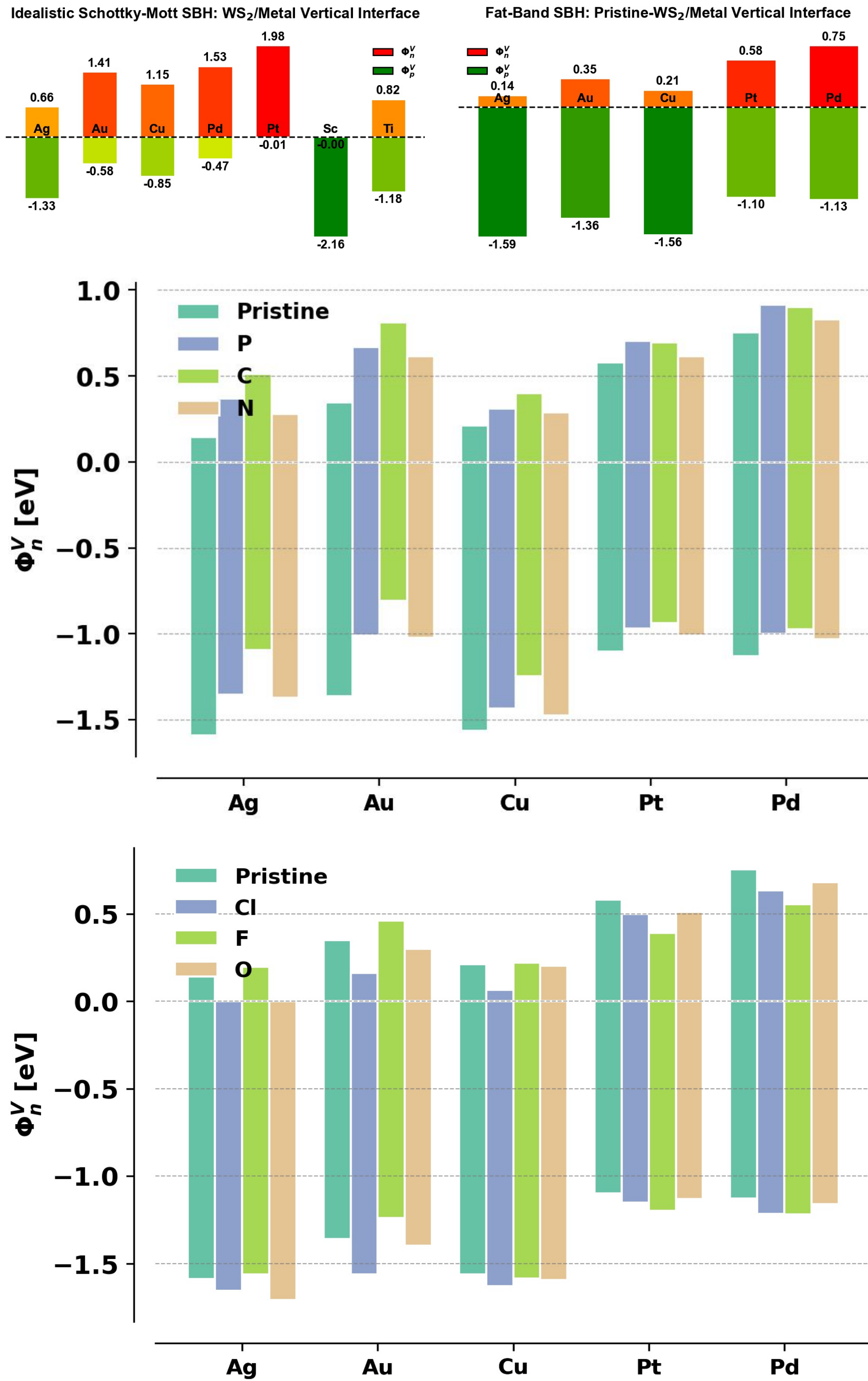

Figure 4.4: The top two plots describe the Schottky barrier height (SBH) utilizing the idealized Schottky-Mott model and the subsequent alteration due to Fermi level pinning (FLP) calculated using Fat band technique. Please note that the Fat band method could not be employed for Sc and Ti due to their highly reactive nature, which destroys the WS_2's band-edges. The bottom two plots, with the help of bar plots, compare the SBH modification across different substituted interfaces concerning the pristine WS_2/metal interface.

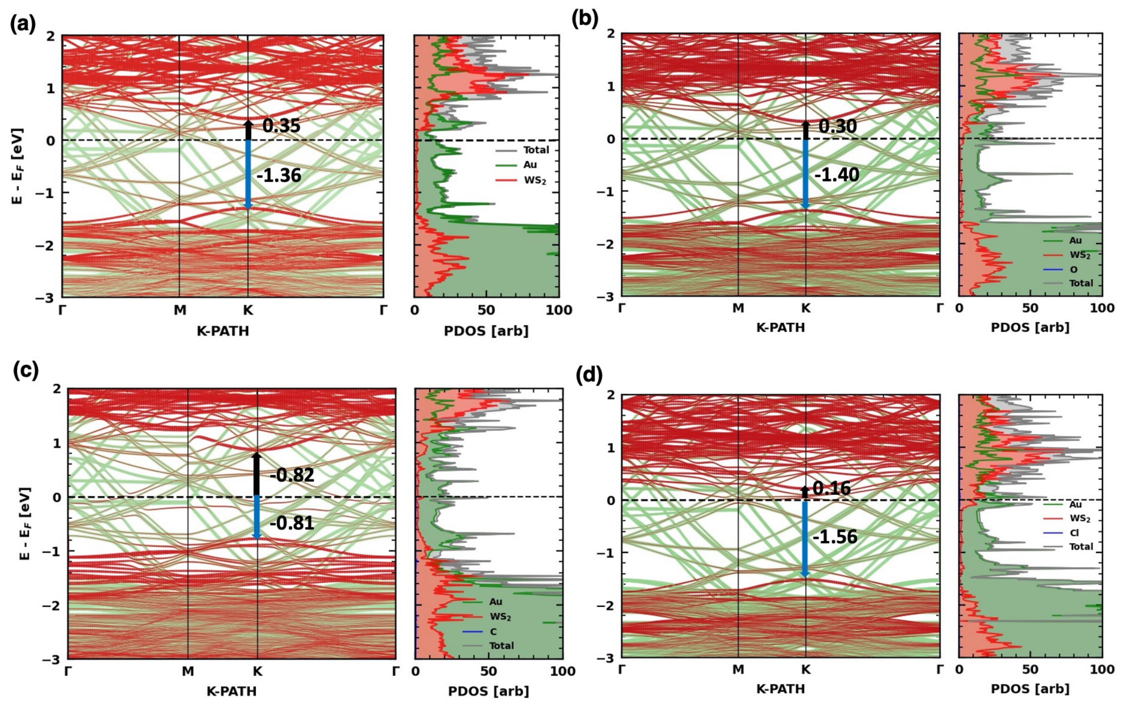

Figure 4.5: Electronic bandstructure and atom-projected DOS as applied for the fat band technique to predict the vertical SBH of Au. Black and blue-colored arrows denote the n-type and p-type SBH, which originates at the Fermi level and points to the CBM and VBM, respectively. (a) Pristine-WS_2-Au(111), (b) O-doped-WS_2-Au(111), (c) C-doped-WS_2-Au(111), (d) Cl-doped-WS_2-Au(111)

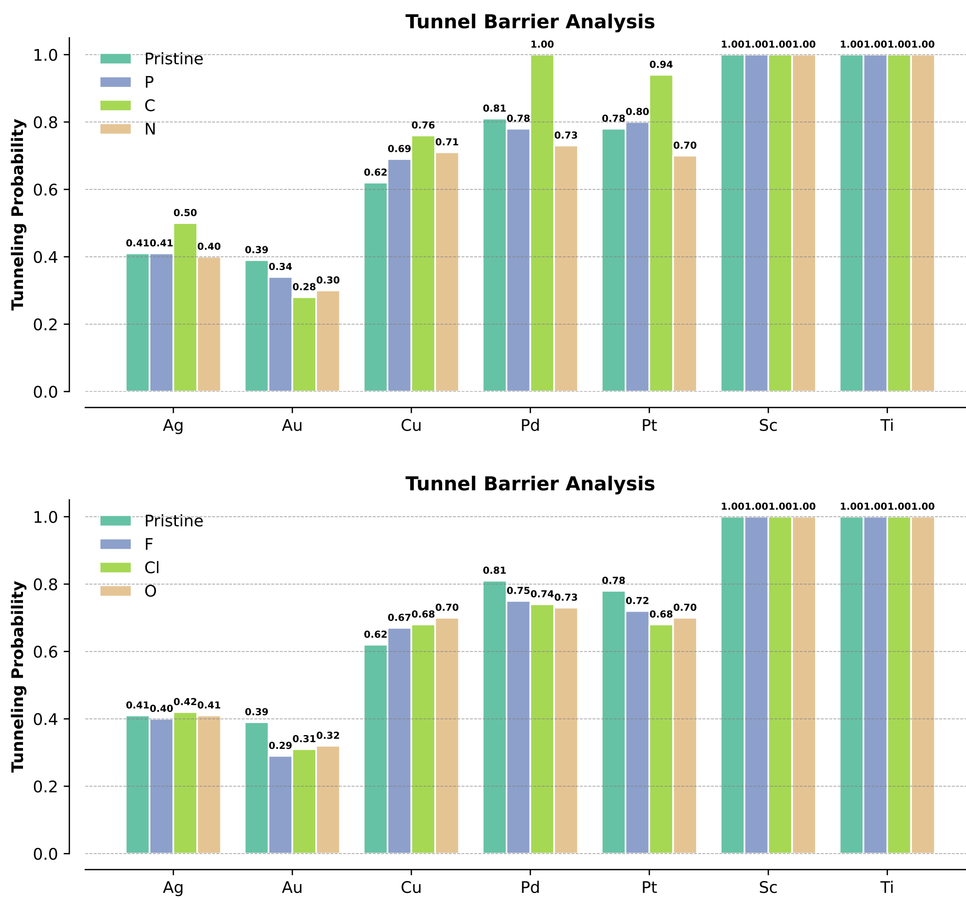

Figure 4.6: Tunneling Probability (T) analysis for all the interfaces with/without doping. T values larger than 1 imply no tunneling barrier at the interface.

tion resulting from doped-WS_2. A comprehensive explanation of the results in this section is provided in the following Section 4.2.4. Furthermore, tunneling barriers are a common issue in various engineered interface techniques, especially when a semi-metallic layer is introduced at the interface to minimize the interaction between the metal and the semiconductor, thereby reducing MIGS resulting in FLDP. However, these approaches often result in low-quality interfaces with a large tunneling width that thermally excited electrons must overcome to inject across the interface, ultimately leading to higher contact resistance. Our calculations reveal that p-type metals (C, P, N) not only reduce the hole SBH but also exhibit reduced tunnel barriers, as evident from the binding energy analysis in Fig. 4.2.1. This elucidates a crucial connection among the most significant quantities analyzed here, including binding energy, tunnel barrier, and Schottky barrier. Interestingly, we find that substitutionally doped metal-semiconductor contacts can provide FLDP (lower hole-SBH in the case of metal/TMDs contacts) without compromising the mechanical stability of the interface.

4.2.4 Metal Induced Gap States (MIGS)

Metal-induced gap states (MIGS) are the electronic states appearing in the semiconductor's band gap as a result of metal interaction. These states can either be in the vicinity of the valence band (forming acceptor-like states) or just below the conduction (originating into donor-like states). In general, the location of MIGS in the band gap is largely controlled by the specific metal and semiconductor involved. Nonetheless, in the case of TMDs, emerging MIGS tend to cause the FLP towards conduction band exhibiting donor-like states, irrespective of metal used to form the contact [126, 127]. In our calculations, we observed that in the case of Sc and Ti, the hybridization of atomic orbitals at the interface is so strong that it entirely disrupts the band edges. This makes it increasingly challenging to determine edge-dependent properties, including SBH and metal-induced gap states. For the other metal cases, we've represented MIGS in Fig. 4.7. As expected, metals with fully-occupied d-orbitals produce fewer MIGS compared to those with vacant d-orbitals. However, an important observation is the variation in MIGS with different substitutions concerning the pristine-WS_2/metal contact. Fig. 4.7 clearly shows that for p-type dopants, there is no variation in MIGS formation among all the substituted systems compared to pristine WS_2/metal contacts. This contradicts the anticipated result that the reduction of p-type SBH by Fermi level depinning (FLDP) can generally be attributed to MIGS suppression [128, 129, 130]. On the other hand, for n-type dopants, especially for F, it seems to significantly increase MIGS. However, it doesn't undergo a more severe Fermi level pinning (FLP) toward E_c to yield very low n-type SBH in similar extent with all the n-type dopants. As shown in Figure 4.4, Cl-doping leads to the highest reduction in n-type SBH, allowing Cl to be an excellent n-type polarity inducing dopant. The substantial increase in MIGS for the F-case could be attributed to the increment in the Density of States (DOS) due to unsaturated bonds, resulting from F-substitution, which enhances the electron delocalization rendering higher DOS within the band gap. This variation in MIGS behavior across different systems primarily depends on the chemical interaction linked to the metal and dopant's intrinsic characteristics at the interface, which appears to have a weak effect on FLDP in the case of dopant-substituted WS_2/metal systems, ruling out the possibility of MIGS-dependent FLDP.

Furthermore, MIGS at the metal-semiconductor (MS) interface arises from the metal wavefunction decaying into the band gap of the semiconductor due to the abrupt discontinuity of metal Block states, resulting from the translational symmetry-breaking of the metal crystals at the interface. This prevents electron transfer from the semiconductor to metal into the states around the Fermi level because the semiconductor lacks electronic states in the band gap. There-

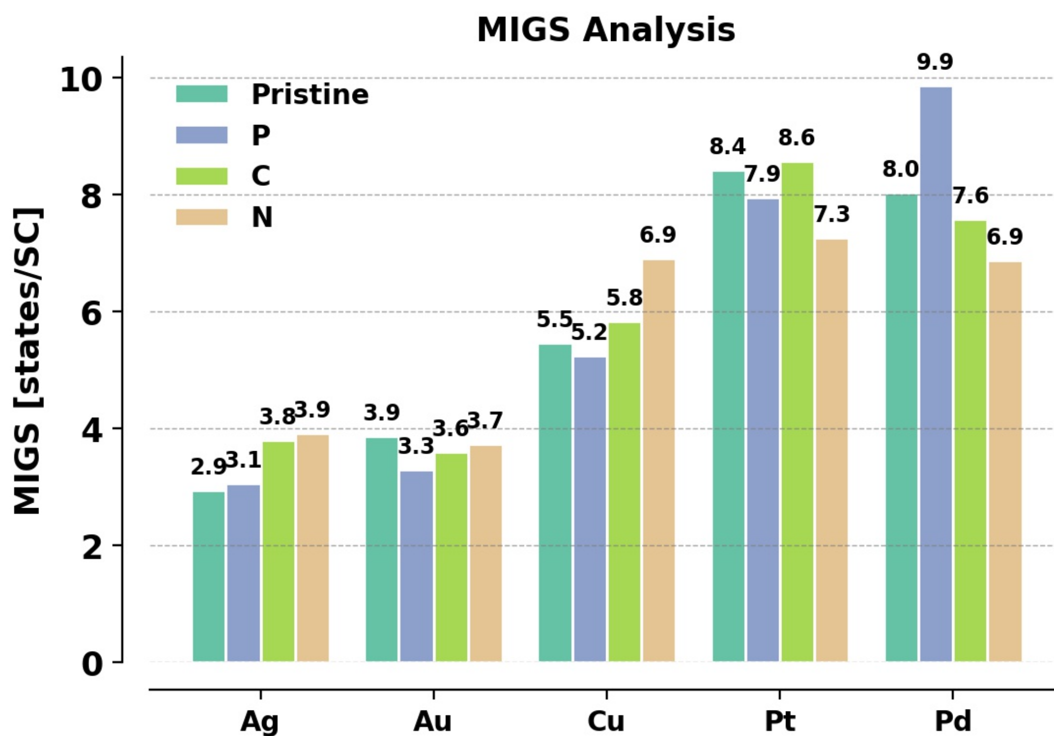

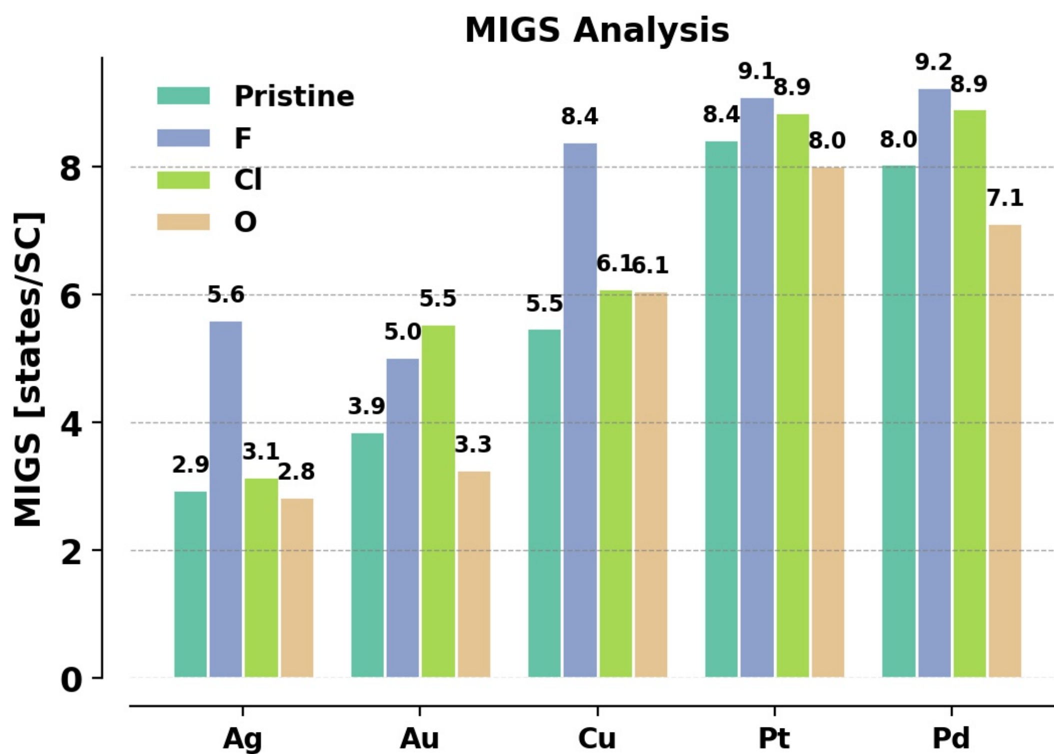

Figure 4.7: Metal-induced gap states (MIGS) calculated over all the electronic states within the band gap. We can observe variations in MIGS depending on metal and dopant chemical reactivity.

fore, it can be argued that MIGS cannot be influenced by the semiconductor side without modifying states on the metal side. We believe, this could substantiate why the Fermi level depinning (FLDP) model based on MIGS is not applicable here, leading to a weak dependence of SBH on MIGS for a given metal interfaced with different substituted WS_2. However, a change in dipole moment resulting from dopant substitution may offer a clearer explanation for the underlying mechanisms driving the FLDP phenomenon [131], as discussed in the following section. In addition, the origin of MIGS can be associated to both localization and delocalization of electrons in the vicinity of dopants at the interfaces. This can leading to the creation of charge scattering centers, which leads to increased contact resistance. However, as Fig. 4.5 illustrates, the curvature of band edges after metal contact remains largely unaffected showing that the carrier mobility of vertical interfaces will be unchanged. We attempt further to explain the above findings by conducting a charge analysis at the interface, correlating it with SBH, as shown in the upcoming section.

4.2.5 Interface Charge Analysis

Given that we are dealing with non-ideal interfaces where charge transfer is inevitable due to various crucial factors pertaing to chemical environment such as the electronegativity difference between the metal and semiconductor at the interface, the difference in work function between the metal and semiconductor, and the degree of atomic overlap at the interface, it is crucial to understand the behavior of charge transfer across the interface, particularly the charge rearrangement resulting from introducing S-substitution in WS_2. This charge rearrangement is expected to create dipoles at the interface, which in turn screens the work function difference between the metal and semiconductor, providing a rough explanation of Fermi level depinning (FLDP). To quantify the charge transfer at the interface, we calculated the charge rearrangement occurring in the WS_2 part due to S-substitution in conjunction with metal contact. This calculation is performed using the expression,

$$dQ = \int_{L_z}^{\infty} (\rho_d(z) - \rho_0(z))dz, \tag{4.2.1}$$

where $\rho_d(z)$ and $\rho_0(z)$ represent the charge density of doped and undoped systems, respectively. The lower limit (L_z) of integration is taken as the mid-point at the interface in the case of metal-contacted systems and has a value of $-\infty$ in the case of non-contacted WS_2 substitution study. The value of dQ as expected from the valence charges of substituted atoms is consistent with that obtained for WS_2-substituted cases, as illustrated in Fig. 4.9. These dQ values resulting from acceptor and donor impurities introduced into the WS_2 lattice alter its electrical properties, creating additional energy levels within the band gap. These energy levels result in a positive dQ in the case of holes (acceptor impurities) and a negative dQ in the case of excess electrons (donor impurities), leading to varying properties in different WS_2-contacted systems. The reason for $dQ = 0$ in the case of O-substitution is that it satisfies the S-bonding condition due to its being iso-electronic to S. The asymmetry in the figure indicates that only one side of WS_2 is substituted. In the case of metal contact, we made an effort to characterize further charge transfer occurring across the interface from metal contact. This charge transfer varies depending on the metals and substituted atoms, as seen in Figure 4.9. This is precisely why we observe that SBH values for p-type dopants (C, P, N) are not the same as in the WS_2-doped study because there is a non-vanishing finite charge redistribution taking place upon metal contacts. This subsequently weakens their ability to provide us with a p-type contact by capturing the carriers in the MIGS emerging around the conduction band. In the cases of Ag, Au, and Cu, we can see

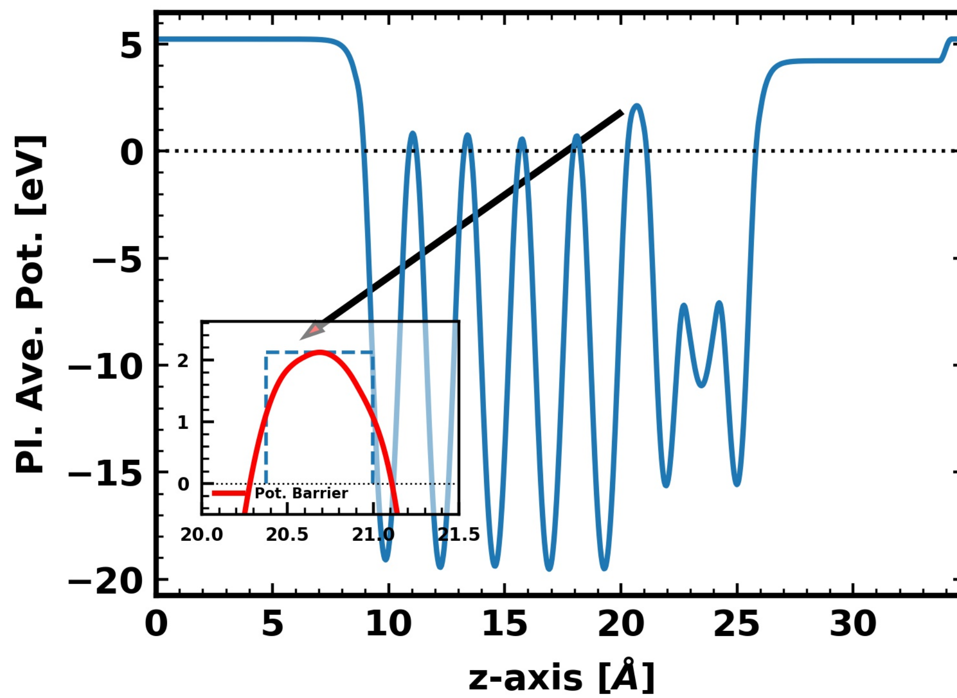

Figure 4.8: Planar-averaged electrostatic potential along the interface in the z-direction. The red dotted line represents the Fermi level. The dashed circular portion, which has been zoomed in on the right, is approximated as a rectangular shape to facilitate the application of quantum mechanical tunneling theory.

dQ values departing from the original WS_2-substitution case, which reduces p-type SBH to a certain degree but does not entirely change the polarity from n-type to p-type.

Interestingly, the amount of dQ generally aligns with the varying trends in vertical SBH modification for the substitutionally doped contact systems. However, it does not show a strict correlation with the observed SBH values. One reason for this discrepancy could be the fact that DFT calculations may not provide accurate on-site charges for strongly correlated systems, such as transition metals with partially filled *d*-orbitals [132]. DFT is known to have limitations in accurately describing the localization of electronic charges, referred to as self-interaction error. To account for proper electronic interactions and, hence, accurate charge transfer in such strongly correlated electronic systems, Hubbard U-corrected DFT+U calculations could be employed [133], which are known to describe on-site electron-electron interactions more accurately than semi-local exchange-correlation functionals based on the Perdew-Burke-Ernzerhof (PBE) generalized gradient approximation (GGA). However, calculating optimized U-values for various systems with hundreds of atoms is beyond the scope of this study. It's also important to note that this study is limited to a fixed doping concentration, which is reasonable to believe could have ultimately led to p-type contacts with a higher concentration of acceptor impurities resulting from more extensive p-type doping. Furthermore, the presence of additional energy states within the band gap of a semiconductor, as indicated by the dQ values result in a higher value of MIGS in the case of F and Cl compared to the pristine contact case. However, for C, P, and N cases, there is no systematic reduction across different systems, although a slight increase in MIGS is observed. This indicates that in the case of p-type dopants, FLDP is not solely dependent on MIGS.

The idealistic Schottky-Mott model fails to explain the SBH due to charge redistribution - an electric dipole is formed across the interface. This dipole results in the Fermi level of the semiconductor-metal contact being pinned within the band gap rather than adjusting to the metal's Fermi level. Therefore, we anticipate that Fermi level depinning (FLDP) leading to reduction of p-type Schottky barrier height can be explained from the change in the interface dipole moment (ΔP) resulting from dopant substitution (C, P, N). The ΔP can be calculated as follows:

$$\Delta P = \int_{Z_i}^{Z_f} z\Delta\rho(z)dz \tag{4.2.2}$$

where Z_i and Z_f represent the initial and final z-locations involving finite charge variation ($\Delta\rho$). As shown in Figure 4.10, C, P, and N exhibit the highest negative ΔP values, while it is positive for F and Cl, with the highest value observed for Cl. The variation is minimal for O, which are generally in line with FLDP and the previously determined dQ values.

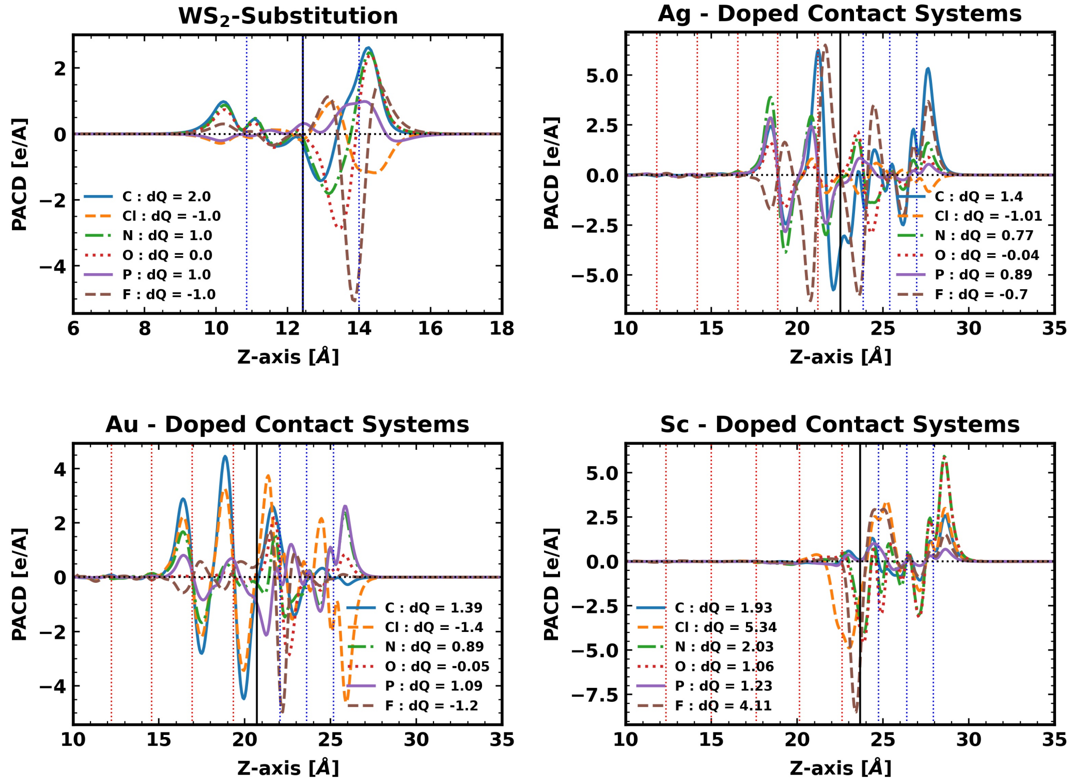

Figure 4.9: Planar average charge density (PACD) due to doping compared to the pristine contact. The dQ-values indicate the amount of charge transferred towards the WS_2 side upon substitution. The solid black line represents the interface midpoint, while the red/blue dotted lines indicate the locations of metal/WS_2 atomic planes along the z-direction.

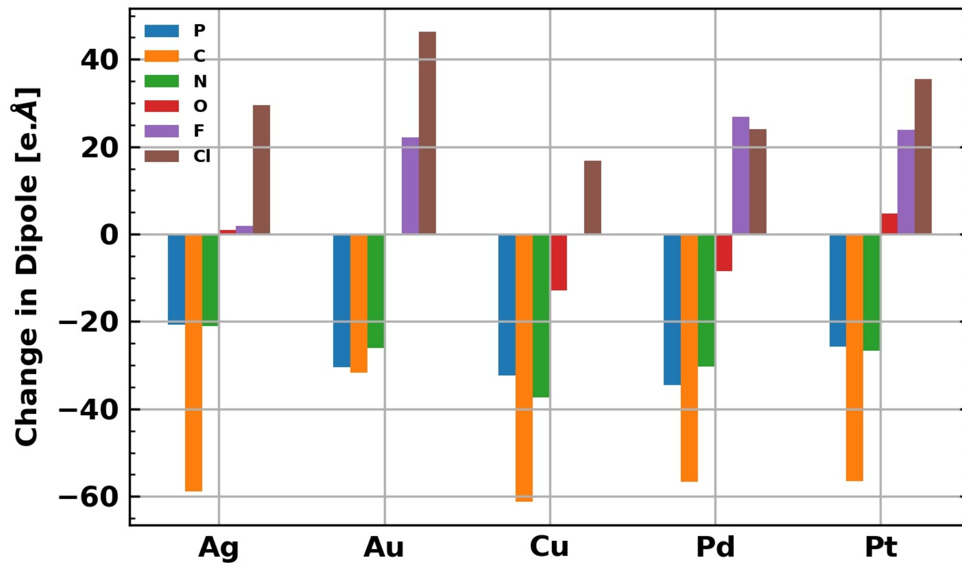

Figure 4.10: Change in the interface dipole moment (ΔP) due to doping. The trend in dipole change consistently correlates with the Fat band Schottky barrier heights.

Chapter 5

Summary

5.1 Conclusion

In conclusion, our study successfully modeled various metal-semiconductor interfaces using state-of-the-art computational tools. We conducted a comprehensive analysis of both the mechanical and electrical properties of metal-phosphorene and metal/WS_2 contacts, to elucidate the key factors contributing to parasitic contact resistance in 2D-semiconductor/metal interfaces, a critical aspect for their potential use in next-generation electronic devices. This work covered various facets of these interfaces, including the feasibility of stable interface formation with different commonly used metal electrodes. We also explored the electronic properties that contribute to the overall contact resistance, encompassing Schottky barrier height (SBH), tunneling barrier heights (TBH), metal-induced gap states (MIGS), and variations in interface charge density. It's important to note that phosphorene and transition metal dichalcogenides (TMDs) belong to two distinct classes of highly sought-after 2D semiconductors, each offering unique electronic properties. Phosphorene, for instance, is a monolayer 2D semiconductor composed of phosphorus (P) atoms, featuring a band gap ranging from 0.3 eV to 2.0 eV and a high carrier mobility of over ~1000 cm^2/Vs. These characteristics make it a compelling candidate for high-speed transistors. On the other hand, WS_2 is a primitive crystal composed of tungsten (W) and sulfur (S), boasting a band gap of 1.8-2.5 eV and a carrier mobility of up to ~200 cm^2/Vs, positioning it as a suitable choice for ultra-small and low-power transistors. Furthermore, our study demonstrated that distinct interface properties emerge due to the unique characteristics of phosphorene and WS_2. Notably, we investigated important properties such as electron affinity (χ_{SC}), ionization potential (I_{SC}), and electronegativity of interface atoms. For instance, we observed the formation of Ohmic contacts in the case of phosphorene-metal interfaces with all the metals, primarily due to the metallization of phosphorene upon metal contacts. Conversely, with WS_2, Schottky barriers form except in the case of Sc and Ti, where Ohmic behavior is observed for direct metal-semiconductor interfaces. Moreover, we found that none of the interfaces adhered to the idealistic Schottky-Mott model; instead, they tended to form pinned interfaces. This pinning effect is found to be attributed to the surface dipole formation resulting from finite charge rearrangement at the interface. This observation underscores the complexity of metal-electrode selection, emphasizing that relying solely on work function for decision-making may not yield the desired interface properties.

In the following paragraphs, we have summarized the outcome of this work separately specific to phosphorene and WS_2. Our investigation into the phosphorene involved several key findings as explained below:

- 1. Adhesion Strength: We employed work of separation calculations to gauge the adhesion strength / binding strength of the metal interfaces. This approach allowed us to classify metals into two types: type 1 metals with lower adhesion, indicating a weaker bond with phosphorene, and type 2 metals with higher adhesion, implying a stronger bond. Type 1 metals consist of Ag, Al, Au, Cu, and Zn, while Mo, Pd, W, Co, Ni, Pt, Nb, Sc, Ru, Ta, Ti, Cr, and V.
- 2. Metallization of phosphorene: Through density of state analysis, we observed that all metals led to the metallization of the contacted phosphorene, thereby providing us with Ohmic contacts.
- 3. Electrical Behavior Analysis: In the context of carrier flow from contacts to phosphorene, we considered two interfaces: vertical interface (direct contact between metal and phosphorene) and lateral interface (between the contact portion and pristine phosphorene in the FET channel). Calculation of both the tunnel barrier height (TBH) and Schottky barrier height (SBH) play pivotal roles in determining overall contact resistance. Our analysis highlights the necessity of a combined analysis of both parameters to comprehend the electrical behavior of the contacts.
- 4. Mid-Interface Charge Density: We found that mid-interface charge density calculations served as a valuable tool for predicting the mechanical and electrical properties of the contacts.
- 5. Based on our analysis, it was determined that type 1 metals exhibit not only lower adhesion but also poorer electrical performance. Conversely, type 2 metals demonstrated a stronger bond and excellent electrical properties. However, there was an exception to this observation, as type 2 metals such as Mo, Nb, Ta, and W exhibited poor electrical performance due to broken interlayer P−P bonds.

In our investigation of WS_2/metal interfaces, we conducted the study in two distinct phases. Initially, we focused on the pristine-WS_2/metal interface, and subsequently, we explored the S-substituted-WS_2/metal interface with various dopants, including C, Cl, F, P, N, and O. This systematic exploration carries substantial implications for improving the contact properties of transistors based on transition metal dichalcogenides (TMDs), especially those utilizing WS_2. It provides valuable insights into the distinctive doping characteristics associated with these dopants within WS_2-based contact interfaces.

Following are the summarized key findings:

- Positive binding strength of interfaces offers the possibility of mechanically stable interfaces for all the metal electrodes.
- A consistently high correlation has been observed between binding strength and the interface separation.
- Vertical SBH calculation reveals that all interfaces lead to n-type contact polarity due to MIGS formation.
- Dopants like P, C, and N contribute to lower p-type Schottky barrier heights (SBH) by enabling Fermi level depinning (FLDP). We found that C-doping is the most promising mechanism for WS_2/metal interfaces as it not only leads to the most significant p-type

SBH reduction but also shows considerably improved interface adhesion strength, thereby reducing the tunneling barrier. On the other hand, Cl, due to its donor-inducing property leads to the highest improvement in the n-type SBH.

- The FLDP exhibits a weak dependence on metal-induced gap states (MIGS), allowing for FLDP alongside mechanically stable interfaces and reduced tunneling barriers across all the metallic electrodes.
- This observation contrasts with other interface passivation techniques, which often suffer from issues such as low-quality interfaces and increased tunneling resistance due to extended interface distances.
- Furthermore, our study underscores the intricate interplay among various interface properties, including binding energy, charge density, MIGS, SBH, and TBH.

To summarize, this work addresses different key aspects responsible for contact resistance, by computationally modeling different metal-semiconductor interfaces with two different widely studied 2D-semiconductors, phosphorene and WS_2. The research findings hold the promise of providing critical insights into the MS interfaces to guide further experiments. The results can be used to compare and downselect the appropriate metal electrodes to fabricate the more energy-efficient electronic/optoelectric devices by focusing on the specific properties contributing to the contact resistance.

Bibliography

[66] S. Smidstrup, T. Markussen, and . Pieter Vancraeyveld, "QuantumATK: an integrated platform of electronic and atomic-scale modelling tools," *Journal of Physics: Condensed Matter*, vol. 32, no. 1, p. 015901, oct 2019. [Online]. Available: https://doi.org/10.1088%2F1361-648x%2Fab4007

[92] A. Ghaffar, M. D. Ganeriwala, K. Hongo, R. Maezono, and N. R. Mohapatra, "Insights into the mechanical and electrical properties of a metal–phosphorene interface: An ab initio study with a wide range of metals," *ACS omega*, vol. 6, no. 11, pp. 7795–7803, 2021. [Online]. Available: https://doi.org/10.1021/acsomega.0c06255

[1] N. Marzari, A. Ferretti, and C. Wolverton, "Electronic-structure methods for materials design," *Nature Materials*, vol. 20, no. 6, pp. 736–749, may 2021. [Online]. Available: https://doi.org/10.1038%2Fs41563-021-01013-3

[2] P. Makkar and N. N. Ghosh, "A review on the use of DFT for the prediction of the properties of nanomaterials," *RSC Advances*, vol. 11, no. 45, pp. 27 897–27 924, 2021. [Online]. Available: https://doi.org/10.1039%2Fd1ra04876g

[3] F. Oba and Y. Kumagai, "Design and exploration of semiconductors from first principles: A review of recent advances," *Applied Physics Express*, vol. 11, no. 6, p. 060101, may 2018. [Online]. Available: https://doi.org/10.7567%2Fapex.11.060101

[4] C. Freysoldt, B. Grabowski, T. Hickel, J. Neugebauer, G. Kresse, A. Janotti, and C. G. V. de Walle, "First-principles calculations for point defects in solids," *Reviews of Modern Physics*, vol. 86, no. 1, pp. 253–305, mar 2014. [Online]. Available: https://doi.org/10.1103%2Frevmodphys.86.253

[5] A. K. Geim and K. S. Novoselov, "The rise of graphene," *Nature materials*, vol. 6, no. 3, p. 183, 2007.

[6] Y. P. Venkata Subbaiah, K. J. Saji, and A. Tiwari, "Atomically thin MoS_2: A versatile nongraphene 2d material," *Advanced Functional Meterials*, vol. 26, no. 13, p. 2046, 2016.

[7] H. Wang, L. Yu, Y.-H. Lee, Y. Shi, A. Hsu, M. L. Chin, L.-J. Li, M. Dubey, J. Kong, and T. Palacios, "High-frequency, scaled graphene transistors on diamond-like carbon," *Nature*, vol. 472, no. 7341, p. 74, 2011.

[8] L. Liao, Y.-C. Lin, M. Bao, R. Cheng, J. Bai, Y. Liu, Y. Qu, K. L. Wang, Y. Huang, and X. Duan, "Integrated circuits based on bilayer MoS_2 transistors," *Nano Letters*, vol. 12, no. 9, p. 4674, 2012.

[9] W. Cao, J. Kang, D. Sarkar, W. Liu, and K. Banerjee, "2d semiconductor fets - projections and design for sub-10 nm vlsi," *IEEE Transactions on Electron Devices*, vol. 62, no. 11, p. 3459, 2015.

[10] IRDS. (2022) IRDS™ 2022 Beyond CMOS and Emerging Research Materials. [Online; accessed 19-10-2023]. [Online]. Available: https://irds.ieee.org/editions/2022/irds%E2%84%A2-2022-beyond-cmos-and-emerging-research-materials

[11] G. E. Moore *et al.*, "Progress in digital integrated electronics," in *Electron devices meeting*, vol. 21. Washington, DC, 1975, pp. 11–13.

[12] D. Roy, P. Pal, T. Pal, and R.-A. Doong, "Advancement in phosphorene: Synthesis, properties, and applications," *Applied Materials Today*, vol. 35, p. 101944, dec 2023. [Online]. Available: https://doi.org/10.1016%2Fj.apmt.2023.101944

[13] X. Ling, H. Wang, S. Huang, F. Xia, and M. S. Dresselhaus, "The renaissance of black phosphorus," *Proceedings of the National Academy of Sciences*, vol. 112, no. 15, pp. 4523–4530, mar 2015. [Online]. Available: https://doi.org/10.1073%2Fpnas.1416581112

[14] G.-S. Kim, S.-H. Kim, J. Park, K. H. Han, J. Kim, and H.-Y. Yu, "Schottky barrier height engineering for electrical contacts of multilayered mos_2 transistors with reduction of metal-induced gap states," *ACS Nano*, vol. 12, no. 6, pp. 6292–6300, may 2018. [Online]. Available: https://doi.org/10.1021%2Facsnano.8b03331

[15] H.-L. Tang, M.-H. Chiu, C.-C. Tseng, S.-H. Yang, K.-J. Hou, S.-Y. Wei, J.-K. Huang, Y.-F. Lin, C.-H. Lien, and L.-J. Li, "Multilayer graphene-wse_2 heterostructures for wse_2 transistors," *ACS Nano*, vol. 11, no. 12, pp. 12 817–12 823, dec 2017. [Online]. Available: https://doi.org/10.1021%2Facsnano.7b07755

[16] A. Avsar, K. Marinov, E. G. Marin, G. Iannaccone, K. Watanabe, T. Taniguchi, G. Fiori, and A. Kis, "Reconfigurable diodes based on vertical WSe_2 transistors with van der waals bonded contacts," *Advanced Materials*, vol. 30, no. 18, mar 2018. [Online]. Available: https://doi.org/10.1002%2Fadma.201707200

[17] Y. Pan, Y. Wang, M. Ye, R. Quhe, H. Zhong, Z. Song, X. Peng, D. Yu, J. Yang, J. Shi *et al.*, "Monolayer phosphorene–metal contacts," *Chemistry of Materials*, vol. 28, no. 7, pp. 2100–2109, 2016.

[18] A. Maity and P. Sen, "Density functional study of metal–phosphorene interfaces," *International Journal of Modern Physics B*, vol. 31, no. 11, p. 1750077, 2017.

[19] A. Chanana and S. Mahapatra, "First principles study of metal contacts to monolayer black phosphorous," *Journal of Applied Physics*, vol. 116, no. 20, p. 204302, 2014.

[20] K. Wang, L. Zhang, G. D. Nguyen, X. Sang, C. Liu, Y. Yu, W. Ko, R. R. Unocic, A. A. Puretzky, C. M. Rouleau, D. B. Geohegan, L. Fu, G. Duscher, A.-P. Li, M. Yoon, and K. Xiao, "Selective antisite defect formation in ws_2 monolayers via reactive growth on dilute w-au alloy substrates," *Advanced Materials*, vol. 34, no. 3, p. 2106674, nov 2021. [Online]. Available: https://doi.org/10.1002%2Fadma.202106674

[21] J. Hong, Z. Hu, M. Probert, K. Li, D. Lv, X. Yang, L. Gu, N. Mao, Q. Feng, L. Xie, J. Zhang, D. Wu, Z. Zhang, C. Jin, W. Ji, X. Zhang, J. Yuan, and Z. Zhang, "Exploring atomic defects in molybdenum disulphide monolayers," *Nature Communications*, vol. 6, no. 1, feb 2015. [Online]. Available: https://doi.org/10.1038%2Fncomms7293

[22] J. Lee, M. J. Kim, B. G. Jeong, C. Kwon, Y. Cha, S. H. Choi, K. K. Kim, and M. S. Jeong, "Electrical role of sulfur vacancies in MoS2: Transient current approach," *Applied Surface Science*, vol. 613, p. 155900, mar 2023. [Online]. Available: https://doi.org/10.1016%2Fj.apsusc.2022.155900

[23] S. M. Gali, A. Pershin, A. Lherbier, J.-C. Charlier, and D. Beljonne, "Electronic and transport properties in defective mos_2: Impact of sulfur vacancies," *The Journal of Physical Chemistry C*, vol. 124, no. 28, pp. 15 076–15 084, jun 2020. [Online]. Available: https://doi.org/10.1021%2Facs.jpcc.0c04203

[24] H. Cho, M. Sritharan, Y. Ju, P. Pujar, R. Dutta, W.-S. Jang, Y.-M. Kim, S. Hong, Y. Yoon, and S. Kim, "Se-vacancy healing with substitutional oxygen in wse_2 for high-mobility p-type field-effect transistors," *ACS Nano*, may 2023. [Online]. Available: https://doi.org/10.1021%2Facsnano.2c11567

[25] Y. Zhao, K. Xu, F. Pan, C. Zhou, F. Zhou, and Y. Chai, "Doping, contact and interface engineering of two-dimensional layered transition metal dichalcogenides transistors," *Advanced Functional Materials*, vol. 27, no. 19, p. 1603484, dec 2016. [Online]. Available: https://doi.org/10.1002%2Fadfm.201603484

[26] J. Jiang, Q. Zhang, A. Wang, Y. Zhang, F. Meng, C. Zhang, X. Feng, Y. Feng, L. Gu, H. Liu, and L. Han, "A facile and effective method for patching sulfur vacancies of ws_2 via nitrogen plasma treatment," *Small*, vol. 15, no. 36, p. 1901791, jun 2019. [Online]. Available: https://doi.org/10.1002%2Fsmll.201901791

[27] Y.-C. Lin, B. Jariwala, B. M. Bersch, K. Xu, Y. Nie, B. Wang, S. M. Eichfeld, X. Zhang, T. H. Choudhury, Y. Pan, R. Addou, C. M. Smyth, J. Li, K. Zhang, M. A. Haque, S. Fölsch, R. M. Feenstra, R. M. Wallace, K. Cho, S. K. Fullerton-Shirey, J. M. Redwing, and J. A. Robinson, "Realizing large-scale, electronic-grade two-dimensional semiconductors," *ACS Nano*, vol. 12, no. 2, pp. 965–975, jan 2018. [Online]. Available: https://doi.org/10.1021%2Facsnano.7b07059

[28] M. Wurdack, T. Yun, E. Estrecho, N. Syed, S. Bhattacharyya, M. Pieczarka, A. Zavabeti, S.-Y. Chen, B. Haas, J. Müller, M. N. Lockrey, Q. Bao, C. Schneider, Y. Lu, M. S. Fuhrer, A. G. Truscott, T. Daeneke, and E. A. Ostrovskaya, "Ultrathin ga_2o_3 glass: A large-scale passivation and protection material for monolayer ws_2," *Advanced Materials*, vol. 33, no. 3, p. 2005732, dec 2020. [Online]. Available: https://doi.org/10.1002%2Fadma.202005732

[29] Q. Cui, Z. Luo, Q. Cui, W. Zhu, H. Shou, C. Wu, Z. Liu, Y. Lin, P. Zhang, S. Wei, H. Yang, S. Chen, A. Pan, and L. Song, "Robust and high photoluminescence in ws_2 monolayer through in situ defect engineering," *Advanced Functional Materials*, vol. 31, no. 38, p. 2105339, jul 2021. [Online]. Available: https://doi.org/10.1002%2Fadfm.202105339

[30] Z. Yu, Y. Pan, Y. Shen, Z. Wang, Z.-Y. Ong, T. Xu, R. Xin, L. Pan, B. Wang, L. Sun, J. Wang, G. Zhang, Y. W. Zhang, Y. Shi, and X. Wang, "Towards intrinsic charge transport in monolayer molybdenum disulfide by defect and interface engineering," *Nature Communications*, vol. 5, no. 1, oct 2014. [Online]. Available: https://doi.org/10.1038%2Fncomms6290

[31] J. H. Park, A. Sanne, Y. Guo, M. Amani, K. Zhang, H. C. P. Movva, J. A. Robinson, A. Javey, J. Robertson, S. K. Banerjee, and A. C. Kummel, "Defect passivation of transition metal dichalcogenides via a charge transfer van der waals interface," *Science Advances*, vol. 3, no. 10, oct 2017. [Online]. Available: https://doi.org/10.1126%2Fsciadv.1701661

[32] Y. J. Zheng, Y. Chen, Y. L. Huang, P. K. Gogoi, M.-Y. Li, L.-J. Li, P. E. Trevisanutto, Q. Wang, S. J. Pennycook, A. T. S. Wee, and S. Y. Quek, "Point defects and localized excitons in 2d wse_2," *ACS Nano*, vol. 13, no. 5, pp. 6050–6059, may 2019. [Online]. Available: https://doi.org/10.1021%2Facsnano.9b02316

[33] M. Koperski, K. Nogajewski, A. Arora, V. Cherkez, P. Mallet, J.-Y. Veuillen, J. Marcus, P. Kossacki, and M. Potemski, "Single photon emitters in exfoliated WSe2 structures," *Nature Nanotechnology*, vol. 10, no. 6, pp. 503–506, may 2015. [Online]. Available: https://doi.org/10.1038%2Fnnano.2015.67

[34] M. Mahjouri-Samani, L. Liang, A. Oyedele, Y.-S. Kim, M. Tian, N. Cross, K. Wang, M.-W. Lin, A. Boulesbaa, C. M. Rouleau, A. A. Puretzky, K. Xiao, M. Yoon, G. Eres, G. Duscher, B. G. Sumpter, and D. B. Geohegan, "Tailoring vacancies far beyond intrinsic levels changes the carrier type and optical response in monolayer $mose_2$ crystals," *Nano Letters*, vol. 16, no. 8, pp. 5213–5220, jul 2016. [Online]. Available: https://doi.org/10.1021%2Facs.nanolett.6b02263

[35] Y. Kim, H. Bark, B. Kang, and C. Lee, "Wafer-scale substitutional doping of monolayer mos_2 films for high-performance optoelectronic devices," *ACS Applied Materials & Interfaces*, vol. 11, no. 13, pp. 12 613–12 621, mar 2019. [Online]. Available: https://doi.org/10.1021%2Facsami.8b20714

[36] H. Gao, J. Suh, M. C. Cao, A. Y. Joe, F. Mujid, K.-H. Lee, S. Xie, P. Poddar, J.-U. Lee, K. Kang, P. Kim, D. A. Muller, and J. Park, "Tuning electrical conductance of mos_2 monolayers through substitutional doping," *Nano Letters*, vol. 20, no. 6, pp. 4095–4101, may 2020. [Online]. Available: https://doi.org/10.1021%2Facs.nanolett.9b05247

[37] F. Zhang, Y. Lu, D. S. Schulman, T. Zhang, K. Fujisawa, Z. Lin, Y. Lei, A. L. Elias, S. Das, S. B. Sinnott, and M. Terrones, "Carbon doping of ws_2 monolayers: Bandgap reduction and p-type doping transport," *Science Advances*, vol. 5, no. 5, may 2019. [Online]. Available: https://doi.org/10.1126%2Fsciadv.aav5003

[38] H. M. W. Khalil, M. F. Khan, J. Eom, and H. Noh, "Highly stable and tunable chemical doping of multilayer ws_2 field effect transistor: Reduction in contact resistance," *ACS Applied Materials & Interfaces*, vol. 7, no. 42, pp. 23 589–23 596, oct 2015. [Online]. Available: https://doi.org/10.1021%2Facsami.5b06825

[39] B. Tang, Z. G. Yu, L. Huang, J. Chai, S. L. Wong, J. Deng, W. Yang, H. Gong, S. Wang, K.-W. Ang, Y.-W. Zhang, and D. Chi, "Direct n- to p-type channel

conversion in monolayer/few-layer ws_2 field-effect transistors by atomic nitrogen treatment," *ACS Nano*, vol. 12, no. 3, pp. 2506–2513, mar 2018. [Online]. Available: https://doi.org/10.1021%2Facsnano.7b08261

[40] F. Zhang, Y. Lu, D. S. Schulman, T. Zhang, K. Fujisawa, Z. Lin, Y. Lei, A. L. Elias, S. Das, S. B. Sinnott, and M. Terrones, "Carbon doping of ws_2 monolayers: Bandgap reduction and p-type doping transport," *Science Advances*, vol. 5, no. 5, may 2019. [Online]. Available: https://doi.org/10.1126%2Fsciadv.aav5003

[41] T. Kim, Y. Kim, and E. K. Kim, "Characteristics of cl-doped MoS2 field-effect transistors," *Sensors and Actuators A: Physical*, vol. 312, p. 112165, sep 2020. [Online]. Available: https://doi.org/10.1016%2Fj.sna.2020.112165

[42] S. Wu, Y. Zeng, X. Zeng, S. Wang, Y. Hu, W. Wang, S. Yin, G. Zhou, W. Jin, T. Ren, Z. Guo, and J. Lu, "High-performance p-type mos_2 field-effect transistor by toroidal-magnetic-field controlled oxygen plasma doping," *2D Materials*, vol. 6, no. 2, p. 025007, jan 2019. [Online]. Available: https://doi.org/10.1088%2F2053-1583%2Faafe2d

[43] M. Esfandiari, S. Kamaei, M. Rajabali, and S. Mohajerzadeh, "High-performance large-area ws_2-based transistors by a novel tin-oxide assisted liquid-phase exfoliation: doping adjustment by plasma treatment," *2D Materials*, vol. 8, no. 2, p. 025013, jan 2021. [Online]. Available: https://doi.org/10.1088%2F2053-1583%2Fabd6b2

[44] J. Jiang, P. Yang, J. J. Liou, W. Liao, and Y. Chai, "Defect engineering of two-dimensional materials towards next-generation electronics and optoelectronics," *Nano Research*, vol. 16, no. 2, pp. 3104–3124, nov 2022. [Online]. Available: https://doi.org/10.1007%2Fs12274-022-5016-9

[45] B. Kirubasankar, Y. S. Won, L. A. Adofo, S. H. Choi, S. M. Kim, and K. K. Kim, "Atomic and structural modifications of two-dimensional transition metal dichalcogenides for various advanced applications," *Chemical Science*, vol. 13, no. 26, pp. 7707–7738, 2022. [Online]. Available: https://doi.org/10.1039%2Fd2sc01398c

[46] H. Li, S. Huang, Q. Zhang, Z. Zhu, C. Li, J. Meng, and Y. Tian, "Nonmetal doping induced electronic and magnetic properties in mose2 monolayer," *Chemical Physics Letters*, vol. 692, pp. 69–74, 2018. [Online]. Available: https://doi.org/10.1016/j.cplett.2017.12.010

[47] J. Kim, G. H. An, S. Bang, D. G. Park, D. Kim, S. Jin, M. J. Kim, H. S. Lee, and J. W. Lee, "Comparative analysis of schottky barriers for heterogeneous defect domains in monolayer ws_2 field-effect transistors," *Applied Surface Science*, vol. 604, p. 154600, 2022. [Online]. Available: https://doi.org/10.1016/j.apsusc.2022.154600

[48] H. Y. Jeong, Y. Jin, S. J. Yun, J. Zhao, J. Baik, D. H. Keum, H. S. Lee, and Y. H. Lee, "Heterogeneous defect domains in single-crystalline hexagonal ws_2," *Advanced Materials*, vol. 29, no. 15, p. 1605043, feb 2017. [Online]. Available: https://doi.org/10.1002%2Fadma.201605043

[49] J. Wang, J. Liu, B. Zhang, X. Ji, K. Xu, C. Chen, L. Miao, and J. Jiang, "The mechanism of hydrogen adsorption on transition metal dichalcogenides as hydrogen evolution reaction catalyst," *Physical Chemistry Chemical Physics*, vol. 19, no. 15, pp. 10 125–10 132, 2017. [Online]. Available: https://doi.org/10.1039/C7CP00636E

[50] F. Withers, T. H. Bointon, M. Dubois, S. Russo, and M. F. Craciun, “Nanopatterning of fluorinated graphene by electron beam irradiation,” *Nano Letters*, vol. 11, no. 9, pp. 3912–3916, aug 2011. [Online]. Available: https://doi.org/10.1021%2Fnl2020697

[51] X. Liu, D. Qu, Y. Yuan, J. Sun, and W. J. Yoo, “Self-terminated surface monolayer oxidation induced robust degenerate doping in mote$_2$ for low contact resistance,” *ACS Applied Materials & Interfaces*, vol. 12, no. 23, pp. 26 586–26 592, may 2020. [Online]. Available: https://doi.org/10.1021%2Facsami.0c03762

[52] L. Yang, K. Majumdar, H. Liu, Y. Du, H. Wu, M. Hatzistergos, P. Y. Hung, R. Tieckelmann, W. Tsai, C. Hobbs, and P. D. Ye, “Chloride molecular doping technique on 2d materials: Ws$_2$ and mos$_2$,” *Nano Letters*, vol. 14, no. 11, pp. 6275–6280, oct 2014. [Online]. Available: https://doi.org/10.1021%2Fnl502603d

[53] A. Chanana and S. Mahapatra, “Density functional theory based study of chlorine doped ws$_2$-metal interface,” *Applied Physics Letters*, vol. 108, no. 10, p. 103107, mar 2016. [Online]. Available: https://doi.org/10.1063%2F1.4943267

[54] S. Prucnal, A. Hashemi, M. Ghorbani-Asl, R. Hübner, J. Duan, Y. Wei, D. Sharma, D. R. T. Zahn, R. Ziegenrücker, U. Kentsch, A. V. Krasheninnikov, M. Helm, and S. Zhou, “Chlorine doping of mose$_2$ flakes by ion implantation,” *Nanoscale*, vol. 13, no. 11, pp. 5834–5846, 2021. [Online]. Available: https://doi.org/10.1039%2Fd0nr08935d

[55] M. Born and W. Heisenberg, “Zur quantentheorie der molekeln,” *Original Scientific Papers Wissenschaftliche Originalarbeiten*, pp. 216–246, 1985.

[56] R. G. Parr and Y. Weitao, *Density-Functional Theory of Atoms and Molecules*. Oxford University Press, jan 1995. [Online]. Available: https://doi.org/10.1093%2Foso%2F9780195092769.001.0001

[57] R. M. Martin, *Electronic structure: basic theory and practical methods*. Cambridge university press, 2020.

[58] D. S. Sholl and J. A. Steckel, *Density functional theory: a practical introduction*. John Wiley & Sons, 2022.

[59] J. P. Perdew, A. Ruzsinszky, J. Tao, V. N. Staroverov, G. E. Scuseria, and G. I. Csonka, “Prescription for the design and selection of density functional approximations: More constraint satisfaction with fewer fits,” *The Journal of chemical physics*, vol. 123, no. 6, 2005.

[60] C.-K. Skylaris, P. D. Haynes, A. A. Mostofi, and M. C. Payne, “Introducing *ONETEP*: Linear-scaling density functional simulations on parallel computers,” *The Journal of Chemical Physics*, vol. 122, no. 8, feb 2005. [Online]. Available: https://doi.org/10.1063%2F1.1839852

[61] S. Grimme, “Accurate description of van der waals complexes by density functional theory including empirical corrections,” *Journal of Computational Chemistry*, vol. 25, no. 12, pp. 1463–1473, jun 2004. [Online]. Available: https://doi.org/10.1002%2Fjcc.20078

[62] ——, "Semiempirical GGA-type density functional constructed with a long-range dispersion correction," *Journal of Computational Chemistry*, vol. 27, no. 15, pp. 1787–1799, sep 2006. [Online]. Available: https://doi.org/10.1002%2Fjcc.20495

[63] S. Grimme, J. Antony, S. Ehrlich, and H. Krieg, "A consistent and accurate *abinitio* parametrization of density functional dispersion correction (DFT-d) for the 94 elements h-pu," *The Journal of Chemical Physics*, vol. 132, no. 15, apr 2010. [Online]. Available: https://doi.org/10.1063%2F1.3382344

[64] S. Grimme, S. Ehrlich, and L. Goerigk, "Effect of the damping function in dispersion corrected density functional theory," *Journal of Computational Chemistry*, vol. 32, no. 7, pp. 1456–1465, mar 2011. [Online]. Available: https://doi.org/10.1002%2Fjcc.21759

[65] A. D. Becke and E. R. Johnson, "A density-functional model of the dispersion interaction," *The Journal of Chemical Physics*, vol. 123, no. 15, oct 2005. [Online]. Available: https://doi.org/10.1063%2F1.2065267

[67] W. Schottky, "Zur halbleitertheorie der sperrschicht- und spitzengleichrichter," *Zeitschrift for Physik*, vol. 113, no. 5-6, pp. 367–414, may 1939. [Online]. Available: https://doi.org/10.1007%2Fbf01340116

[68] "The theory of crystal rectifiers," *Proceedings of the Royal Society of London. Series A. Mathematical and Physical Sciences*, vol. 171, no. 944, pp. 27–38, may 1939. [Online]. Available: https://doi.org/10.1098%2Frspa.1939.0051

[69] R. T. Tung, "The physics and chemistry of the schottky barrier height," *Applied Physics Reviews*, vol. 1, no. 1, 2014. [Online]. Available: https://doi.org/10.1063/1.4858400

[70] R. Anderson, "Experiments on ge-GaAs heterojunctions," *Solid-State Electronics*, vol. 5, no. 5, pp. 341–351, sep 1962. [Online]. Available: https://doi.org/10.1016%2F0038-1101%2862%2990115-6

[71] R. T. Tung, "Recent advances in schottky barrier concepts," *Materials Science and Engineering: R: Reports*, vol. 35, no. 1-3, pp. 1–138, nov 2001. [Online]. Available: https://doi.org/10.1016%2Fs0927-796x%2801%2900037-7

[72] J. Bardeen, "Surface states and rectification at a metal semi-conductor contact," *Physical Review*, vol. 71, no. 10, pp. 717–727, may 1947. [Online]. Available: https://doi.org/10.1103%2Fphysrev.71.717

[73] L. Li, Y. Yu, G. J. Ye, Q. Ge, X. Ou, H. Wu, D. Feng, X. H. Chen, and Y. Zhang, "Black phosphorus field-effect transistors," *Nature nanotechnology*, vol. 9, no. 5, p. 372, 2014.

[74] S. Das, W. Zhang, M. Demarteau, A. Hoffmann, M. Dubey, and A. Roelofs, "Tunable transport gap in phosphorene," *Nano letters*, vol. 14, no. 10, pp. 5733–5739, 2014.

[75] H. Liu, A. T. Neal, Z. Zhu, Z. Luo, X. Xu, D. Tománek, and P. D. Ye, "Phosphorene: an unexplored 2d semiconductor with a high hole mobility," *ACS nano*, vol. 8, no. 4, pp. 4033–4041, 2014.

[76] ——, "Phosphorene: an unexplored 2d semiconductor with a high hole mobility," *ACS nano*, vol. 8, no. 4, pp. 4033–4041, 2014.

[77] A. Castellanos-Gomez, L. Vicarelli, E. Prada, J. O. Island, K. Narasimha-Acharya, S. I. Blanter, D. J. Groenendijk, M. Buscema, G. A. Steele, J. Alvarez *et al.*, “Isolation and characterization of few-layer black phosphorus,” *2D Materials*, vol. 1, no. 2, p. 025001, 2014.

[78] S. Das, W. Zhang, M. Demarteau, A. Hoffmann, M. Dubey, and A. Roelofs, “Tunable transport gap in phosphorene,” *Nano letters*, vol. 14, no. 10, pp. 5733–5739, 2014.

[79] J. Qiao, X. Kong, Z.-X. Hu, F. Yang, and W. Ji, “High-mobility transport anisotropy and linear dichroism in few-layer black phosphorus,” *Nature communications*, vol. 5, p. 4475, 2014.

[80] F. Xia, H. Wang, and Y. Jia, “Rediscovering black phosphorus as an anisotropic layered material for optoelectronics and electronics,” *Nature communications*, vol. 5, p. 4458, 2014.

[81] V. Tran, R. Soklaski, Y. Liang, and L. Yang, “Layer-controlled band gap and anisotropic excitons in few-layer black phosphorus,” *Physical Review B*, vol. 89, no. 23, p. 235319, 2014.

[82] J. Qiao, X. Kong, Z.-X. Hu, F. Yang, and W. Ji, “High-mobility transport anisotropy and linear dichroism in few-layer black phosphorus,” *Nature communications*, vol. 5, p. 4475, 2014.

[83] H. Liu, A. T. Neal, Z. Zhu, Z. Luo, X. Xu, D. Tománek, and P. D. Ye, “Phosphorene: an unexplored 2d semiconductor with a high hole mobility,” *ACS nano*, vol. 8, no. 4, pp. 4033–4041, 2014.

[84] K. Gong, L. Zhang, W. Ji, and H. Guo, “Electrical contacts to monolayer black phosphorus: A first-principles investigation,” *Physical Review B*, vol. 90, no. 12, p. 125441, 2014.

[85] G. Kresse and J. Furthmüller, “Efficiency of ab-initio total energy calculations for metals and semiconductors using a plane-wave basis set,” *Computational materials science*, vol. 6, no. 1, pp. 15–50, 1996.

[86] ——, “Efficient iterative schemes for ab initio total-energy calculations using a plane-wave basis set,” *Physical review B*, vol. 54, no. 16, p. 11169, 1996.

[87] J. P. Perdew, K. Burke, and M. Ernzerhof, “Generalized gradient approximation made simple,” *Physical review letters*, vol. 77, no. 18, p. 3865, 1996.

[88] G. Kresse and D. Joubert, “From ultrasoft pseudopotentials to the projector augmented-wave method,” *Physical Review B*, vol. 59, no. 3, p. 1758, 1999.

[89] M. Methfessel and A. Paxton, “High-precision sampling for brillouin-zone integration in metals,” *Physical Review B*, vol. 40, no. 6, p. 3616, 1989.

[90] P. E. Blöchl, O. Jepsen, and O. K. Andersen, “Improved tetrahedron method for brillouin-zone integrations,” *Physical Review B*, vol. 49, no. 23, p. 16223, 1994.

[91] J. Klimeš, D. R. Bowler, and A. Michaelides, “Van der waals density functionals applied to solids,” *Physical Review B*, vol. 83, no. 19, p. 195131, 2011.

[93] S. Das, M. Demarteau, and A. Roelofs, "Ambipolar phosphorene field effect transistor," *ACS nano*, vol. 8, no. 11, pp. 11 730–11 738, 2014.

[94] Y. Du, H. Liu, Y. Deng, and P. D. Ye, "Device perspective for black phosphorus field-effect transistors: contact resistance, ambipolar behavior, and scaling," *ACS nano*, vol. 8, no. 10, pp. 10 035–10 042, 2014.

[95] "Resistivity of the elements," https://periodictable.com/Properties/A/Resistivity.al.log.html, accessed date: 28 January 2020.

[96] Q. H. Wang, K. Kalantar-Zadeh, A. Kis, J. N. Coleman, and M. S. Strano, "Electronics and optoelectronics of two-dimensional transition metal dichalcogenides," *Nature Nanotechnology*, vol. 7, no. 11, pp. 699–712, nov 2012. [Online]. Available: https://doi.org/10.1038%2Fnnano.2012.193

[97] D. J. Late, B. Liu, H. S. S. R. Matte, V. P. Dravid, and C. N. R. Rao, "Hysteresis in single-layer mos_2 field effect transistors," *ACS Nano*, vol. 6, no. 6, pp. 5635–5641, may 2012. [Online]. Available: https://doi.org/10.1021%2Fnn301572c

[98] L. Britnell, R. M. Ribeiro, A. Eckmann, R. Jalil, B. D. Belle, A. Mishchenko, Y.-J. Kim, R. V. Gorbachev, T. Georgiou, S. V. Morozov, A. N. Grigorenko, A. K. Geim, C. Casiraghi, A. H. C. Neto, and K. S. Novoselov, "Strong light-matter interactions in heterostructures of atomically thin films," *Science*, vol. 340, no. 6138, pp. 1311–1314, jun 2013. [Online]. Available: https://doi.org/10.1126%2Fscience.1235547

[99] Z. Yin, H. Li, H. Li, L. Jiang, Y. Shi, Y. Sun, G. Lu, Q. Zhang, X. Chen, and H. Zhang, "Single-layer mos_2 phototransistors," *ACS Nano*, vol. 6, no. 1, pp. 74–80, dec 2011. [Online]. Available: https://doi.org/10.1021%2Fnn2024557

[100] Y.-H. Zhang, Y.-B. Chen, K.-G. Zhou, C.-H. Liu, J. Zeng, H.-L. Zhang, and Y. Peng, "Improving gas sensing properties of graphene by introducing dopants and defects: a first-principles study," *Nanotechnology*, vol. 20, no. 18, p. 185504, apr 2009. [Online]. Available: https://doi.org/10.1088%2F0957-4484%2F20%2F18%2F185504

[101] F. Perrozzi, S. Emamjomeh, V. Paolucci, G. Taglieri, L. Ottaviano, and C. Cantalini, "Thermal stability of WS2 flakes and gas sensing properties of WS2/WO3 composite to h2, NH3 and NO2," *Sensors and Actuators B: Chemical*, vol. 243, pp. 812–822, may 2017. [Online]. Available: https://doi.org/10.1016%2Fj.snb.2016.12.069

[102] V. Agarwal and K. Chatterjee, "Recent advances in the field of transition metal dichalcogenides for biomedical applications," *Nanoscale*, vol. 10, no. 35, pp. 16 365–16 397, 2018. [Online]. Available: https://doi.org/10.1039%2Fc8nr04284e

[103] Y. Zhang, T. R. Nayak, H. Hong, and W. Cai, "Graphene: a versatile nanoplatform for biomedical applications," *Nanoscale*, vol. 4, no. 13, p. 3833, 2012. [Online]. Available: https://doi.org/10.1039%2Fc2nr31040f

[104] X. Chen, Z. Zhu, L. Li, H. Li, X. Chen, and S. Li, "Two-dimensional transition metal dichalcogenides-based electronic devices: Recent progress and future perspectives," *Nanomaterials*, vol. 12, no. 1, p. 146, 2022. [Online]. Available: https://www.mdpi.com/2079-4991/12/1/146

[105] J. Gao, F. Zhang, Y. Liu, Y. Liu, Y. Dai, and J. Wang, "Recent progress in the development of ws_2-based flexible and wearable devices," *Frontiers in Materials*, vol. 8, p. 804836, 2021. [Online]. Available: https://www.frontiersin.org/articles/10.3389/fmats.2021.804836/full

[106] Z. Liu, Y. Liu, H. Liu, Y. Chen, S. Xu, H. Zhang, J. He, Z. Wang, P. Liu, P. Hu, and X. Cao, "Recent progress in two-dimensional ws_2-based photoelectric devices," *Frontiers in Materials*, vol. 8, p. 789846, 2021. [Online]. Available: https://www.frontiersin.org/articles/10.3389/fmats.2021.789846/full

[107] K. K. H. Smithe, D. J. Strickland, C. T. Chen, Y. Gong, X. Zhang, X. Shen, and K. Zhang, "Addressing the contact resistance problem in ws_2 field effect transistors," *ACS Applied Materials and Interfaces*, vol. 12, no. 48, pp. 53 308–53 316, 2020. [Online]. Available: https://pubs.acs.org/doi/10.1021/acsami.0c15366

[108] G.-H. Lee, C.-H. Lee, A. M. van der Zande, W. Chen, Y. Li, M. Han, X. Cui, G. Arefe, C. Nuckolls, T. F. Heinz, J. Guo, J. C. Hone, and P. Kim, "Large-scale integration of two-dimensional materials and their heterostructures by wafer bonding," *Nature*, vol. 574, no. 7779, pp. 347–355, 2019. [Online]. Available: https://www.nature.com/articles/s41586-019-1614-8

[109] A. Allain, J. Kang, and K. Banerjee, "Electrical contacts to two-dimensional semiconductors," *Nature Materials*, vol. 14, no. 12, pp. 1195–1205, 2015. [Online]. Available: https://www.nature.com/articles/nmat4449

[110] W. Choi, J. Lee, R. Ghaffari, S. Hwang, T.-i. Kim, and S. K. Kim, "Reducing contact resistance in graphene devices through contact area patterning," *Nano Letters*, vol. 12, no. 3, pp. 1726–1731, 2012. [Online]. Available: https://pubs.acs.org/doi/10.1021/nl204337k

[111] S. Radhakrishnan, S. Kar, and M. DC, "Strategies to reduce contact resistance in metal–2d semiconductor contacts," *Journal of Electronic Materials*, vol. 49, no. 5, pp. 3055–3073, 2020. [Online]. Available: https://link.springer.com/article/10.1007/s11664-020-07971-2

[112] T. Das, S. Wang, T. Zhang, and W. Wu, "Mitigation of contact resistance at the metal-2d semiconductor interface using graphene as an interlayer," *Scientific Reports*, vol. 6, p. 20663, 2016. [Online]. Available: https://www.nature.com/articles/srep20663

[113] J. Zang, J. Liu, J. Qi, G. Zhang, and C. Wu, "Doping-induced reduction of contact resistance in monolayer ws2 field-effect transistors," *Applied Physics Letters*, vol. 112, no. 5, p. 053103, 2018. [Online]. Available: https://aip.scitation.org/doi/10.1063/1.5007221

[114] S.-Y. Lin, S.-H. Hung, Y.-W. Huang, T.-M. Lu, T.-L. Tsai, T.-M. Chen, P.-T. Liu, C.-H. Chen, and L.-J. Li, "Reduced contact resistance in ws2 field-effect transistors via ion implantation doping," *Applied Physics Letters*, vol. 110, no. 12, p. 123106, 2017. [Online]. Available: https://aip.scitation.org/doi/10.1063/1.4979185

[115] S. Banerjee, J. Luginsland, and P. Zhang, "Interface engineering of electrical contacts," *Physical Review Applied*, vol. 15, no. 6, jun 2021. [Online]. Available: https://doi.org/10.1103%2Fphysrevapplied.15.064048

[116] G. Kwon, Y.-H. Choi, H. Lee, H.-S. Kim, J. Jeong, K. Jeong, M. Baik, H. Kwon, J. Ahn, E. Lee, and M.-H. Cho, "Interaction- and defect-free van der waals contacts between metals and two-dimensional semiconductors," *Nature Electronics*, vol. 5, no. 4, pp. 241–247, apr 2022. [Online]. Available: https://doi.org/10.1038%2Fs41928-022-00746-6

[117] S. Bhattacharjee, K. L. Ganapathi, D. N. Nath, and N. Bhat, "Surface state engineering of metal/MoS_2 contacts using sulfur treatment for reduced contact resistance and variability," *IEEE Transactions on Electron Devices*, vol. 63, no. 6, pp. 2556–2562, jun 2016. [Online]. Available: https://doi.org/10.1109%2Fted.2016.2554149

[118] J. Tang, Z. Wei, Q. Wang, Y. Wang, B. Han, X. Li, B. Huang, M. Liao, J. Liu, N. Li, Y. Zhao, C. Shen, Y. Guo, X. Bai, P. Gao, W. Yang, L. Chen, K. Wu, R. Yang, D. Shi, and G. Zhang, "In situ oxygen doping of monolayer mos_2 for novel electronics," *Small*, vol. 16, no. 42, p. 2004276, sep 2020. [Online]. Available: https://doi.org/10.1002%2Fsmll.202004276

[119] Y.-C. Lin, R. Torsi, D. B. Geohegan, J. A. Robinson, and K. Xiao, "Controllable thin-film approaches for doping and alloying transition metal dichalcogenides monolayers," *Advanced Science*, vol. 8, no. 9, p. 2004249, feb 2021. [Online]. Available: https://doi.org/10.1002%2Fadvs.202004249

[120] K. S. Kim, K. H. Kim, J. E. Kang, J.-H. Lee, Y. J. Ji, and G. Y. Yeom, "Atomic layer engineering of TMDs by modulation of top chalcogen atoms: For electrical contact and chemical doping," *ACS Applied Electronic Materials*, vol. 4, no. 8, pp. 3794–3800, aug 2022. [Online]. Available: https://doi.org/10.1021%2Facsaelm.2c00379

[121] T. Zhang, M. Liu, K. Fujisawa, M. Lucking, K. Beach, F. Zhang, M. Shanmugasundaram, A. Krayev, W. Murray, Y. Lei, Z. Yu, D. Sanchez, Z. Liu, H. Terrones, A. L. Elías, and M. Terrones, "Spatial control of substitutional dopants in hexagonal monolayer ws_2: The effect of edge termination," *Small*, vol. 19, no. 6, p. 2205800, jan 2023. [Online]. Available: https://doi.org/10.1002%2Fsmll.202205800

[122] L. Loh, Z. Zhang, M. Bosman, and G. Eda, "Substitutional doping in 2d transition metal dichalcogenides," *Nano Research*, vol. 14, no. 6, pp. 1668–1681, aug 2020. [Online]. Available: https://doi.org/10.1007%2Fs12274-020-3013-4

[123] Y.-C. Lin, S. Li, H.-P. Komsa, L.-J. Chang, A. V. Krasheninnikov, G. Eda, and K. Suenaga, "Revealing the atomic defects of ws_2 governing its distinct optical emissions," *Advanced Functional Materials*, vol. 28, no. 4, p. 1704210, nov 2017. [Online]. Available: https://doi.org/10.1002%2Fadfm.201704210

[124] K. H. Kim, K. S. Kim, Y. J. Ji, I. Moon, K. Heo, D.-H. Kang, K. N. Kim, W. J. Yoo, J.-H. Park, and G. Y. Yeom, "Effect of large work function modulation of mos_2 by controllable chlorine doping using a remote plasma," *Journal of Materials Chemistry C*, vol. 8, no. 5, pp. 1846–1851, 2020. [Online]. Available: https://doi.org/10.1039%2Fc9tc05548g

[125] H.-P. Komsa, J. Kotakoski, S. Kurasch, O. Lehtinen, U. Kaiser, and A. V. Krasheninnikov, "Two-dimensional transition metal dichalcogenides under electron irradiation: Defect production and doping," *Physical Review Letters*, vol. 109, no. 3, jul 2012. [Online]. Available: https://doi.org/10.1103%2Fphysrevlett.109.035503

[126] C. Kim, I. Moon, D. Lee, M. S. Choi, F. Ahmed, S. Nam, Y. Cho, H.-J. Shin, S. Park, and W. J. Yoo, "Fermi level pinning at electrical metal contacts of monolayer molybdenum dichalcogenides," *ACS Nano*, vol. 11, no. 2, pp. 1588–1596, jan 2017. [Online]. Available: https://doi.org/10.1021%2Facsnano.6b07159

[127] Y. Yue, J. Chen, Y. Zhang, S. Ding, F. Zhao, Y. Wang, D. Zhang, R. Li, H. Dong, W. Hu, Y. Feng, and W. Feng, "Two-dimensional high-quality monolayered triangular WS_2 flakes for field-effect transistors," *ACS Applied Materials & Interfaces*, vol. 10, no. 26, pp. 22 435–22 444, jun 2018. [Online]. Available: https://doi.org/10.1021%2Facsami.8b05885

[128] Y. Liu, P. Stradins, and S.-H. Wei, "Van der waals metal-semiconductor junction: Weak fermi level pinning enables effective tuning of schottky barrier," *Science advances*, vol. 2, no. 4, p. e1600069, 2016. [Online]. Available: https://doi.org/10.1126/sciadv.1600069

[129] R.-S. Chen, G. Ding, Y. Zhou, and S.-T. Han, "Fermi-level depinning of 2d transition metal dichalcogenide transistors," *Journal of Materials Chemistry C*, vol. 9, no. 35, pp. 11 407–11 427, 2021. [Online]. Available: https://doi.org/10.1039%2Fd1tc01463c

[130] P.-C. Shen, C. Su, Y. Lin, A.-S. Chou, C.-C. Cheng, J.-H. Park, M.-H. Chiu, A.-Y. Lu, H.-L. Tang, M. M. Tavakoli, G. Pitner, X. Ji, Z. Cai, N. Mao, J. Wang, V. Tung, J. Li, J. Bokor, A. Zettl, C.-I. Wu, T. Palacios, L.-J. Li, and J. Kong, "Ultralow contact resistance between semimetal and monolayer semiconductors," *Nature*, vol. 593, no. 7858, pp. 211–217, may 2021. [Online]. Available: https://doi.org/10.1038%2Fs41586-021-03472-9

[131] C. Gong, L. Colombo, R. M. Wallace, and K. Cho, "The unusual mechanism of partial fermi level pinning at metal mos_2 interfaces," *Nano Letters*, vol. 14, no. 4, pp. 1714–1720, mar 2014. [Online]. Available: https://doi.org/10.1021%2Fnl403465v

[132] H. J. Kulik, "Perspective: Treating electron over-delocalization with the dft + u method," *The Journal of Chemical Physics*, vol. 142, no. 24, jun 2015. [Online]. Available: https://doi.org/10.1063%2F1.4922693

[133] V. I. Anisimov, F. Aryasetiawan, and A. Lichtenstein, "First-principles calculations of the electronic structure and spectra of strongly correlated systems: the lda+ u method," *Journal of Physics: Condensed Matter*, vol. 9, no. 4, p. 767, 1997. [Online]. Available: https://doi.org/10.1088/0953-8984/9/4/002

Biography

Name	Mr. Abdul Ghaffar
Date of Birth	12 July 1996
Educational Attainment	MSc in Physics Indian Institute of Technology Gandhinagar, Gujarat, India, 2019 BSc (Hons) in Physics: Aligarh Muslim University Aligarh, India, 2017
Scholarship	2021-2024: Monbukagakusho (MEXT) Scholarship
Work Experiences	2019-2021: Research Assistant Indidian Institute of Technology Gandhinagar, India

Publications

[1] A. Ghaffar, Mohit D. Ganeriwala, K. Hongo, R. Maezono, and Nihar R. Mohapatra "Insights into the Mechanical and Electrical Properties of a Metal-Phosphorene Interface: An Ab Initio Study with a Wide Range of Metals" *ACS Omega*, 6, 7795-7803, 2021

[2] A. Ghaffar, P. Song, K. Hongo, R. Maezono, "High- superconductivity of clathrate Y_3EuH_{24}" *arXiv preprint*, arXiv:2205.05906, 2022

[3] A. Ghaffar, Nihar R. Mohapatra, R. Maezono, K. Hongo "Substitutional Doping Strategies for Fermi Level Depinning and Enhanced Interface Quality in WS2-Metal Contacts" *ACS Applied Electronic Materials*, *Manuscript under review*, 2024

[4] K. Saritas, A. Ghaffar, J. Krogel, T. Ichibha, K. Hongo, R. Maezono, F. Reboredo "Enhancing $MnBi_2Te_4$ stability by doping", *The Journal of Physical Chemistry C*, *Submitted for review*, 2024

[5] P. Song, A. Durajski, Z. Hou, A. Ghaffar, R. Dahule, R. Szczesniak, K. Hongo, R. Maezono "(La, Th)H_{10}: Potential High-T_c (242 K) Superconductors Stablized Thermodynamically below 200 GPa", *The Journal of Physical Chemistry C*, 2024